

10. SITE 956¹

Shipboard Scientific Party²

HOLE 956A

Date occupied: 14 September 1994
Date departed: 15 September 1994
Time on hole: 1 days, 9 hr, 40 min
Position: 27°36.905'N, 16°9.797'W
Bottom felt (drill-pipe measurement from rig floor, m): 3453.4
Distance between rig floor and sea level (m): 11.50
Water depth (drill-pipe measurement from sea level, m): 3441.9
Total depth (from rig floor, m): 3615.00
Penetration (m): 161.60
Number of cores (including cores having no recovery): 18
Total length of cored section (m): 161.60
Total core recovered (m): 160.48
Core recovery (%): 99.3
Oldest sediment cored:
Depth (mbsf): 161.60
Nature: lapillistone
Earliest age: early Pliocene

HOLE 956B

Date occupied: 15 September 1994
Date departed: 22 September 1994
Time on hole: 5 days, 4 hr, 7 min
Position: 27°36.895'N, 16°9.797'E
Bottom felt (drill-pipe measurement from rig floor, m): 3453.4
Distance between rig floor and sea level (m): 11.50
Water depth (drill-pipe measurement from sea level, m): 3441.9
Total depth (from rig floor, m): 4156.90
Penetration (m): 703.50
Number of cores (including cores having no recovery): 57
Total length of cored section (m): 546.40
Total core recovered (m): 297.40
Core recovery (%): 54.4
Oldest sediment cored:
Depth (mbsf): 703.50
Nature: hyaloclastite lapillistone
Earliest age: middle Miocene

Principal results: Site 956, the second of two sites drilled in the southern volcanic apron of Gran Canaria, is located in the southern Canary Channel and has received sediments from three sources apart from background sedimentation: African continental margin, Gran Canaria, and Tenerife.

The major volcanic events to be studied comprise (1) large explosive eruptions that resulted in widespread ash flows and ash falls during Mogan and Fataga volcanism, (2) the basaltic shield phase, and (3) Pleistocene tephra layers from Tenerife. The influx of volcanoclastics in the upper part of the sediment column (younger than ~10 Ma) was expected to be small, because post-Miocene volcanic activity is absent in the south of the island. Larger thicknesses of volcanoclastic sediments from Tenerife were expected, however, because of the greater proximity to this island and presumed paleowind directions comparable to the present.

The sedimentary succession drilled at Site 956 is 704 m thick and consists dominantly of fine-grained hemipelagic sediments with interbeds in the uppermost and lower part, of coarse-grained volcanoclastic and, in the middle part, of siliciclastic material. Ages range from Holocene to middle Miocene. The supply of volcanoclastic material by sediment gravity flows and fallout from both Gran Canaria and Tenerife has played a fundamental role in determining the lithostratigraphy of Site 956. The sedimentary succession has therefore been subdivided into five lithostratigraphic units based chiefly on the abundance and composition of volcanoclastic deposits that correspond broadly in time and composition to the Miocene magmatic phases of Gran Canaria and Pleistocene volcanism on Tenerife.

Unit I (0–158 mbsf): consists mostly of nannofossil mixed sediment with foraminifers with thick interbedded coarse debris flows, typically rich in pumice, which were most likely derived from Tenerife. Their initiation may be related to sea level changes caused by Pleistocene glacial–interglacial cycles. Tephra fall layers of similar age and mineralogy have also been found at all other sites and at Site 397, southeast of the island of Gran Canaria. Slump deposits are common in this unit.

Unit II (158–195 mbsf): has very poor recovery but the angular clasts are identical petrographically to Miocene shield basalts and to trachyphonolitic ignimbrites from Gran Canaria. Much of the unit may represent slump debris from the collapsed flank of southwestern Gran Canaria.

Unit III (195–370 mbsf): 175 m thick; early Pliocene to late Miocene in age. It consists dominantly of nannofossil mixed sediment and clayey nannofossil ooze. The unit is distinguished from Unit II by the lack of coarse-grained material, with only minor interbeds of quartzose and calcareous sand deposits. Slumping is pervasive.

Unit IV (370–564 mbsf): The lower part of the sequence (Subunits IVa and IVb) has numerous interbedded volcanoclastic deposits that can be correlated with Miocene Fataga and Mogan group volcanism on Gran Canaria. Core descriptions and logging data indicate that tuff layers begin to appear in Core 157-956B-23R where the upper boundary of the Fataga-equivalent sediments (Subunit IVa) was placed. Zeolitized and fresh vitric tuffs are common in Subunit IVa (Fataga), while more abundant fresh glass occurs in Subunit IVb (Mogan); similar relationships were found at Sites 953 and 955. The compositionally distinct ignimbrite P1 (14 Ma), previously recognized at 845 mbsf at Site 953, ~170 km northeast of Site 956, and at 560 mbsf at Site 955, occurs at 564 mbsf at Site 956. Some of the vitric material in this unit was re-worked and deposited by turbidity currents, whereas at least some may have been associated with the entrance of pyroclastic flows into the sea, with subsequent transformation to water-rich sediment gravity flows. In general, the flux of coarse volcanoclastic material during this time was high, reflecting the voluminous nature of the mid-Miocene Mogan activity.

¹ Schmincke, H.-U., Weaver, P.P.E., Firth, J.V., et al., 1995. *Proc. ODP, Init. Repts.*, 157: College Station, TX (Ocean Drilling Program).

² Shipboard Scientific Party is given in the list preceding the Table of Contents.

Unit V (564–704 mbsf): 140 m thick; middle Miocene in age. It consists of moderately sorted and graded massive basaltic breccia and hyaloclastite tuff units interpreted as debris flow deposits. The breccias contain abundant subrounded to rounded clasts of nonvesicular basalt and red oxidized scoriaceous fragments indicating derivation from subaerial volcanism. Smaller amounts of altered vesicular hyaloclastite grains also occur, suggesting that hydroclastic eruptions were taking place at this time. The products of both submarine and subaerial volcanism were mixed prior to deposition. Minor hemipelagic interbeds and mixed volcanoclastic and siliciclastic sediments occur in the upper part of the unit. A foraminifer sand rich in amphibole, zircon, and sphene, which also shows up well in the natural gamma log, represents an unusual lithology and appears to be derived from metamorphic or plutonic basement. Minor quartz occurs at 600 mbsf and a huge debris flow at least 85 m thick comprises the basal part of the hole.

Sediment accumulation rates are difficult to calculate for Site 956, except for the upper 50 m of the sequence, because the upper 370 m, within Units I, II, and III (see "Lithostratigraphy" section, this chapter), contain abundant chaotically disturbed sediments. Discrepancies exist between the microfossil ages and paleomagnetic ages in the lower part of the hole that should be clarified by shore-based single crystal dating. Very high accumulation rates must be assumed for the deposits of Unit V (564–704 mbsf) on biostratigraphic grounds and because most of this sequence is made up of only 3 debris flows.

A complete suite of three logging strings were successfully run in Hole 956B. The quad combination and geochemical tools and the FMS recorded data from the base of hole (650 mbsf) to the end of pipe (300 mbsf). The quality of the recorded logs is excellent, enabling detailed characterization of the sequence of pelagic, turbidite, and volcanoclastic material. The changes from shallow submarine through emergent basaltic to subaerial shield and subsequent ash flow eruptions are especially well reflected in the logs. The components of potassium, uranium, and thorium derived from the total natural gamma-ray log are particularly diagnostic. The transition from the shield to the volcanoclastic sediments correlative to the Mogan Formation is characterized by sharp increases in density, sonic velocity, and resistivity as well as an abrupt increase in potassium, thorium, and uranium. Similarly, the abrupt decrease of potassium, uranium, and thorium, and, to a lesser degree, resistivity, reflects the pronounced decrease in supply of volcanoclastics in the volcanic hiatus above. Even the geochemically similar Mogan and Fataga formations can be distinguished from each other by the patterns of the natural gamma-ray log.

There is generally good agreement between the stratigraphic and lithologic interpretations of the cores and the depositional architecture as derived from the seismic profile. Three major sequences can be discerned in the seismic profile, an upper one comprising seismic Units A, B, and C, a middle one consisting of only one subunit, Unit D, and a lower sequence comprising seismic Units E and F. The upper sequence is slightly thinning basinward. The sequence corresponds to the Pliocene–Pleistocene deposits in lithostratigraphic Units I and II. The middle sequence is characterized by basinward thickening and lateral change in seismic facies. The sequence corresponds approximately to the late Miocene deposits of lithostratigraphic Units III and IVa. The lower sequence, which thins basinward, corresponds to the early-middle Miocene deposits of lithologic Units IVb and V. The transition from seismic Unit E to F seems to correspond to the base of the Mogan Formation on the island.

Four ADARA temperature measurements taken between 44.1 and 101.1 mbsf gave a geothermal gradient of 33.51°C/km. Thermal conductivity downhole had an average value of approximately 1.11 W/(m·K), resulting in a heat flow value of 37.20 mW/m². These values are high for a continental margin setting and most likely reflect the Canary Island hot spot.

Summary: The basaltic shield stage of Gran Canaria was penetrated for 140 m and found to consist of three debris flows, which do not represent the true submarine stage below the volatile fragmentation depth but must have formed while the island was already emerged. Seismic data acquired dur-

ing the approach to the site imply that volcanoclastic sediments related to the shield stage extend to much greater depth.

A very thick sequence of vitric tuffs are interpreted to reflect both primary and reworked ash flow eruptions during both the Mogan and Fataga formations. The compositionally distinct ignimbrite P1 (14.1 Ma) was recognized at the base of the vitric tuff-rich lower part of the hole, as at Sites 953 and 955. Significant volcanoclastic material supplied to the site from other islands appears to be restricted to Pleistocene turbidite, grain flow, and fallout tephra layers presumably from Tenerife. Much will be learned about composition, repose periods, and magnitude of explosive volcanism of Pico de Teide by shore-based study of the Pleistocene tephra layers.

The sedimentary succession recovered at Site 956 bears many similarities to that of Site 953. In contrast to Site 953, however, Site 956 in the southern basin also received siliciclastic material and clay from the African continental margin, as also reflected in the generally lower CaCO₃ concentrations of the sediment. The greater abundance of slumps in the upper ~380 m of Site 956 may reflect wholesale sediment packet sliding but to a much lesser degree than at Site 955.

BACKGROUND AND OBJECTIVES

Background

Site 956, the last of four VICAP sites, was drilled into the southwestern peripheral volcanic apron of Gran Canaria. The site is located in the southern Canary Channel, 45 km southwest of the coast of Gran Canaria, 57 km southeast of southern Tenerife, and ~200 km west of the African continental margin. Unlike the two northern sites, this location is not shielded from sediment influx from the African continental margin. The site is separated from Site 954 in the northern basin by the ridge (maximum water depth of 2200 m) between Tenerife and Gran Canaria. The drill site is in a fairly flat area close to the morphological flank of Gran Canaria at a water depth of ~3440 m. Site 956 is the second of two sites drilled in the southern volcanic apron of Gran Canaria.

Objectives

The objectives of drilling Sites 955 and 956 are similar; Site 956 represents the westernmost of the south Canary Channel facies of the volcanoclastic apron. The sediments south of Gran Canaria are expected to differ significantly from those in the north on account of the absence of post-Miocene volcanic activity in the south and are expected to represent chiefly the basaltic shield (subaerial history ~14.5–15.5 Ma) and overlying rhyolitic (14–13.4 Ma) and trachyphonolitic (13.4–9.5 Ma) pyroclastic formations.

Age, Composition, and Volcanic Evolution of the Shield Phase of Gran Canaria

One objective at this site is to document the shield stage of Gran Canaria. No major influences of the shield stages of the eastern islands are expected at this location. Clarification of the ages of the shield phases is crucial for understanding the early magmatic and temporal evolution of Gran Canaria and correlation of the datums to those obtained at the other three sites.

What is the response of the lithosphere to loading and heating during magmatic activity as reflected in the attitude of the lowermost volcanic deposits? Can a true submarine phase (i.e., eruption below the volatile fragmentation depth) be distinguished from the emerging phase of a shield volcano? Can slump events, believed to be associated with the origin of the large subaerial and submarine scars in southwest Gran Canaria, one of which formed during the close but

prior to the end of basaltic shield volcanism on Gran Canaria, be detected in the sedimentary record?

Rhyolitic Ash Flows

A second major objective is to document rhyolitic ash flows (~15 cooling units of the Mogan group) erupted on Gran Canaria between 14 and 13.4 Ma. Even though Site 956 is 45 km from the present coast of Gran Canaria, we hope to find the distal submarine continuation of many of these ash flows and some associated ash-fall tephra layers. Questions to be addressed include the following: Are the marine ash layers the direct result of explosive eruptions on land? How does the physical nature of high temperature ignimbrites change when they enter the sea? How can ash layers resulting from erosion be distinguished texturally and structurally from those recording explosive volcanic eruptions?

Explosive Trachyphonolitic Volcanism of the Fataga Group

The rocks of the Fataga Group represent an exceptionally long (4 Ma) record of highly evolved explosive volcanism. Many ash layers are expected in the time interval between ~13.4 and 9.5 Ma. The reconstruction of the fallout fans should help to constrain the paleowind pattern during the middle Miocene. A major influx of Fataga erosional debris correlatable with the widespread Miocene gravel fans in southern Gran Canaria could be reflected in the clastic sediments at this site. We also hope to correlate major land and submarine events with distinct seismic reflectors.

Tenerife Explosive Volcanism

Because of the close proximity of Site 956 to Tenerife, many ash and pumice layers related to evolution of the caldera rocks and Pico de Teide Volcano (2–0.13 Ma) are expected. Our objective is to reconstruct the temporal and compositional evolution of this large evolved volcano by analyzing the glass and mineral phases. So far four phases in the activity of the evolved edifice have been recognized. It will be interesting to see how many of these distinct phases, and additional ones, can be recognized in fallout tephra layers. This analysis will help to better define the length of eruptive and repose periods of this active volcano and estimate the magnitude of its explosive eruptions. The reconstruction of the fallout fans should help to constrain the paleowind pattern during the Quaternary.

UNDERWAY GEOPHYSICS

On our approach to Site 956 a ~18-km-long reflection seismic profile was acquired starting at 27°39.3'N, 16°05.6'W and ending at 27°34.0'N, 16°15'W. An 80 in.³ water gun was used as a seismic source and the signals were recorded on a single channel streamer and displayed on line-scan recorders for immediate inspection. The shot interval was 8 s corresponding to an average shot distance of 22 m. Data was stored digitally on 8 mm tape and subsequently processed shipboard with SIOSEIS software. The processing sequence was as follows: finite difference migration, bandpass filter (40–150 Hz), automatic gain control (200 ms window), trace mix (weights 1 2 1), display. The processed profile is shown in Figure 1 and the interpretative line drawing in Figure 2. The profile intersects the pre-site-survey Profile P105 SP 3900 at SP 358 and Profile P106 SP 100 at SP 625, as indicated in Figure 1. The reason for supplementing the existing profiles was mainly to secure additional insight in the three dimensional aspects of the sequence to be drilled. No complications were observed and the following description refers to the new seismic profile (unless otherwise specified).

The seismic profile has a penetration of ~1 s below the seafloor. The acoustic basement appears as an approximately horizontal reflector at 5.2–5.3 s. The seafloor reflector is plane with a subtle southwestward dip from 4.5 to 4.55 s in the southwestern half of the profile. In the northeastern part of the profile the seafloor starts to rise toward Gran Canaria with an initial slope dipping ~3° westward. Site 956 is located at the foot of this slope. The average slope northeast of Site 956 is ~2°. The seafloor here is undulating, and a local mound ~75 m high and ~1 km wide is located near the end of the profile. When compared with the seafloor topography seen on the crossing profiles, the seafloor features appear to have an approximately north-south trend parallel to the local seafloor contours.

The sequence between the seafloor and the acoustic basement is divided into seismic Units A, B, C, D, E, and F, based on characteristics of internal reflectors and their relationship to bounding reflectors.

The base of the shallowest unit (A) is defined by a reflector that is approximately concordant with the seafloor. The basal reflector is coherent and has a high amplitude in the flat basinward part of the profile. On the slope the basal reflector has varying amplitude and continuity. Unit A forms a drape sheet with a nearly constant thickness of 25 ms.

The base of Unit B is defined by a reflector onto which internal reflectors onlap and downlap. The base is very well defined by a nearly horizontal, continuous, high-amplitude reflector in the southwestern part of the profile. In the northwestern end of the profile, where the reflector rises toward the island, the amplitude and the continuity is so strongly reduced that identification is difficult. Unit B is characterized by substantial variation vertically as well as laterally. Four subunits, B1, B2, B3, and B4, can be discerned.

Subunit B1 is restricted to the slope where it appears as a series of mounds with decreasing height downslope. The largest of the mounds rest on an interval that contains a series of parallel, high-amplitude reflectors. These reflectors define Subunit B2 on the slope. In a downslope direction the parallel reflectors in Subunit B2 continue, with a short interruption in an interval with strongly reduced amplitudes, until they are truncated by Unit A at the slope adjacent to Site 956. The Subunit B2 reaches its maximum thickness of 100 ms close to the northeast of Site 956. At Site 956 the thickness of Subunit B2 is reduced to 25 ms and it is transparent. Subunit B2 continues in a basinward direction as a transparent sheet with constant thickness. A basinward thickening to ~75 ms and a regain of the amplitudes commences ~4 km from Site 956. The thickness of Subunit B3 varies between 30 and 75 ms. The subunit thins out in a basinward direction. Internal high-amplitude, subparallel, wavy reflectors prevail in the most basinward parts. These reflectors appear to downlap onto the basal reflector. The subunit is transparent at Site 956 and upslope. In the most elevated part, thickness appears to increase and internal reflectors indicate the presence of mounded features. Subunit B4 is only found outside the slope. The extent of the subunit coincides with the extent of the high-amplitude part of the basal reflector for Unit B. Subunit B4 is nearly transparent, but distinct low-amplitude reflectors show low-angle truncations/toplaps at the surface of the subunit and onlaps and downlaps at the base. The thickness of Subunit B4 reaches a maximum of ~75 ms basinward of Site 956. The total thickness of Unit B at Site 956 is 150 ms.

Unit C is bounded by almost horizontal, continuous, high-amplitude reflectors except in the northeastern most part of the profile where amplitude and continuity is low and where the reflectors have a basinward slope of ~2°. Amplitude and continuity of internal reflectors follow the external reflectors. Outside the slope internal reflectors indicate a series of aggrading sheets, each typically 10–25 ms thick.

Unit D is wedge-shaped with thicknesses increasing from 150 ms at the slope to 350 ms in the basinward end of the profile. The base of the unit is defined by a basinward sloping surface onto which the

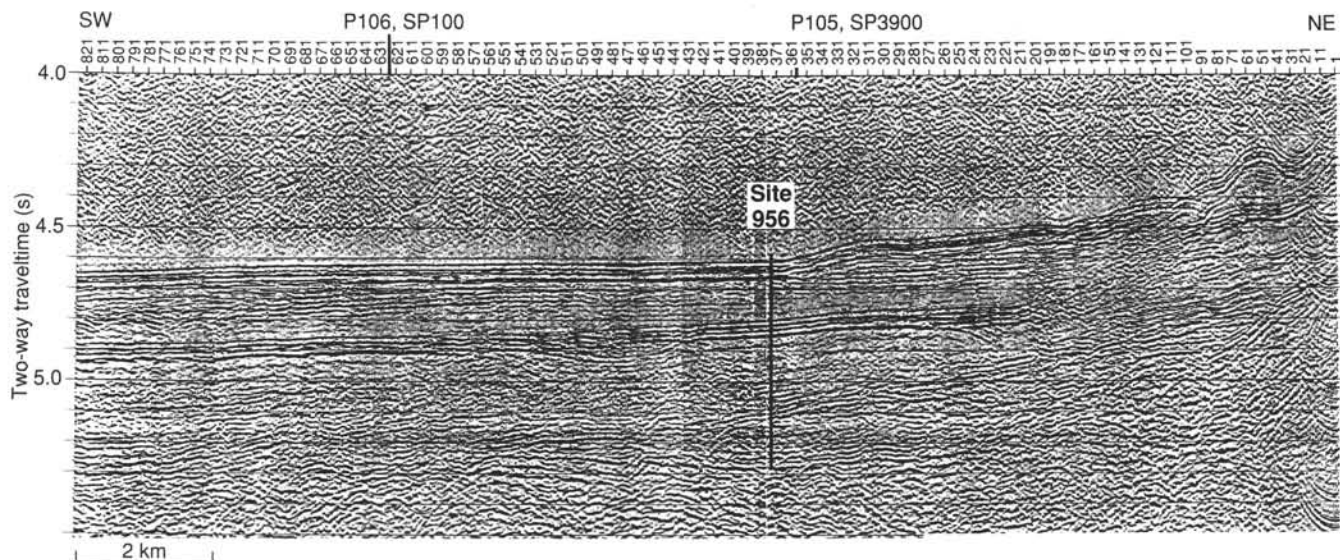


Figure 1. Processed seismic profile acquired during approach to Site 956. Estimated depth (mbsf) to unit-boundaries are given at Site 956.

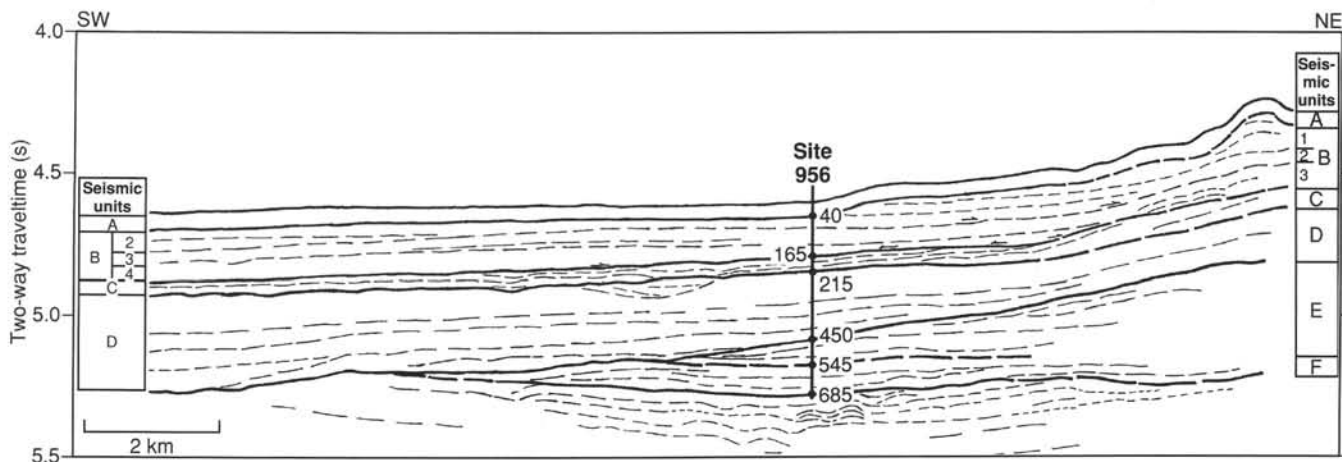


Figure 2. Seismic-stratigraphic interpretation of the seismic profile at Site 956.

internal reflectors in the lower part of the unit onlap or downlap. The internal reflectors in the lower part of the unit have relatively high amplitudes, but the continuity is generally low. This lower part of the unit pinches out as it onlaps the sloping base of the unit. The upper 100 ms of the unit is characterized by low-amplitude reflectors with long periods and low continuity outside the slope. On the slope the reflector pattern changes to short period reflectors with relatively high continuity. The upper part of the unit maintains its thickness or even increases in thickness on the slope. Internal reflectors are generally concordant with the top of the unit. The only exception is a cut-and-fill-like feature located in the upper part of the unit ~2 km basinward of Site 956.

Units E and F together form a wedge-shaped complex that pinches out in a basinward direction. The total thickness amounts to 400 ms in the northern side of the profile, where only the top of Unit E and base of Unit F can be identified. The boundary between Units E and F is defined in the basinward end of the wedge, as the reflector onto which the toe of Unit E downlaps. Internal reflectors in Unit F tend to converge in a basinward direction.

Except for the pinch-out zone the thickness of Unit F is almost constant at ~100 ms. Internal reflectors downlap onto the basal reflector. This reflector, and its correlative reflector at the base of Unit D outside the pinch-out zone, is defined as the acoustic basement. As indicated in Figure 2 a few weak traces of subparallel or wavy reflectors appear below the acoustic basement reflector. These reflectors seem to indicate a wide sag with the deepest point close to Site 956.

At Site 956 a high quality sonic log was obtained in the interval 304–680 mbsf. Together with velocity data from the MST a complete velocity function from seafloor to 680 mbsf was calculated (Fig. 3).

The depths of the seismic units at Site 956 was calculated as follows:

- Unit A: 0–40 mbsf
- Unit B: 40–165 mbsf
- Unit C: 165–215 mbsf
- Unit D: 215–450 mbsf
- Unit E: 450–545 mbsf
- Unit F: 545–685 mbsf

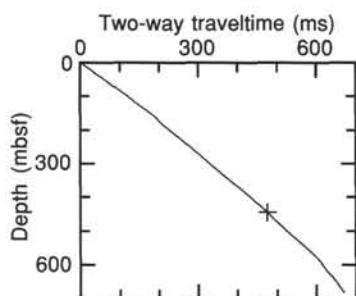


Figure 3. Relationship derived from sonic log and MST-data between depth and two-way traveltime, measured from the seafloor reflector.

OPERATIONS

Site 955 to Site 956 (VICAP-7) Transit

The vessel sailed the 49 nmi to the survey area at an average speed of 10.4 kt. After a 3 hr seismic survey, the vessel returned to the site coordinates. The hydrophones and thrusters were extended as the *JOIDES Resolution* was offset to the GPS coordinates of the site. At 1331, local time, 14 September, a beacon was dropped on location. A back-up beacon was dropped at 1401 when the initial beacon's anchor line parted. The first beacon was retrieved.

Hole 956A

An APC/XCB BHA was made up and Core 157-956A-1H established the mud line depth at 3441.9 mbsf. Hole 956A was APC/XCB cored to XCB refusal at 161.6 mbsf (Table 1). The APC cored 158.1 m (17 cores) and recovered 158.7 m (100.4% recovery). Cores were oriented starting with Core 157-956A-3H. Heat flow measurements were conducted while Cores 157-956A-5H, 157-956A-8H, and 157-956A-11H were obtained. XCB coring was initiated at 158.1 mbsf when the formation prevented even a partial stroke of the APC after Core 157-956A-17H. The XCB core barrel was pulled after penetrating 3.5 m in 20 min. The hard clay and lapillistone recovered in the single XCB core combined with the slow rate of advance indicated that the RCB should be used to obtain the deeper objectives of the site. The total recovery of the hole was 99.3%. There was a trace of methane (2–3 ppm) in the cores.

Hole 956B

At 1600, 15 September, the bit was pulled out of the hole to change to the RCB system. The vessel was offset 20 m south, and an RCB BHA was made up. Hole 956B was spudded at 0705, 16 September. After washing down to 157.1 mbsf, the wash barrel was retrieved and a new barrel dropped. RCB coring advanced relatively quickly from 157.1 to 590.0 mbsf (Cores 157-956B-1R through 157-956B-45R with 54.6% recovery). During this interval, the deplugger had to be dropped after Cores 157-956B-8R and 157-956B-9R were retrieved with zero recovery. Preventive mud flushes of 25 bbl of sepiolite were circulated at 512 and 552 mbsf.

After cutting Core 157-956B-45R, the hole began packing off with a loss of circulation and rotation caused by the stalling of the top drive. After the driller bled off the pressure and backed off on the torque on the drill string with the top drive, rotation and circulation were immediately regained. The hole was swept with 50 bbl sepiolite flush and the core barrel containing 157-956B-45R was retrieved.

To ensure a viable hole for the deeper objective of the site, a wiper trip was initiated. Maximum overpull coming out of the hole was at 221 mbsf (20,000 lb.). The drill string was run in to 313 mbsf where a hard bridge was tagged. The hole was washed and reamed from 302 to 395 mbsf. The drill string was washed down from 395 to 571 mbsf

and tagged 19 m of soft fill. The hole was washed and reamed from 571 to 590 mbsf and then swept with a 30 bbl treatment of sepiolite. After the wash barrel was retrieved, RCB coring resumed at 1600, 19 September.

RCB coring continued until shortly after midnight on 20 September when the depth objective of 703.5 mbsf was reached. 20 bbl sepiolite flushes were pumped after every core, starting with Core 157-956B-48R. Total recovery for the hole was 54.4% of the cored interval (546.4 m). The gas detected during this hole ranged from 2 to 4 ppm methane.

At 0030, 21 September, the hole was prepared for logging. A wiper trip was begun, and a hard bridge was contacted at 597 mbsf. The hole was washed and reamed from 577 to 704 mbsf (TD), and flushed with 50 bbl of sepiolite. The bit was released at 703 mbsf. The hole was displaced with an 8.8 ppg concentration of sepiolite mud, and the drill pipe was pulled out to the logging depth of 300 mbsf.

Three tool strings, the quad combination, geochemical, and FMS, were successfully logged from the base of the hole to the end of pipe (300 mbsf).

The logging string and the pipe was pulled, and the deck was secured by 0000, September 22. The ship was underway to Las Palmas by 2130, September 23. The pilot met the ship at approximately 0600, September 23, and the ship was at dock by ~0800, September 23, ending Leg 157.

LITHOSTRATIGRAPHY

The sedimentary succession recovered at Site 956 is 704 m thick and consists of abundant hemipelagic material (clayey nannofossil mixed sediment and clayey nannofossil mixed sediment with foraminifers), major volcanoclastic sediments, and minor turbidite interbeds of siliciclastic and bioclastic sands and silts (Fig. 4). The sequence ranges in age from Pleistocene to middle Miocene. The sedimentary succession has been divided into five lithostratigraphic units based on the abundance and lithology of sand interbeds (Fig. 5) and abundance of slumped intervals.

Calcium carbonate content in the hemipelagic sediments from 0 to 350 mbsf does not significantly change and ranges between 40 and 75 wt% (Fig. 6). Below 300 mbsf calcium carbonate contents sharply decrease, ranging between 30 and 40 wt% from 340 to 350 mbsf (Fig. 6). The calcium carbonate content of turbidite muds and sands is lower (25%–45%) than hemipelagic sediment from 0 to 300 mbsf. It ranges more widely (20% to 50 wt%), below 300 mbsf. These trends resemble those at Site 956 but the decrease in carbonate occurs 30 m shallower at Site 955 (270 mbsf) than at Site 956 (300 mbsf).

Unit I

Interval: Sections 157-956A-1H-1 to 157-956A-17H-CC
Depth: 0–158 mbsf
Age: Pleistocene to late Pliocene

Unit I is 158 m thick and the dominant lithologies are clayey nannofossil mixed sediment with foraminifers and clayey nannofossil mixed sediment. The unit is characterized by slump and soft sediment deformation throughout. It is subdivided into three subunits based on differences in the minor sand lithologies and occurrence of specific volcanic components.

Subunit Ia

Interval: Sections 157-956A-1H-1 to 157-956A-5H-3
Depth: 0–37.5 mbsf
Age: Pleistocene

Subunit Ia is 37.5 m thick. This subunit consists mostly of greenish-gray, medium to thick bedded, clayey nannofossil mixed sedi-

Table 1. Coring summary, Holes 956A and 956B.

Core	Date (September 1994)	Time (UTC)	Sub-bottom (m)		Cored (m)	Recovered (m)	Recovery (%)	Section	Length (m)	Depth (mbsf)		Samples	
			Top	Bottom						Top	Bottom		
157-956A- 1H	14	2105	0.0	6.1	6.1	6.14	100.0	1	1.50	0.00	1.50	IW 145-150 HS 0-5/voids closed on catwalk	
								2	0.89	1.50	2.39		
								3	0.92	2.39	3.31		Voids closed on catwalk
								4	1.50	3.31	4.81		
								5	1.13	4.81	5.94		
								CC	0.20	5.94	6.14		
2H	14	2210	6.1	15.6	9.5	8.82	92.8	1	1.50	6.10	7.60	IW 145-150 HS 0-5	
								2	1.50	7.60	9.10		
								3	1.50	9.10	10.60		
								4	1.50	10.60	12.10		
								5	1.50	12.10	13.60		
								6	0.99	13.60	14.59		
3H	14	2315	15.6	25.1	9.5	10.00	105.2	CC	0.33	14.59	14.92	IW 145-150 HS 0-5	
								1	1.50	15.60	17.10		
								2	1.50	17.10	18.60		
								3	1.50	18.60	20.10		
								4	1.50	20.10	21.60		
								5	1.50	21.60	23.10		
4H	15	0015	25.1	34.6	9.5	9.82	103.0	6	1.50	23.10	24.60	IW 145-150 HS 0-5	
								7	0.80	24.60	25.40		
								CC	0.20	25.40	25.60		
								1	1.50	25.10	26.60		
								2	1.50	26.60	28.10		
								3	1.50	28.10	29.60		
5H	15	0130	34.6	44.1	9.5	10.06	105.9	4	1.50	29.60	31.10	IW 140-150 HS 0-5	
								5	1.50	31.10	32.60		
								6	1.50	32.60	34.10		
								7	0.52	34.10	34.62		
								CC	0.30	34.62	34.92		
								1	1.50	34.60	36.10		
6H	15	0220	44.1	53.6	9.5	6.57	69.1	2	1.50	36.10	37.60	IW 140-150 HS 0-5	
								3	1.50	37.60	39.10		
								4	1.50	39.10	40.60		
								5	1.50	40.60	42.10		
								6	1.50	42.10	43.60		
								7	0.65	43.60	44.25		
7H	15	0320	53.6	63.1	9.5	9.78	103.0	CC	0.41	44.25	44.66	IW 140-150	
								1	1.50	44.10	45.60		
								2	1.50	45.60	47.10		
								3	1.50	47.10	48.60		
								4	1.50	48.60	50.10		
								5	0.33	50.10	50.43		
8H	15	0435	63.1	72.6	9.5	9.52	100.0	CC	0.24	50.43	50.67	IW 140-150 HS 0-5	
								1	1.50	53.60	55.10		
								2	1.50	55.10	56.60		
								3	1.50	56.60	58.10		
								4	1.50	58.10	59.60		
								5	1.50	59.60	61.10		
9H	15	0535	72.6	82.1	9.5	9.92	104.0	6	1.50	61.10	62.60	IW 140-150 HS 0-5	
								7	0.56	62.60	63.16		
								CC	0.22	63.16	63.38		
								1	1.50	63.10	64.60		
								2	1.50	64.60	66.10		
								3	1.50	66.10	67.60		
10H	15	0625	82.1	91.6	9.5	9.30	97.9	4	1.50	67.60	69.10	IW 140-150 HS 0-5	
								5	1.50	69.10	70.60		
								6	1.50	70.60	72.10		
								CC	0.52	72.10	72.62		
								1	1.50	72.60	74.10		
								2	1.50	74.10	75.60		
11H	15	0735	91.6	101.1	9.5	9.96	105.0	3	1.50	75.60	77.10	IW 140-150 HS 0-5	
								4	1.50	77.10	78.60		
								5	1.50	78.60	80.10		
								6	1.50	80.10	81.60		
								7	0.55	81.60	82.15		
								CC	0.37	82.15	82.52		
1H	15	0625	82.1	91.6	9.5	9.30	97.9	1	1.50	82.10	83.60	IW 140-150 HS 0-5	
								2	1.50	83.60	85.10		
								3	1.50	85.10	86.60		
								4	1.50	86.60	88.10		
								5	1.50	88.10	89.60		
								6	1.50	89.60	91.10		
1H	15	0735	91.6	101.1	9.5	9.96	105.0	CC	0.30	91.10	91.40	IW 140-150 HS 0-5	
								1	1.50	91.60	93.10		
								2	1.50	93.10	94.60		

Table 1 (continued).

Core	Date (September 1994)	Time (UTC)	Sub-bottom (m)		Cored (m)	Recovered (m)	Recovery (%)	Section	Length (m)	Depth (mbsf)		Samples
			Top	Bottom						Top	Bottom	
12H	15	0830	101.1	110.6	9.5	9.95	105.0	3	1.50	94.60	96.10	HS 0-5
								4	1.50	96.10	97.60	
								5	1.50	97.60	99.10	
								6	1.50	99.10	100.60	
								7	0.75	100.60	101.35	
								CC	0.21	101.35	101.56	
								1	1.50	101.10	102.60	
2	1.50	102.60	104.10									
13H	15	0925	110.6	120.1	9.5	9.91	104.0	3	1.50	104.10	105.60	IW 140-150 HS 0-5
								4	1.50	105.60	107.10	
								5	1.50	107.10	108.60	
								6	1.50	108.60	110.10	
								7	0.63	110.10	110.73	
								CC	0.32	110.73	111.05	
								1	1.50	110.60	112.10	
2	1.50	112.10	113.60									
14H	15	1020	120.1	129.6	9.5	9.83	103.0	3	1.50	113.60	115.10	HS 0-5
								4	1.50	115.10	116.60	
								5	1.50	116.60	118.10	
								6	1.50	118.10	119.60	
								7	0.60	119.60	120.20	
								CC	0.31	120.20	120.51	
								1	1.50	120.10	121.60	
2	1.50	121.60	123.10									
15H	15	1110	129.6	139.1	9.5	9.48	99.8	3	1.50	123.10	124.60	IW 140-150 HS 0-5
								4	1.50	124.60	126.10	
								5	1.50	126.10	127.60	
								6	1.50	127.60	129.10	
								7	0.56	129.10	129.66	
								CC	0.27	129.66	129.93	
								1	1.50	129.60	131.10	
2	1.50	131.10	132.60									
16H	15	1205	139.1	148.6	9.5	10.02	105.5	3	1.50	132.60	134.10	HS 0-5
								4	1.50	134.10	135.60	
								5	1.50	135.60	137.10	
								6	1.50	137.10	138.60	
								CC	0.48	138.60	139.08	
								1	1.50	139.10	140.60	
								2	1.50	140.60	142.10	
17H	15	1300	148.6	158.1	9.5	9.65	101.0	3	1.50	142.10	143.60	IW 140-150 HS 0-5
								4	1.50	143.60	145.10	
								5	1.50	145.10	146.60	
								6	1.50	146.60	148.10	
								7	0.66	148.10	148.76	
								CC	0.36	148.76	149.12	
								1	1.50	148.60	150.10	
2	1.50	150.10	151.60									
18X	15	1520	158.1	161.6	3.5	1.75	50.0	3	1.50	151.60	153.10	HS 0-5
								4	1.50	153.10	154.60	
								5	1.50	154.60	156.10	
								6	1.50	156.10	157.60	
								CC	0.65	157.60	158.25	
								1	1.45	158.10	159.55	
								CC	0.30	159.55	159.85	
Coring totals					161.6	160.5	99.30					
157-956B-1R	16	1140	157.1	166.6	9.5	5.33	56.1	1	1.50	157.10	158.60	IW 140-150 HS 0-5
								2	1.50	158.60	160.10	
								3	1.50	160.10	161.60	
								4	0.63	161.60	162.23	
2R	16	1320	166.6	176.1	9.5	1.77	18.6	CC	0.20	162.23	162.43	
3R	16	1425	176.1	185.7	9.6	0.09	0.9	1	1.50	166.60	168.10	
4R	16	1535	185.7	195.4	9.7	0.21	2.2	2	0.41	168.10	168.51	
5R	16	1645	195.4	205.1	9.7	8.53	87.9	1	0.09	176.10	176.19	
6R	16	1745	205.1	214.7	9.6	8.30	86.4	CC	0.21	185.70	185.91	IW 140-150 HS 0-5
								1	1.50	195.40	196.90	
								2	1.50	196.90	198.40	
								3	1.50	198.40	199.90	
								4	1.50	199.90	201.40	
								5	1.50	201.40	202.90	
								6	0.87	202.90	203.77	
CC	0.16	203.77	203.93									
								1	1.50	205.10	206.60	
								2	1.50	206.60	208.10	
								3	1.50	208.10	209.60	
								4	1.50	209.60	211.10	

Table 1 (continued).

Core	Date (September 1994)	Time (UTC)	Sub-bottom (m)		Cored (m)	Recovered (m)	Recovery (%)	Section	Length (m)	Depth (mbsf)		Samples
			Top	Bottom						Top	Bottom	
7R	16	1850	214.7	224.3	9.6	6.33	65.9	5	1.50	211.10	212.60	HS 0-5
								6	0.63	212.60	213.23	
								CC	0.17	213.23	213.40	
8R	16	2005	224.3	233.9	9.6	0.00	0.0	1	1.50	214.70	216.20	HS 0-5
								2	1.50	216.20	217.70	
								3	1.50	217.70	219.20	
								4	1.50	219.20	220.70	
								CC	0.33	220.70	221.03	
9R	16	2130	233.9	243.6	9.7	0.00	0.0					
10R	16	2355	243.6	253.2	9.6	7.58	78.9					
11R	17	0115	253.2	262.8	9.6	5.45	56.8	1	1.50	243.60	245.10	IW 135-150
								2	1.50	245.10	246.60	
								3	1.50	246.60	248.10	
								4	1.50	248.10	249.60	
								5	1.38	249.60	250.98	
CC	0.20	250.98	251.18									
12R	17	0230	262.8	272.4	9.6	6.91	72.0	1	1.50	253.20	254.70	HS 0-5
								2	1.50	254.70	256.20	
								3	1.50	256.20	257.70	
								4	0.73	257.70	258.43	
CC	0.22	258.43	258.65									
13R	17	0345	272.4	282.0	9.6	3.68	38.3	1	1.50	262.80	264.30	HS 0-5
								2	1.50	264.30	265.80	
								3	1.50	265.80	267.30	
								4	1.50	267.30	268.80	
								5	0.67	268.80	269.47	
CC	0.24	269.47	269.71									
14R	17	0505	282.0	291.7	9.7	5.59	57.6	1	1.50	272.40	273.90	HS 0-5
								2	1.50	273.90	275.40	
								3	0.46	275.40	275.86	
CC	0.22	275.86	276.08									
15R	17	0610	291.7	301.3	9.6	9.24	96.2	1	1.50	282.00	283.50	IW 130-150
								2	1.50	283.50	285.00	
								3	1.50	285.00	286.50	
								4	0.85	286.50	287.35	
CC	0.24	287.35	287.59									
16R	17	0705	301.3	310.8	9.5	8.09	85.1	1	1.50	291.70	293.20	HS 0-5
								2	1.50	293.20	294.70	
								3	1.50	294.70	296.20	
								4	1.50	296.20	297.70	
								5	1.50	297.70	299.20	
								6	1.50	299.20	300.70	
								7	0.24	300.70	300.94	
17R	17	0815	310.8	320.3	9.5	9.03	95.0	1	1.50	301.30	302.80	HS 0-5
								2	1.50	302.80	304.30	
								3	1.50	304.30	305.80	
								4	1.50	305.80	307.30	
								5	1.50	307.30	308.80	
								6	0.54	308.80	309.34	
CC	0.05	309.34	309.39									
18R	17	0925	320.3	329.9	9.6	9.70	101.0	1	1.50	310.80	312.30	IW 130-150
								2	1.50	312.30	313.80	
								3	1.50	313.80	315.30	
								4	1.50	315.30	316.80	
								5	1.50	316.80	318.30	
								6	1.50	318.30	319.80	
CC	0.03	319.80	319.83									
19R	17	1045	329.9	339.5	9.6	8.84	92.1	1	1.50	320.30	321.80	HS 0-5
								2	1.50	321.80	323.30	
								3	1.50	323.30	324.80	
								4	1.50	324.80	326.30	
								5	1.50	326.30	327.80	
								6	1.50	327.80	329.30	
								7	0.67	329.30	329.97	
CC	0.03	329.97	330.00									
20R	17	1210	339.5	349.2	9.7	9.40	96.9	1	1.50	329.90	331.40	HS 0-5
								2	1.50	331.40	332.90	
								3	1.50	332.90	334.40	
								4	1.50	334.40	335.90	
								5	1.50	335.90	337.40	
								6	1.32	337.40	338.72	
CC	0.02	338.72	338.74									
20R	17	1210	339.5	349.2	9.7	9.40	96.9	1	1.50	339.50	341.00	
								2	1.50	341.00	342.50	
								3	1.50	342.50	344.00	
								4	1.50	344.00	345.50	

Table 1 (continued).

Core	Date (September 1994)	Time (UTC)	Sub-bottom (m)		Cored (m)	Recovered (m)	Recovery (%)	Section	Length (m)	Depth (mbsf)		Samples
			Top	Bottom						Top	Bottom	
21R	17	1345	349.2	358.9	9.7	8.80	90.7	5	1.50	345.50	347.00	IW 130-150
								6	1.50	347.00	348.50	HS 0-5
								7	0.37	348.50	348.87	
								CC	0.03	348.87	348.90	
								1	1.50	349.20	350.70	
								2	1.50	350.70	352.20	
								3	1.50	352.20	353.70	
22R	17	1520	358.9	368.4	9.5	8.64	90.9	4	1.50	353.70	355.20	
								5	1.50	355.20	356.70	HS 0-5
								6	1.28	356.70	357.98	
								CC	0.02	357.98	358.00	
								1	1.50	358.90	360.40	
								2	1.50	360.40	361.90	
								3	1.50	361.90	363.40	
23R	17	1650	368.4	377.9	9.5	7.86	82.7	4	1.50	363.40	364.90	
								5	1.50	364.90	366.40	HS 0-5
								6	0.99	366.40	367.39	
								CC	0.15	367.39	367.54	
								1	1.50	368.40	369.90	
								2	1.50	369.90	371.40	
								3	1.50	371.40	372.90	
24R	17	1820	377.9	387.4	9.5	8.30	87.3	4	1.50	372.90	374.40	IW 130-150
								5	1.50	374.40	375.90	HS 0-5
								6	0.36	375.90	376.26	2 cm to Paleo
								1	1.50	377.90	379.40	
								2	1.50	379.40	380.90	
								3	1.50	380.90	382.40	
								4	1.50	382.40	383.90	
25R	17	1945	387.4	397.0	9.6	6.86	71.4	5	1.50	383.90	385.40	HS 0-5
								6	0.80	385.40	386.20	73-75 to Paleo
								1	1.50	387.40	388.90	
								2	1.50	388.90	390.40	
								3	1.50	390.40	391.90	
								4	1.50	391.90	393.40	
								5	0.62	393.40	394.02	
26R	17	2125	397.0	406.7	9.7	2.38	24.5	CC	0.24	394.02	394.26	
								1	1.50	397.00	398.50	
								2	1.67	398.50	400.17	HS 0-5
27R	17	2300	406.7	416.4	9.7	6.70	69.1	CC	0.21	400.17	400.38	
								1	1.50	406.70	408.20	
								2	1.50	408.20	409.70	
28R	18	0025	416.4	426.0	9.6	3.41	35.5	3	1.50	409.70	411.20	
								4	1.50	411.20	412.70	IW 130-150
								5	0.51	412.70	413.21	
								CC	0.19	413.21	413.40	
								1	1.50	416.40	417.90	
29R	18	0150	426.0	435.7	9.7	4.49	46.3	2	1.50	417.90	419.40	HS 0-5
								CC	0.41	419.40	419.81	
								1	1.50	426.00	427.50	
30R	18	0335	435.7	445.3	9.6	1.82	18.9	2	1.50	427.50	429.00	
								3	1.30	429.00	430.30	HS 0-5
								CC	0.19	430.30	430.49	
								1	1.50	435.70	437.20	
31R	18	0515	445.3	455.0	9.7	1.10	11.3	CC	0.32	437.20	437.52	HS 145-150
								1	1.25	445.30	446.55	
32R	18	0650	455.0	464.6	9.6	4.58	47.7	1	1.43	455.00	456.43	
								2	1.50	456.43	457.93	HS 0-5
								3	1.50	457.93	459.43	
								4	0.34	459.43	459.77	
33R	18	0815	464.6	474.3	9.7	4.12	42.5	1	1.26	464.60	465.86	
								2	1.50	465.86	467.36	IW 130-150/HS 145-150
								3	1.43	467.36	468.79	
								4	0.13	468.79	468.92	
34R	18	0935	474.3	483.9	9.6	2.86	29.8	1	1.37	474.30	475.67	
								2	1.50	475.67	477.17	
								3	0.05	477.17	477.22	HS 0-5
35R	18	0110	483.9	493.6	9.7	4.88	50.3	1	1.43	483.90	485.33	
								2	1.47	485.33	486.80	HS 105-108
								3	1.41	486.80	488.21	
								4	0.69	488.21	488.90	
36R	18	1230	493.6	503.3	9.7	2.30	23.7	1	1.44	493.60	495.04	
								2	1.00	495.04	496.04	HS 105-110
37R	18	1435	503.3	512.9	9.6	3.57	37.2	1	1.50	503.30	504.80	HS 80-82

Table 1 (continued).

Core	Date (September 1994)	Time (UTC)	Sub-bottom (m)		Cored (m)	Recovered (m)	Recovery (%)	Section	Length (m)	Depth (mbsf)		Samples
			Top	Bottom						Top	Bottom	
38R	18	1610	512.9	522.6	9.7	4.33	44.6	2	1.50	504.80	506.30	IW 20-45
								3	0.88	506.30	507.18	
								1	1.38	512.90	514.28	HS 0-5
2	1.50	514.28	515.78									
3	1.44	515.78	517.22									
39R	18	1740	522.6	532.3	9.7	4.30	44.3	4	0.30	517.22	517.52	HS 0-5
								1	1.28	522.60	523.88	
								2	1.20	523.88	525.08	
								3	1.20	525.08	526.28	
40R	18	1915	532.3	541.9	9.6	2.79	29.0	4	0.92	526.28	527.20	HS 0-5
2	1.47	533.80	535.27									
41R	18	2115	541.9	551.5	9.6	3.35	34.9	1	1.47	541.90	543.37	HS 0-5
2	1.40	543.37	544.77									
42R	18	2250	551.5	561.1	9.6	3.53	36.8	3	0.64	544.77	545.41	HS 78-83
								1	1.41	551.50	552.91	
								2	1.44	552.91	554.35	
43R	19	0045	561.1	570.7	9.6	8.07	84.0	3	0.78	554.35	555.13	HS 0-2
								1	1.50	561.10	562.60	
								2	1.50	562.60	564.10	
3	1.50	564.10	565.60									
4	1.50	565.60	567.10									
5	1.50	567.10	568.60									
44R	19	0320	570.7	580.4	9.7	7.74	79.8	6	0.57	568.60	569.17	HS 0-2
								1	1.50	570.70	572.20	
								2	1.50	572.20	573.70	
								3	1.38	573.70	575.08	
								4	1.50	575.08	576.58	
								5	1.45	576.58	578.03	
45R	19	0705	580.4	590.0	9.6	4.82	50.2	6	0.41	578.03	578.44	HS 0-2
								1	1.20	580.40	581.60	
								2	1.29	581.60	582.89	
								3	1.31	582.89	584.20	
								4	0.88	584.20	585.08	
								CC	0.23	585.08	585.31	
46R	19	1905	590.0	599.6	9.6	5.11	53.2	1	1.29	590.00	591.29	IW 109-129/HS 124-129
								2	1.27	591.29	592.56	
								3	1.50	592.56	594.06	
								4	1.40	594.06	595.46	
47R	19	2235	599.6	609.3	9.7	3.57	36.8	1	1.46	599.60	601.06	HS 0-2
								2	1.49	601.06	602.55	
								3	0.80	602.55	603.35	
48R	20	0125	609.3	619.0	9.7	5.94	61.2	1	1.50	609.30	610.80	HS 0-2
								2	1.28	610.80	612.08	
								3	1.39	612.08	613.47	
								4	1.25	613.47	614.72	
								5	0.52	614.72	615.24	
49R	20	0300	619.0	628.7	9.7	6.58	67.8	1	1.50	619.00	620.50	HS 0-2
								2	1.50	620.50	622.00	
								3	1.46	622.00	623.46	
								4	1.32	623.46	624.78	
								5	0.80	624.78	625.58	
50R	20	0440	628.7	638.2	9.5	6.20	65.2	1	1.43	628.70	630.13	HS 0-2
								2	1.47	630.13	631.60	
								3	1.43	631.60	633.03	
								4	1.50	633.03	634.53	
51R	20	0640	638.2	647.6	9.4	9.89	105.0	1	1.05	638.20	639.25	HS 0-2
								2	1.42	639.25	640.67	
								3	1.50	640.67	642.17	
								4	1.50	642.17	643.67	
								5	1.44	643.67	645.11	
								6	1.34	645.11	646.45	
								7	1.40	646.45	647.85	
								8	0.24	647.85	648.09	
52R	20	0930	647.6	657.3	9.7	5.96	61.4	1	1.41	647.60	649.01	HS 0-2
								2	1.50	649.01	650.51	
								3	1.40	650.51	651.91	
								4	1.42	651.91	653.33	
								5	0.23	653.33	653.56	
53R	20	1215	657.3	666.9	9.6	6.00	62.5	1	1.50	657.30	658.80	HS 0-2
								2	1.50	658.80	660.30	
								3	1.50	660.30	661.80	
								4	1.50	661.80	663.30	
54R	20	1510	666.9	676.6	9.7	1.85	19.1	1	1.50	657.30	658.80	HS 0-2
								2	1.50	658.80	660.30	
								3	1.50	660.30	661.80	
								4	1.50	661.80	663.30	

Table 1 (continued).

Core	Date (September 1994)	Time (UTC)	Sub-bottom (m)		Cored (m)	Recovered (m)	Recovery (%)	Section	Length (m)	Depth (mbsf)		Samples
			Top	Bottom						Top	Bottom	
55R	20	1825	676.6	686.3	9.7	4.78	49.3	1	1.45	666.90	668.35	
								2	0.74	668.35	669.09	
56R	20	2205	686.3	696.0	9.7	4.64	47.8	1	1.46	676.60	678.06	
								2	1.46	678.06	679.52	
								3	1.47	679.52	680.99	
57R	21	0020	696.0	703.5	7.5	1.21	16.1	1	1.47	686.30	687.77	
								2	1.46	687.77	689.23	
								3	1.47	689.23	690.70	
								4	0.24	690.70	690.94	
Coring totals					546.4	297.4	54.40					

Notes: Hole 956A located at 27°36.905'N, 16°9.797'W. Water depth from sea surface = 3441.9 m. Hole 956B located at 27°36.895'N, 16°9.797'W. Water depth from sea surface = 3441.9 m. HS = headdress samples; IW = interstitial water samples.

ment with foraminifers. Minor diatoms are present within the mixed sediments of Subunit Ia. The sediments are generally moderately bioturbated and slightly mottled.

Minor lithologies in Subunit Ia include bioclastic sand, nannofossil ooze, and one pumiceous bed. Bioclastic sands are the most common minor lithology (Fig. 4) and consist of thick to very thick beds of coarse to very coarse shell debris of shallow-water marine organisms. Angular fragments of bivalves, scaphopods, corals, and echinoderm spines are abundant with minor whole bivalve and scaphopod shells. In Cores 157-956A-1H and 157-956A-2H, bioclastic fragments constitute 95% to 99% of the sand component, with the remainder consisting of dark volcanic lithic fragments. In Core 157-956A-3H, bioclastic fragments constitute 80%–90%, and pumice, alkali feldspar, other crystals, and lithic fragments 10%–20%. Core 157-956A-3H contains a distinctive thick (30 cm), orange-brown pumice lapilli bed (Fig. 7) that fines upward to zeolitic ash. Minor interbeds of structureless, light gray-brown nannofossil ooze also occur throughout the unit.

Strongly tilted and folded bedding, indicative of soft sediment deformation and slumping, are common in Subunit Ia. Slumped and convoluted intervals range between 0.8 and 7.2 m. Isolated whole and broken bivalve shells and coral fragments and pumice clasts are present within the slumped sequences of clayey nannofossil mixed sediment. Siliciclastic interbeds are commonly discontinuous and folded.

Subunit Ib

Interval: Sections 157-956A-5H-4 to 157-956A-9H-3

Depth: 37.5–76.5 mbsf

Age: Pleistocene to late Pliocene

Subunit Ib is 39 m thick. The dominant lithology is mottled pale brown to greenish-brown, thin to very thick bedded, clayey nannofossil mixed sediment with foraminifers. Diatoms are sporadically present in the upper parts of this unit. Foraminifers decrease in abundance in the lower part of the subunit with the major lithology changing to clayey nannofossil mixed sediment in Core 157-956A-9H. Disseminated pyrite and pyritic concretions are common.

The minor lithologies in Subunit Ib differ significantly from those in Subunit Ia, mainly in the absence of bioclastic sand and a sharp increase in volcanic material (Fig. 5). Minor interbeds of foraminifer sand and silt with pumice occur in the upper part of Subunit Ib. However, the majority of the interbedded sediments consist of pumice sand, basaltic lapilli, vitric silt, and crystal lithic sand. These volcanoclastic interbeds are thinly laminated to thinly bedded, normally

graded with sharp bases. Some pumice-rich deposits are medium bedded and show reverse grading of well-rounded pumice lapilli (Fig. 8). Other pumice deposits are massive, well sorted, and consist almost exclusively of millimeter-size felsic pumice grains (Fig. 9). A 13-cm-thick bed of basaltic lapilli occurs at the top of Core 157-956A-6H-1 and consists of black to red, aphyric, vesicular to nonvesicular basalt with subround to subangular clasts and minor barnacle fragments. Several vitric ash layers are also present in Subunit Ib and are characterized by sharp basal contacts, bioturbated upper contacts, a high proportion of felsic glass shards, and a low amount of biogenic material. In Section 157-956A-9H-3, two vitric ash layers are in direct contact (Fig. 10).

Strongly folded beds of clayey nannofossil mixed sediment with foraminifers occur throughout Subunit Ib and range from 4.2 to 6 m thick. Interbeds of the minor lithologies present in these slumped intervals are strongly folded, discontinuous, and have diffuse contacts.

Subunit Ic

Interval: Sections 157-956A-9H-4 to 157-956A-17H-CC

Depth: 76.5–158 mbsf

Age: late Pliocene

Subunit Ic is 81.5 m thick. The dominant lithology is mottled gray and greenish gray, thin to thick bedded, clayey nannofossil mixed sediment. Pyrite is dispersed throughout the unit.

A significant change in the minor lithology, from volcanic-rich interbeds to quartz-rich interbeds, was used to separate Subunits Ib and Ic. Although minor pumice silt and lapilli and vitric ash with nannofossils occur in the upper part of Subunit Ic, most of the minor lithologies consist of calcareous quartz sand with lithics and foraminifer sand. These interbeds are generally thinly laminated to thinly bedded and are normally graded with sharp bases. A distinctive feature of many of these layers is the occurrence of multiple silt laminae at the base of individual graded sequences of nannofossil mixed sediment to silt (Fig. 11).

Convoluted bedding and slump folds of clayey nannofossil mixed sediment are common in Subunit Ic. Slumped and disrupted sequences range in thickness from 2 to 20 m. Lithologies of the minor interbeds within the slumped intervals differ from those of the nondisrupted beds that occur above and below these intervals. One slumped interval in Cores 157-956A-12H and 157-956A-13H has minor interbeds of crystal lithic silt and clay with nannofossils. Another slumped interval in Sections 157-956A-14H-6 and 157-956A-14H-CC consists of convoluted clayey nannofossil mixed sediment with no interbeds.

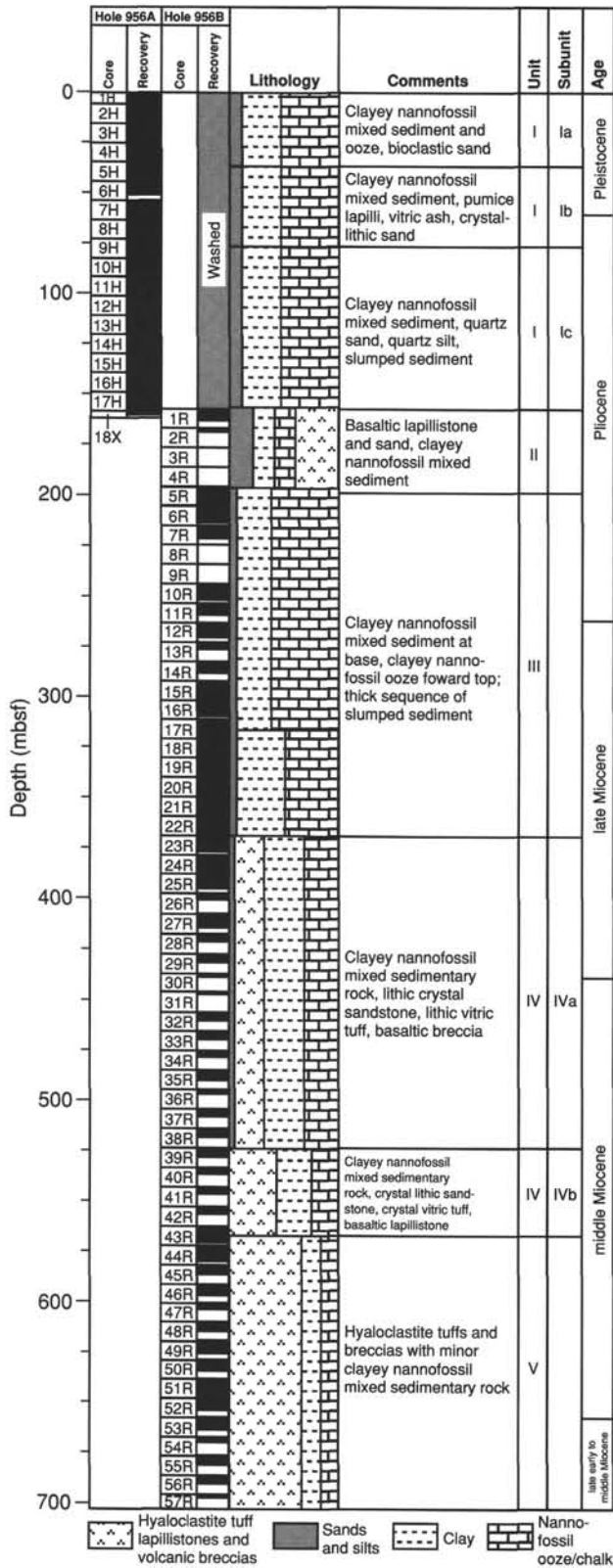


Figure 4. Lithologic summary for Holes 956A and 956B showing the main lithologic units identified with age and a generalized graphic lithology.

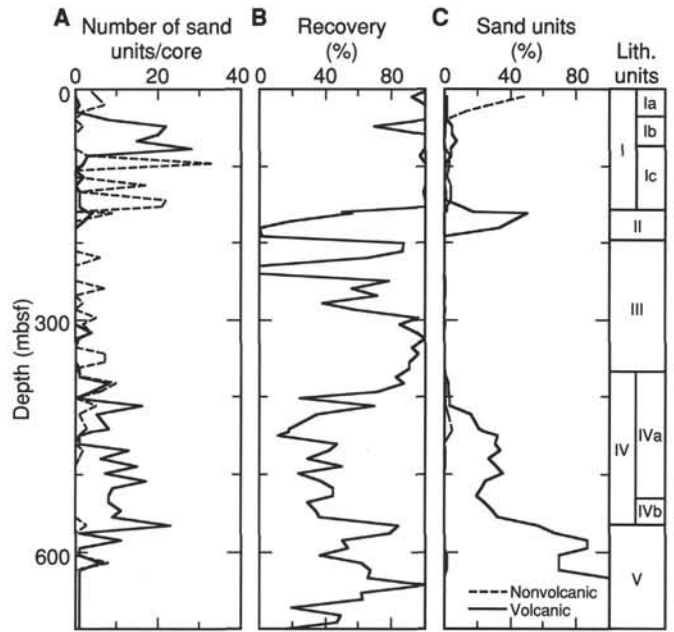


Figure 5. Variation in (A) the number of coarse volcaniclastic layers per core, (B) the core recovery as a function of depth below seafloor for Site 956, and (C) the percentage of coarse (greater than sand size) volcaniclastic and non-volcaniclastic layers per core.

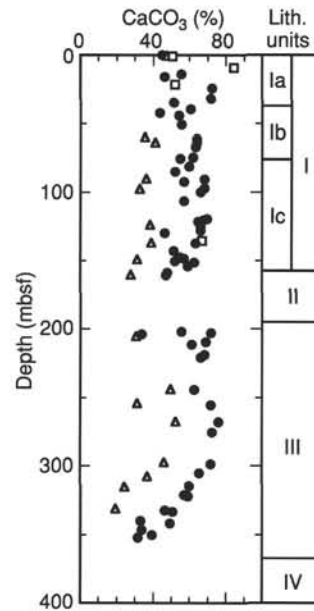


Figure 6. Variation in the calcium carbonate content of pelagic sediment (filled circles), turbidite muds (open triangles), and silt or sand bases of turbidites (open squares) as a function of depth below seafloor at Site 956.

Unit II

Interval: Sections 157-956A-18X-1 to 157-956B-5R-1
 Depth: 158.1–196.9 mbsf
 Age: late Pliocene to early Pliocene

Unit II is 38.8 m thick. It consists dominantly of light gray clayey nannofossil mixed sediment with foraminifers, basaltic lapillistone,

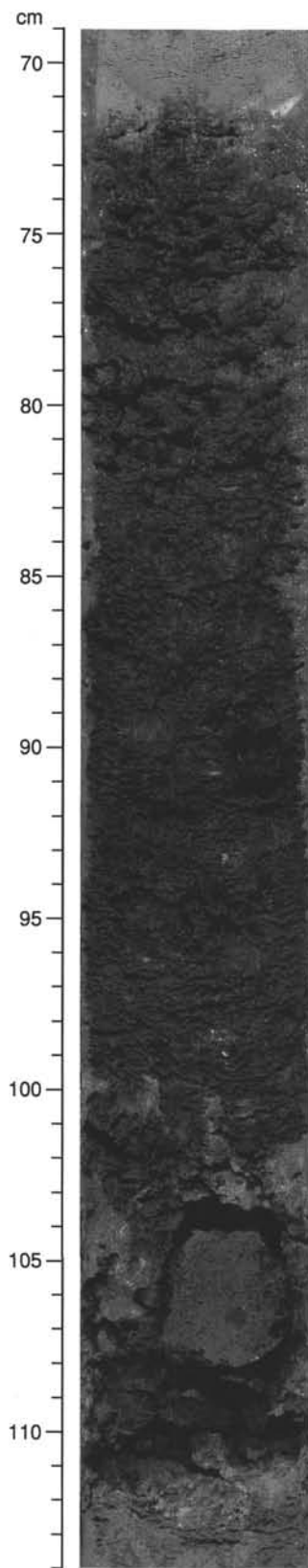


Figure 7. Orange-brown pumice lapilli in Subunit Ia, fining upward into zeolitic ash. Interval 157-956A-3H-5, 69–114 cm.

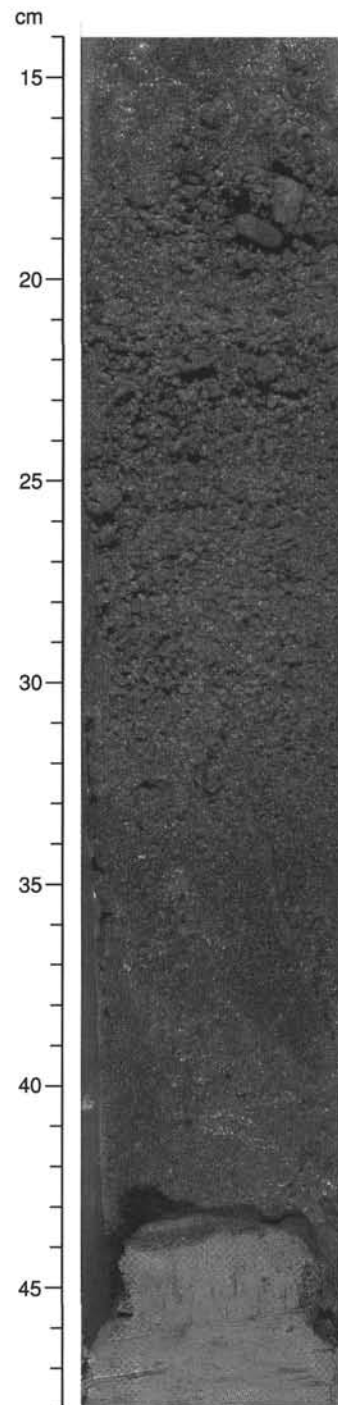


Figure 8. Reversely graded pumice lapilli deposit in Subunit Ib. Note the well-rounded nature of pumice fragments in the upper part of the deposit. Interval 157-956A-9H-2, 14–48 cm.

nannofossil clay, and quartz silts and sands. It is distinguished from Subunit Ic by a reduction in felsic volcanic components and an increase in coarse mafic material. The recovery of this unit was very low and most likely reflects the high proportion of sand-size components (Fig. 5).

Gray clayey nannofossil mixed sediment occurs as thin to medium bedded units that are commonly bioturbated and mottled through-

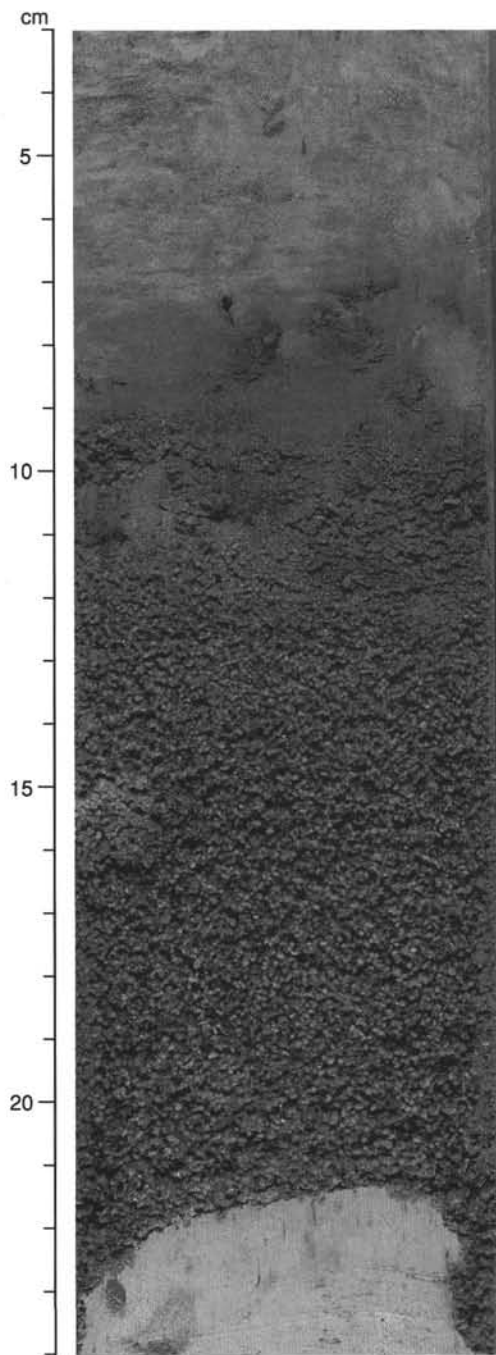


Figure 9. Well-sorted pumice lapilli deposit in Subunit I. Note the massive structure and sharp basal contact. Interval 157-956A-9H-3, 3–24 cm.

out. Calcium carbonate data indicate that these sediments are generally close to the classification division between mixed sediment (<60% CaCO₃) and ooze (>60% CaCO₃; Fig. 6). Consequently, it is difficult to classify these sediments from visual and smear slide analysis alone, because of the significant background flux of volcanic and continentally derived material. Most of the sediments are described as mixed however.

Interbedded with nannofossil mixed sediments are numerous graded intervals consisting of darker gray clayey nannofossil mixed sediment or nannofossil claystone that grades into silt or sand bases. The clayey parts of these turbidite units have generally lower CaCO₃

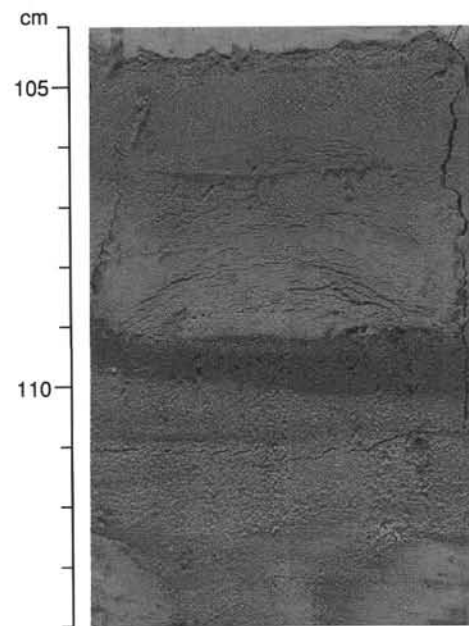


Figure 10. Two vitric ash layers in close contact. The boundary between the two occurs at 109 cm and is defined by a change in grain size and color of the layers. Interval 157-956A-9H-3, 104–114 cm.

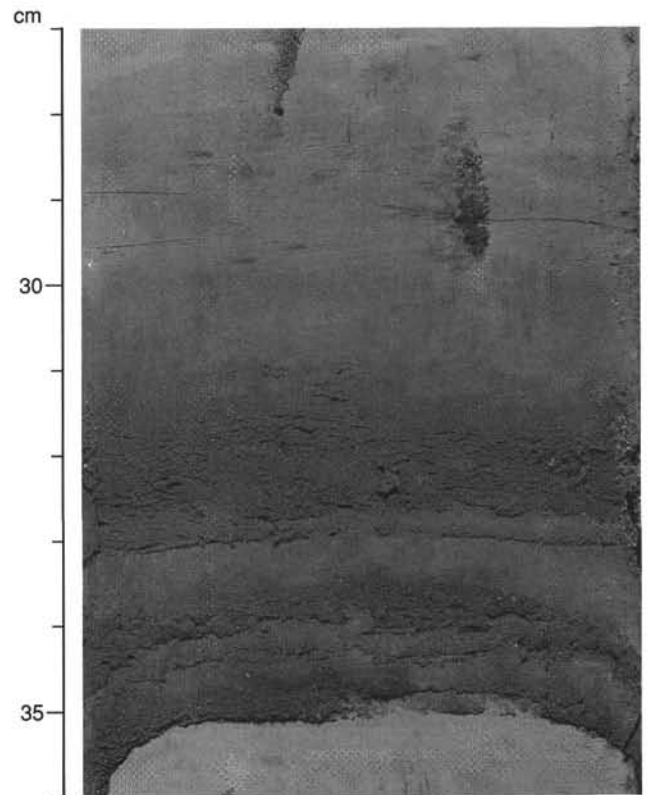


Figure 11. Graded nannofossil mixed sediment sequence with multiple silt laminae at the base. Interval 157-956A-11H-2, 27–36 cm.

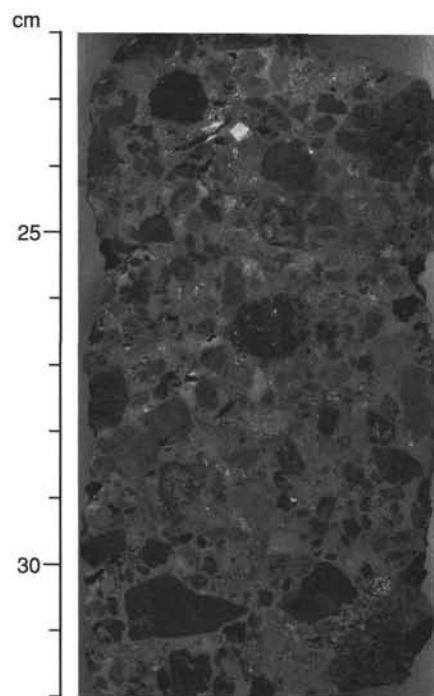


Figure 12. Basaltic lapillistone from Unit II. The deposit consists of angular to subangular clasts of basalt and phonolite in a fine-grained matrix. Interval 157-956B-2R-1, 22–32 cm.

than the pelagic mixed sediments (Fig. 6). Silt and sand bases of the graded layers are composed of rounded quartz, often with a brownish-orange staining, feldspar, and fragments of foraminifers. Most layers have a sharp base and a moderately bioturbated top.

Basaltic lapillistone occurs as thick to very thick beds that are either structureless or normally graded (Fig. 12). They consist dominantly of aphyric basalt clasts that are supported in a greenish-gray matrix and are poorly sorted. The matrix is relatively fine grained (sandy-silt) and contains crystals of clinopyroxene, feldspar, small lithic fragments, and calcareous debris. Some of the basalt clasts are plagioclase-phyric, or more rarely, olivine-clinopyroxene phyric. Most are angular to subangular, with a few rounded to subrounded types. A substantial number of the basalt clasts are moderately vesicular. In Core 157-956B-2R basalt clasts at the base of a lapillistone deposit are up to 5 cm in diameter.

Beneath a basaltic lapillistone in Core 157-956B-2R a sequence of slumped sediment contains scattered clasts of welded ignimbrite (Fig. 13). The clasts display eutaxitic texture with fiamme up to 3 cm in length.

Unit III

Interval: Sections 157-956B-5R-2 to 157-956B-22R-CC
Depth: 196.9–367.5 mbsf
Age: early Pliocene to late Miocene

Unit III is 170.6 m thick. Dominant lithologies include greenish-gray clayey nannofossil mixed sediment and clayey nannofossil ooze. In the lower part of the unit these lithologies are present as mixed sedimentary rock and chalk. Minor lithologies include quartz-rich silt and sand, foraminifer sand, lithic-crystal silt and sand, and nannofossil clay. The unit is distinguished from Unit II by the low abundance of sand deposits and the very common occurrence of slumped sediment (Fig. 5).

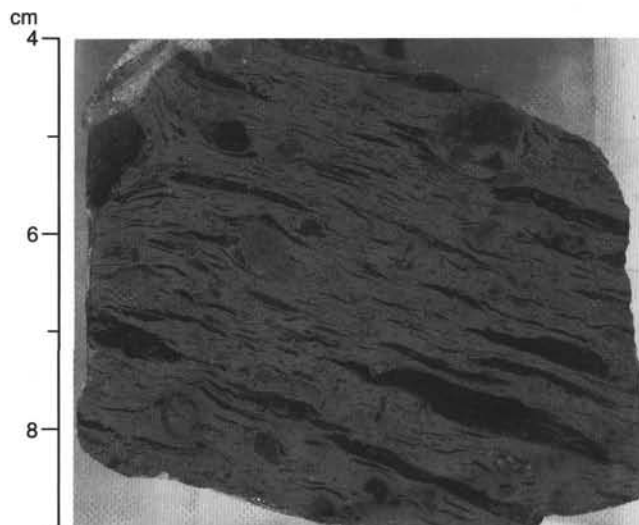


Figure 13. Clast of welded ignimbrite. Dark elongated bands are flattened pumice (fiamme). Note the deformation of fiamme around dense lithic clasts. Interval 157-956B-3R-1, 4–9 cm.

The most common type of sediment in Unit III is greenish gray clayey nannofossil mixed sediment or sedimentary rock. It is usually thin to very thick bedded, moderately bioturbated, and commonly contains abundant dark silt and sand particles dispersed over decimeter scale intervals. The sediment is almost always mottled with various shades of green, purple, or dark gray. This mottling most often takes the form of color banding with individual bands ranging from a few millimeters to a few centimeters in thickness. Nannofossil ooze also occurs as thin to thick bedded layers and displays many of the same sedimentary and mottling characteristics as the mixed sediments.

Bluish green to olive green clayey nannofossil mixed sediment and nannofossil clay occur as thin beds with sharp bases and bioturbated tops. In many cases these beds have a dark silt or sand base that consists of quartz, feldspar, lithics and foraminifer fragments. The dark color of these basal deposits is caused by the presence of abundant micronodules. Most are spherical with diameters ranging from a few tens of micrometers to ~100 μm , and they consist of Fe-Mn oxides and hydroxides (Rothwell, 1989).

Foraminifer sands, crystal-lithic sands, and quartz sands constitute a minor proportion of Unit III and occur mainly as very thin or thin bedded deposits. Foraminifer sands are commonly parallel laminated, light colored, and have sharp upper and lower contacts. The other sands more commonly form the basal units of graded sequences, but they may also occur as discrete layers.

One of the most distinctive features of Unit III is the very high proportion of slumped sediment. There are at least three different types of slumped facies that can be recognized in this unit. The first consists of clayey nannofossil mixed sediment that has horizontal to subhorizontal color banding a few millimeters to several centimeters thick. These bands commonly have a crenulated and irregular appearance and are offset by small faults (Fig. 14). A second variety consists of clayey nannofossil mixed sediment with color banding that is pervasively folded and contorted (Fig. 15). The folding structures indicate that the sediment was soft and unconsolidated at the time of deformation. Faulting is also common in this type of sequence. The third, and less common type, involves clayey nannofossil mixed sediment, lithic-crystal sand, and lapillistone (Fig. 16). This type is characterized by more indurated-appearing clasts of sediment being mixed with a matrix containing a poorly sorted combination of

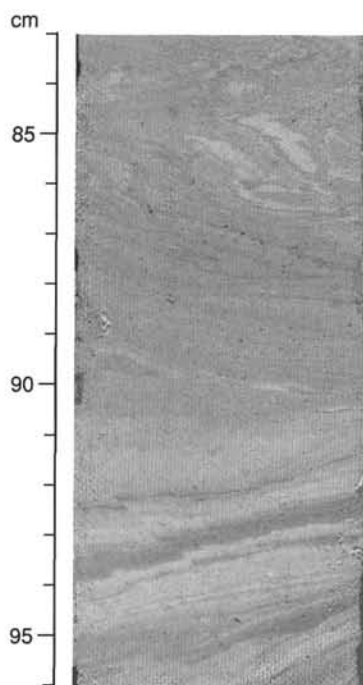


Figure 14. Slumped sediment showing subhorizontal color banding offset by small faults in Unit III. Interval 157-956B-12R-2, 83–96 cm.

clayey mixed sediment, sand, and angular, green volcanic clasts, probably phonolitic, up to several centimeters in diameter.

Unit IV

Interval: Sections 157-956B-23R-1 to 157-956A-43R-2
Depth: 367.5–564.1 mbsf
Age: middle Miocene

Unit IV is 196.6 m thick. The dominant lithologies include greenish-gray clayey nannofossil mixed sedimentary rock, crystal-lithic sandstone, and vitric tuffs, which are interbedded with lesser amounts of calcareous sandstone, mud-clast breccia, basaltic breccia, and minor mafic lapillistone. The key feature of this unit is the high proportion of coarse felsic volcanoclastic material, its greenish color, and less numerous intervals of slumped sediment.

Subunit IVa

Interval: Sections 157-956B-23R-1 to 157-956B-38R-4
Depth: 367.5–517.5 mbsf
Age: late to middle Miocene

Subunit IVa is 150 m thick. It consists of greenish gray clayey nannofossil mixed sedimentary rock and nannofossil chalk interbedded with calcareous sandstone, mud-clast breccia, quartz siltstone, basaltic breccia, lithic-crystal sandstone, claystone, and lithic-vitric tuff (Fig. 5).

Clayey nannofossil mixed sedimentary rock is the dominant lithology of Subunit IVa and occurs as thin to thick bedded units. It varies in color from light greenish gray to dark green with increasing depth. Most beds are moderately bioturbated and mottling is common. Nannofossil chalk also occurs as thin to medium beds but decreases in abundance with depth at the expense of green to dark green claystone.

Crystal-lithic sandstones are found as thin to thick bedded deposits that are usually structureless and relatively well sorted. They con-

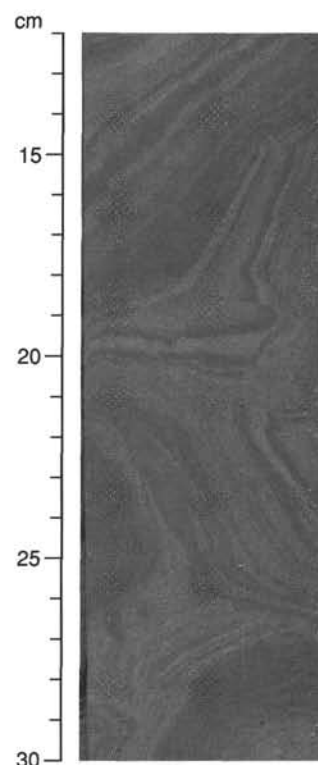


Figure 15. Pervasive folding and faulting of color banding in slumped clayey nannofossil mixed sediment from Unit III. Interval 157-956B-18R-6, 12–30 cm.

sist of small basalt and phonolite clasts, crystals of clinopyroxene, amphibole, feldspar, and some pumice. Red oxidized clasts make up a minor part of these deposits along with calcareous fragments.

In the lower part of Subunit IVa, lithic-vitric tuffs occur as medium to thick bedded deposits. They are well sorted, sometimes normally graded, and some are parallel laminated. The dominant components are dark green glassy felsic clasts, glass shards, pumice, feldspar, amphibole, and some red oxidized clasts. Pore spaces in the deposits are filled with zeolites and some of the induration is the result of zeolite cement. These tuffs are often associated with medium bedded dark green claystone with planar lamination.

Calcareous sands are a relatively minor component and usually occur as thin beds composed of a mixture of foraminifers, crystals, and lithics. Sporadic quartz-rich siltstones occur as very thin to thin bedded layers at the base of nannofossil mixed sedimentary rock sequences.

The amount of slumped sediment in Subunit IVa is much less than in Unit III. However, there are several intervals of mud-clast breccia in Cores 157-956B-26R, 157-956B-27R, 157-956B-28R, and 157-956B-29R. The intervals are medium to thick bedded and consist of pebble-size clasts of clayey nannofossil mixed sedimentary rock supported in a poorly sorted matrix of mixed sedimentary rock, volcanoclastic sand, and small clasts of subangular to angular phonolite (Fig. 17).

Subunit IVb

Interval: Sections 157-956B-39R-1 to 157-956B-43R-2
Depth: 522.6–564.1 mbsf
Age: middle Miocene

Subunit IVb is 41.5 m thick. It consists of pale green clayey nannofossil mixed sedimentary rock interbedded with crystal vitric tuff,

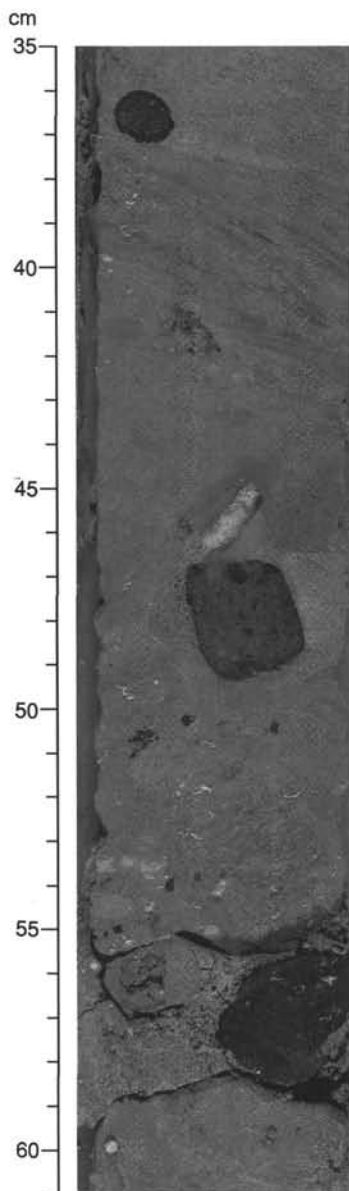


Figure 16. Chaotic mixture of clayey nannofossil mixed sediment, volcaniclastic sand, and clasts of basalt and phonolite from Unit III. Interval 157-956B-22R-6, 35–61 cm.

crystal lithic sandstone, lithic-crystal sandstone, and lapillistone. The unit is distinguished from Unit IVa by the increased abundance of vitric tuff and reduced amount of nonvolcanic sedimentary rock (Fig. 5).

Clayey nannofossil mixed sedimentary rock is the dominant lithology of Subunit IVb and occurs as thin to thick bedded units. It varies in color from pale green to dark green with increasing depth. Most beds are moderately bioturbated and commonly contain silt- to sand-size volcanic lithics and crystals, pumice and volcanic glass shards (Fig. 18).

Crystal vitric tuff and crystal-lithic sandstones are found as thin to thick bedded deposits that are usually parallel laminated to massive and moderately sorted. They consist of volcanic lithics, crystals of amphibole, alkali feldspar, light green clinopyroxene, biotite, and pumice and glass shards. Red oxidized vesicular clasts make up a minor part of these deposits along with calcareous fragments.

Vitric tuffs are common throughout Subunit IVb. They occur as medium to thick bedded deposits, are well sorted, sometimes normal-

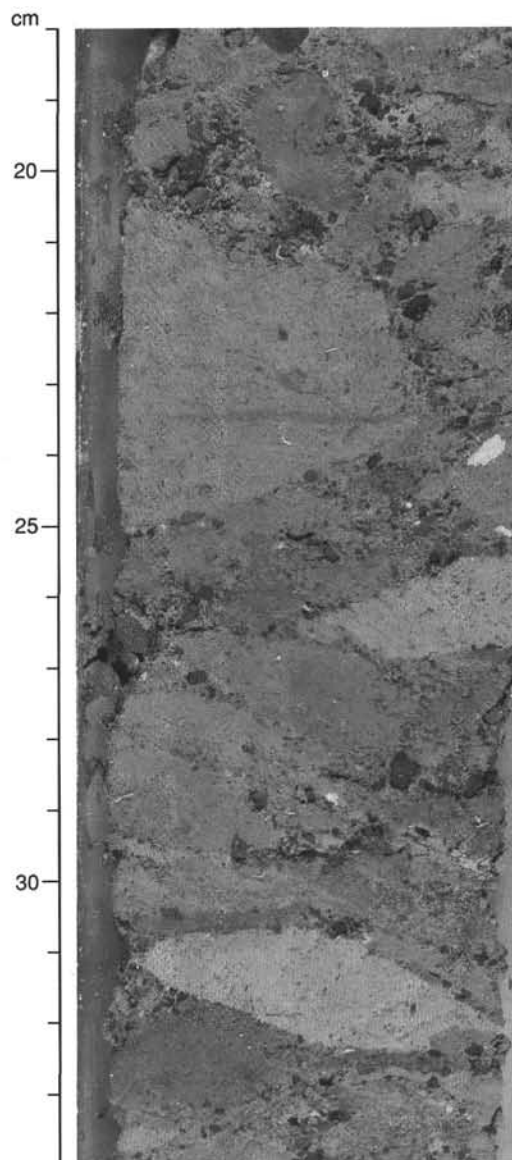


Figure 17. Mud-clast breccia in Subunit IVa. The deposit consists of clasts of clayey nannofossil mixed sediment in matrix of very poorly sorted nannofossil clay with basalt and phonolite fragments up to 1 cm in diameter. Interval 157-956B-27R-3, 18–34 cm.

ly graded, and some are parallel laminated. The dominant components are glass shards, pumice, feldspar, amphibole, light green clinopyroxene, and some red oxidized vesicular clasts. Pore spaces in the deposits are filled with zeolites and some of the induration is the result of zeolite cement. Crystals and volcanic lithics occur as scattered grains in the calcareous pelagic sediments.

Calcareous sands are a minor component and usually occur as thin beds composed of a mixture of foraminifers, crystals, and lithics. Slumped sediment is absent in Subunit IVb.

Unit V

Interval: Sections 157-956B-43R-3 to 157-956B-57R-1

Depth: 564.1–704 mbsf

Age: middle Miocene

Unit V is 140 m thick. This unit consists mostly of hyaloclastite tuff and lapillistone and basaltic breccia with minor interbeds of nan-

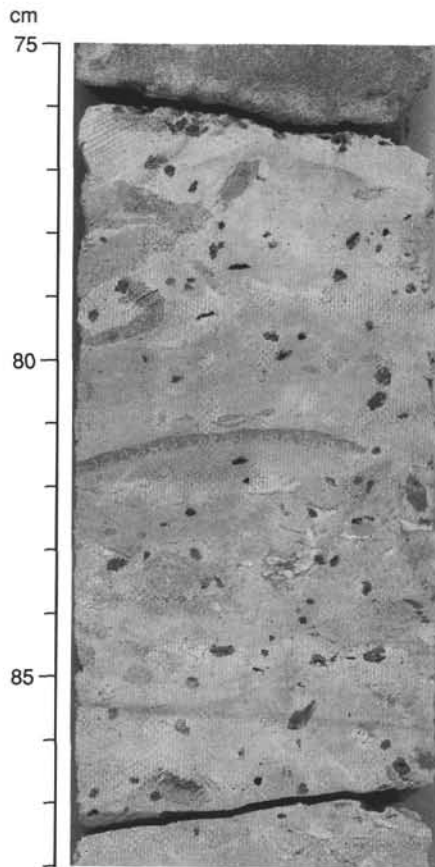


Figure 18. Dispersed pumice clasts (small black pieces) in clayey nannofossil mixed sediment from Subunit IVa. Interval 157-956B-34R-1, 75–88 cm.

nofossil claystone with foraminifers. Unit V is distinguished from Unit IV by the change in composition to basaltic hyaloclastites, lapillistone, and breccia.

Hyaloclastite tuffs occur as dark green, normally graded, thickly bedded sequences that commonly overlie hyaloclastite lapillistone. The hyaloclastite lapillistones occur as very thick to thick, poorly sorted, clast- to matrix-supported beds that are normally graded. Lapillistones are composed of dark green to dark purple, subangular basalt clasts (Fig. 19). Nonvesicular lapilli comprise ~60%–75% and vesicular lapilli ~25%–40% of the clasts. Aphyric clasts are dominant in the upper part of this unit but pyroxene-phyric and olivine (altered)-phyric clasts dominate in the lower unit (Core 157-956B-46R). Rare rip-up clasts of clayey nannofossil mixed sedimentary rock with foraminifers occur within the hyaloclastite lapillistone.

Basaltic breccias are very thickly bedded and structureless, poorly sorted, and clast supported. Clasts are composed mostly of dark purple (and rare red) nonvesicular and olivine (pseudomorphs) and pyroxene phyric-basalt. Many of the larger clasts are vesicular. The matrix of the breccia contains fine lithic fragments of basalt, altered vesicular shards, zeolites, and noncalcareous clay.

Minor interbeds of nannofossil claystone with foraminifers are present throughout the unit. These sediments are laminated to medium bedded and are commonly moderately to strongly bioturbated. Many of the lower bounding surfaces of the claystones are sharp and consist of thinly laminated foraminifer sandstone, lithic foraminifer sandstone and siltstone, foraminifer crystal lithic sandstone and siltstone, and vitric siltstone.

Depositional History

The oldest sediments recovered at Site 956 are mid-Miocene (Unit V) and consist of basaltic breccia and hyaloclastite tuff. At this

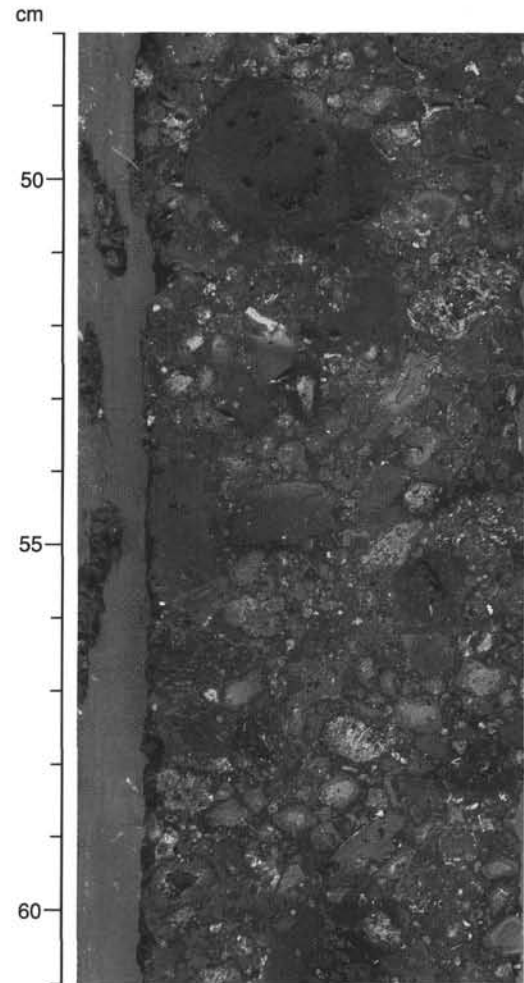


Figure 19. Basaltic lapillistone from Unit V. Basalt fragments are vesicular, nonvesicular, plagioclase-phyric, and clinopyroxene-olivine-phyric. The matrix consists of zeolites and nannofossil claystone with scattered carbonate fragments. Interval 157-956B-44R-4, 48–61 cm.

time the influx of volcanoclastic material was extremely high (Fig. 5). Deposition of this material took place primarily as debris flows that produced poorly to moderately sorted, thick to very thick bedded units with normally graded clasts. Interbeds of clayey nannofossil mixed sediment and foraminifer crystal sand are restricted to Cores 157-956B-43R, 157-956B-45R, 157-956B-48R, and 157-956B-49R.

The breccias contain abundant clasts of vesicular basalt and red oxidized scoriaceous fragments indicating derivation from the products of subaerial volcanism. However, these units also contain a moderate amount of altered, vesicular hyaloclastite grains suggesting that hydroclastic eruptions were taking place at this time as well and that products of both submarine and subaerial volcanism were mixed together prior to deposition of the coarse clastic units. Many lithic clasts are subrounded to rounded and thus indicate reworking of subaerial volcanic rocks.

Deposition of hyaloclastite tuffs and basaltic breccias may have been interrupted by the formation of felsic vitric tuffs with interbedded clayey nannofossil mixed sediment. Precise dating of this interval is difficult and it is overlain by another thick sequence of hyaloclastite tuffs and breccias.

In Core 157-956B-43R a volcanoclastic unit has been tentatively correlated with the middle Miocene P1 ignimbrite on Gran Canaria based on its mineralogical assemblage. On land this unit has been dated at 14 Ma (Bogaard et al., 1988) and it marks the beginning of the voluminous Mogan stage of explosive volcanism on Gran Canaria

(Schmincke, 1994; Freundt and Schmincke, 1995). The explosive volcanic activity supplied abundant felsic volcanoclastic material to the sea as shown by the deposition of thick bedded crystal vitric tuffs, crystal lithic sandstone, and lapillistone at Site 956. A distinctive feature of this material is that despite its age (~13–14 Ma) there is abundant fresh glass in the form of shards and small pumices. Some of the material was reworked and deposited by turbidity currents whereas at least some was associated with the entrance of pyroclastic flows into the sea with subsequent transformation to water-rich sediment gravity flows. In general, the flux of coarse volcanoclastic material during this time was quite high (Fig. 5), reflecting the voluminous nature of the mid-Miocene Mogan activity.

The supply of felsic volcanoclastic material continued at high levels until ~13 Ma (Fig. 5). A change in the composition of the material is shown in the cores as a reduction in abundance of vitric tuffs with unaltered glass shards (Subunit IVa/IVb boundary). This change most likely corresponds to the transition from Mogan (trachytic to rhyolitic composition) to Fataga (trachyphonolitic composition) activity that occurred at ~13.0 Ma (Schmincke, 1994).

At 9.5 Ma the influx of volcanoclastic material abruptly diminished (Fig. 5). This coincides well with the end of Fataga volcanism and marks the beginning of a prolonged volcanic hiatus on Gran Canaria from 9.5 to 4.5 Ma (Schmincke, 1982). During this period (Unit III) sedimentation was dominantly pelagic with only occasional influx of volcanoclastic material. In the early part of this period the pelagic sediment was mostly nannofossil mixed sediment but changed to nannofossil ooze with time (Fig. 6).

A characteristic feature of the hiatus period was extensive sediment slumping. Similar slumps were recognized at Site 953 during the same interval, suggesting widespread instability, possibly related to the position of the site on the flanks of Gran Canaria. Initiation of this slumping may be related to volcano-tectonic activity on neighboring islands, such as Tenerife, or the instability of dominantly fine-grained sediment being deposited during the volcanic hiatus.

In the late Pliocene the influx of coarse volcanoclastic material over the period from 4.3 to 3.4 Ma (Fig. 5) increased sharply. This relatively short-lived pulse marks the transition from Unit III to Unit II and is coincident with the Roque Nublo phase of volcanism on Gran Canaria (4.4–3.4 Ma; Schmincke, 1994). During this time thick lapillistones were emplaced by debris flows and coarse sands were deposited by turbidity currents. However, the large clasts are angular and seem to be entirely of Miocene shield basalt composition with minor Miocene ignimbrite suggesting that mass wasting (flank collapse) may have supplied the clasts rather than volcanic activity.

The transition to Subunit Ic in the late Pliocene is marked by a decrease in the deposition of coarse volcanoclastic material (Fig. 5). During deposition of Subunit Ic, hemipelagic sedimentation continued to dominate but with a distinct change in the turbidite sand composition. Quartz sand in the bases of many of the turbidites in Subunit Ic indicates a source from the African continent. However, these quartz sands have various amounts of foraminifers and volcanic lithic grains indicating mixing of different source areas. Slumped intervals in this unit have slightly different interbed lithologies than the coherent strata above and below the disrupted sequences suggesting that the slumped intervals may have moved considerable distances.

At ~2 Ma Site 956 once again began receiving an influx of felsic volcanoclastic material. Much of this material was deposited as turbidity currents or grain flows and is typically very rich in pumice. Vitric-rich material was also deposited by fallout from explosive eruptions forming relatively thin ash layers. The abundance of pumice and vitric sand, lapilli, and ash reflects dominantly felsic volcanism, probably from the neighboring island of Tenerife. Tephra fall layers of similar age and mineralogy have also been found at Site 397, south of the island of Gran Canaria (Schmincke and von Rad, 1979). As in Subunit Ic, slumped intervals are common in Subunit Ib, indicating continued instability of these sediments.

During the upper part of the Pleistocene (Subunit Ia), hemipelagic sedimentation was punctuated by thick debris flows and turbidity flows of bioclastic sands containing abundant shallow marine fossils and minor phonolitic volcanoclastic material. The lack of quartz and presence of volcanic grains in these coarse debris flows suggest they were derived from either Tenerife, which was also volcanically active at this time, or Gran Canaria rather than the continental shelf. Their initiation may be related to sea-level changes caused by Pleistocene glacial–interglacial cycles.

In summary, the lithostratigraphy of Site 956 bears many similarities to that of Site 953. The supply of volcanoclastic material by sediment gravity flows and fallout from both Gran Canaria and Tenerife has played a fundamental role in determining the lithostratigraphy of Site 956. This supply has changed dramatically both in its rate and lithology from the late Miocene to the present and reflects the proximity of the site to the volcanically active Canary Islands. In contrast to Site 953, however, Site 956 also received an important contribution of organic and siliciclastic material from the African margin via turbidity currents, although to a much lesser degree than Site 955.

BIOSTRATIGRAPHY

Introduction

Site 956 recovered 703.50 m of mostly hemipelagic and fossiliferous sediments ranging in age from Quaternary to late early Miocene(?). The Pliocene, Pleistocene, and upper Miocene sections of lithologic Units I–III were extensively slumped. Within the slumped interval, possible repeated sections were identified in the Pliocene and possibly upper Miocene from nannofossil and foraminifer evidence (Tables 2 and 3). Below approximately 390 mbsf (Core 157-956B-24R), less slumping is present and the biostratigraphic record is less chaotic.

At least two hiatuses appear in the Miocene section where no pervasive slumping is apparent. The first is present between 399.07 and 413.30 mbsf and spans a minimum of 0.6 m.y. between 8.8 and 9.4 Ma. This hiatus was also present at Sites 954 and 955, suggesting it was a regional event. The second hiatus appears between 445.35 and 446.30 mbsf and according to nannofossil and foraminifer data spans a minimum of 0.8 m.y. between 9.99 and 10.8 Ma.

The Pliocene/Pleistocene boundary is placed between 60.10 and 63.17 mbsf based mainly on planktonic foraminifers, and the Miocene/Pliocene boundary is placed between 256.59 and 258.44 mbsf, based on both nannofossils and planktonic foraminifers (Fig. 20). These boundaries occur within slumped intervals and should be taken as an approximate guide only.

Microfossil preservation is generally good to moderate and it deteriorates to poor to moderate only in lithologic Unit IV and in the basaltic breccias of Unit V, where abundances were moderate to low.

Calcareous Nanofossils

Nannofossils are generally abundant with moderate to good preservation above approximately 555 mbsf. Below 568 mbsf preservation was poor (Table 2). The broad sample spacing at this site results from our avoiding sampling core sections that were obviously disturbed or slumped.

Pleistocene

The Pleistocene section was heavily disturbed by pervasive slumping, with many of the cores having chaotic bedding and wildly variable dips (see "Lithostratigraphy," this chapter). One thin possibly allochthonous interval of lower Pliocene Zone CN10 in Sample 157-956B-4H-6, 66 cm (33.26 mbsf), was slumped within the Pleis-

Table 2. Abundance, preservation, and lithology of samples used in nannofossil zonation, Holes 956A and 956B.

Core, section, interval (cm)	Depth (mbsf)	Abundance	Preservation	Zone	Lithology
157-956A-					
1H-CC, 12-12	6.06	H	G	CN15	Turbidite
2H-5, 77.5-77.5	12.88	H	G	CN14b/15	?Turbidite
3H-5, 58-58	22.18	H	G	CN14a	Hemipelagic marl
4H-6, 66-66	33.26	H	M	?CN10	Slumped marl
5H-CC	44.25	H	G	CN13a	Hemipelagic marl
6H-3, 127-127	48.37	H	G	CN13a	Debris flow matrix
6H-CC	50.43	H	G	CN13a	Disturbed
7H-5, 52-52	60.12	H	G	CN12d	Hemipelagic ooze
8H-4, 20-20	67.80	VH	M	CN12d	Slumped marl
9H-3, 26-26	75.86	H	M	CN12d	Hemipelagic marl
9H-CC	82.15	H	G	CN12c	Slumped marl
10H-2, 103-103	84.63	H	G	CN12b	Hemipelagic marl
10H-5, 91-91	89.01	H	G	CN12b	Slumped mixed sediment
10H-CC	91.10	H	G	CN12a	Hemipelagic marl
11H-4, 80-80	96.90	H	G	CN12b	Hemipelagic marl
11H-7, 40-40	101.00	H	G	CN12b	Hemipelagic marl
12H-5, 60-60	107.70	H	G	CN12a	Debris flow matrix
13H-4, 80-80	115.90	H	G	CN12b	Debris flow matrix
14H-4, 60-60	125.20	H	G	CN12b	Hemipelagic marl
15H-5, 60-60	136.20	H	G	CN12b	Hemipelagic marl
16H-2, 60-60	141.20	H	G	CN12a	Debris flow matrix
17H-2, 80-80	150.90	H	G	CN12/CN11	Hemipelagic marl
17H-5, 80-80	155.40	H	G	CN12/CN11	Debris flow matrix
18X-1, 100-100	159.10	H	G	CN12/CN11	Hemipelagic marl
157-956B-					
1R-2, 122-122	159.82	H	M	CN11b	Hemipelagic marl
2R-1, 82-82	167.42	H	P	CN11?a	Debris flow matrix
4R-CC, 10-10	176.20	H	M	CN11a	Hemipelagic marl
5R-5, 85-85	202.25	H	G	CN11a	Hemipelagic marl
6R-5, 15-15	211.25	H	G	CN11a	Hemipelagic marl
7R-4, 50-50	219.70	H	G	CN10	Hemipelagic marl
10R-CC	250.98	H	G	CN10	Hemipelagic marl
11R-3, 41-41	256.61	H	G	CN9b	Hemipelagic marl
11R-CC	258.43	H	G	CN9b	Hemipelagic marl
12R-4, 21-21	267.51	H	G	CN9b	Hemipelagic marl
13R-2, 101-101	274.91	H	M	CN9b	Hemipelagic marl
13R-3, 4.5-4.5	275.45	H	M	CN9b	Hemipelagic marl
14R-4, 60-60	287.10	H	M	CN9b	Debris flow matrix
15R-7, 9-9	300.79	H	M	CN9b	Hemipelagic marl
16R-6, 11-11	308.91	H	G	CN9b	Hemipelagic marl
17R-4, 47-47	315.77	H	M	CN9b	Hemipelagic marl
18R-1, 125-125	321.55	VH	G	CN9b	Hemipelagic marl
19R-3, 33-33	333.23	H	G	CN9b	Hemipelagic marl
20R-4, 75-75	344.75	M	M	CN9b	Debris flow matrix
21R-1, 60-60	349.80	M	G	CN9b	Hemipelagic marl
21R-4, 61-61	354.31	M	G	CN9b	Turbidite
22R-3, 70-70	362.60	H	G	CN9a	Debris flow matrix
23R-2, 120-120	371.10	M	G	CN9a	Hemipelagic marl
24R-3, 9-9	380.99	M	G	CN9a	Hemipelagic marl
25R-2, 79-79	389.69	M	G	CN9a	Hemipelagic marl
26R-2, 56.5-56.5	399.07	L	G	CN8b	Turbidite
27R-CC, 8.5-8.5	413.30	M	M	CN7	Hemipelagic marl
28R-CC, 12-12	419.52	M	M	CN7	Hemipelagic marl
29R-CC, 10-10	430.40	M	M	CN7	Turbidite
30R-1, 77-77	436.47	M	G	CN7	Hemipelagic marl
31R-1, 100-100	446.30	H	G	CN5b	Ignimbrite matrix
32R-2, 106-106	457.49	M	M	CN5b	Hemipelagic marl
32R-4, 14-14	459.57	H	M	CN5	Hemipelagic marl
33R-1, 15-15	464.75	H	M	CN5	Hemipelagic marl
34R-1, 101-101	475.31	M	G	CN5	Hemipelagic marl
35R-3, 120-120	488.00	H	M	CN5	Hemipelagic marl
36R-1, 60-60	494.20	M	M	CN5	Hemipelagic marl
37R-2, 55-55	505.35	M	M	CN5	Hemipelagic marl
38R-1, 90-90	513.80	M	M	CN4	Hemipelagic marl
39R-3, 60-60	525.68	M	M	CN4	Hemipelagic marl
40R-2, 60-60	534.40	M	M	CN4	Hemipelagic marl
41R-3, 25-25	545.02	L	M	CN4	Hemipelagic marl
42R-3, 12-12	554.47	L	M	CN4	Hemipelagic marl
43R-6, 8-8	568.68	M	P	CN4	Hemipelagic marl
44R-4, 44-44	575.52	L	P	CN4	Hemipelagic marl
45R-4, 45-45	589.34	M	P	CN4	Hemipelagic marl
48R-3, 48-48	610.48	L	P	CN4	Hemipelagic marl
48R-5, 44-44	613.84	M	P	CN4	Hemipelagic marl
49R-1, 39-39	615.09	M	P	CN4 or older	Clast in breccia
53R-1, 54-54	657.84	M	P	CN4 or older	Clast in breccia
54R-1, 73-73	667.63	L	P	CN4 or older	Clast in breccia
55R-1, 65-65	677.25	L	P	CN4 or older	Clast in breccia
56R-2, 94-94	688.44	L	P	CN4 or older	Clast in breccia
57R-1, 105-105	697.05	M	M	CN4 or older	Clast in breccia

Note: Key to abbreviations for abundance and preservation in the "Explanatory Notes" chapter (this volume).

Table 3. Abundance, preservation, and lithology of samples used in foraminifer zonation, Holes 956A and 956B.

Core, section, interval (cm)	Depth (mbsf)		Abundance	Preservation	Zone	Lithology
	Top	Bottom				
157-956A-						
1H-CC, 0-2	5.93	5.95	A	G	N22	Calcareous sand
2H-CC, 0-2	14.58	14.60	A	G	N23	Marl
3H-CC, 0-2	25.39	25.41	A	M	N22	Disturbed marl
4H-CC, 0-2	34.61	34.63	A	M	N22	Marl
5H-CC, 0-2	44.24	44.26	C	M	N22	Gray ooze
6H-CC, 0-2	50.42	50.44	A	M	N22	Disturbed ooze
7H-5, 51-53	60.10	60.12	A	G	N22	Ooze
7H-CC, 0-2	63.15	63.17	A	G	PL6	Ooze
8H-CC, 0-2	72.09	72.11	A	G	PL6	Disturbed ooze
9H-CC, 0-2	82.14	82.16	A	G	PL5	Ooze
10H-CC, 0-2	91.09	91.11	A	G	PL5	Marl
11H-CC, 0-2	101.34	101.36	A	G	PL4	Calcareous sand
12H-CC, 0-2	110.72	110.74	A	M	PL4	Debris flow
13H-CC, 0-2	120.19	120.21	A	G	PL5?	Debris flow
14H-CC, 0-2	129.65	129.67	A	M	PL5?	Debris flow
15H-CC, 0-2	138.59	138.61	A	G	PL4	Marl
16H-CC, 0-2	148.75	148.77	A	G	PL4	Marl
17H-CC, 0-2	157.59	157.61	C	M	PL2?	Turbidite mud
18X-1, 0-2	158.09	158.11	R	P	PL2?	Marl
18X-CC, 0-2	159.54	159.56	A	G	PL3	Marl
157-956B-						
1R-3, 117-119	161.26	161.28	A	G	PL2	Marl
4R-CC, 0-2	185.69	185.71	A	G	PL2	Marl
5R-CC, 0-2	203.76	203.78	F	P	PL2	Marl
6R-CC, 0-2	213.22	213.24	A	G	PL1	Marl
7R-CC, 0-2	220.69	220.71	A	G	PL1	Marl
10R-CC, 0-2	250.97	250.99	A	M	PL1	Marl
11R-3, 40-42	256.59	256.61	A	G	PL1	Marl above a slump
11R-CC, 0-2	258.42	258.44	A	G	M13	Slumped chalk
12R-CC, 0-2	269.46	269.48	A	G	M13	Debris flow
13R-CC, 0-2	275.85	275.87	A	M	M11	Disturbed ooze
14R-CC, 0-2	287.34	287.36	C	M	M11	Slumped beds
15R-7, 10-12	300.79	300.81	C	M	M12	Marl
16R-CC, 0-2	309.33	309.35	C	M	M11	Marl
17R-CC, 0-2	319.79	319.81	A	G	M12	Slumped beds
18R-CC, 0-2	329.96	329.98	C	M	M12	Slumped beds
19R-CC, 0-2	338.71	338.73	C	M	M12	Marl
20R-CC, 0-2	348.86	348.88	F	P	M11	Turbidite mud
21R-CC, 0-2	357.97	357.99	F	P	M11	Debris flow
22R-6, 0-2	367.38	367.40	A	M	M12	Debris flow
23R-6, 34-36	376.26	376.28	C	P	M12	Debris flow
24R-6, 78-80	386.18	386.20	C	P	M12	Debris flow
25R-4, 73-75	392.62	392.64	A	M	M11	Marl
26R-CC, 0-2	399.16	399.18	F	P	M11	Turbidite mud
27R-CC, 0-2	413.20	413.22	A	M	M11	Turbidite mud
28R-CC, 0-2	419.39	419.41	A	M	M11	Turbidite mud
29R-CC, 0-2	430.29	430.31	A	M	M11	Turbidite mud
30R-CC, 0-2	437.19	437.21	F	P	M11?	Marl

Notes: Key to abbreviations for abundance and preservation in the "Explanatory Notes" chapter, (this volume).

tocene section. Pleistocene Subzone CN13b may be absent on account of slumping.

Sample 157-956A-1H-CC, 12 cm (6.06 mbsf), contains *Emiliania huxleyi*, and belongs to Zone CN15. Sample 157-956A-2H-5, 77.5 cm (12.88 mbsf), was assigned to undifferentiated Zones CN14b-15, as the presence of low abundances of *E. huxleyi*, which marks the lower part of Zone CN15, could not be positively determined with the light microscope.

The highest occurrence of *Pseudoemiliania lacunosa*, in Sample 157-956A-3H-5, 58 cm (22.18 mbsf), indicated Subzone CN14a. Sample 157-956B-4H-6, 66 cm (33.26 mbsf), from an obviously slumped interval, contains *Amaurolithus tricorniculatus* and several discoaster species suggesting lower Pliocene Zone CN10. Sample 157-956A-5H-CC (44.25 mbsf) contains the highest occurrences of *Calcidiscus macintyreii* and *Helicosphaera sellii* without *Gephyrocapsa "caribbeanica,"* and so belongs to Subzone CN13a. Subzone CN13b was not seen.

Pliocene

Subzone CN12d is indicated in Sample 157-956A-7H-5, 52 cm (60.12 mbsf), by the highest occurrence of *Discoaster brouweri*. The highest occurrence of *D. pentaradiatus* in Sample 157-956A-9H-CC (82.15 mbsf) indicates Subzone CN12c. The highest occurrence of *D.*

surculus in Sample 157-956A-10H-2, 103 cm (84.63 mbsf), indicates Subzone CN12b. From Sample 157-956A-10H-CC (84.63 mbsf) to 157-956A-16H-2, 60 cm (141.2 mbsf), there seems to be repetition of Subzones CN12a and 12b (see Table 2). Foraminifer data in this interval also indicate repetition.

Samples 157-956A-17H-2, 80 cm (150.90 mbsf), 157-956A-17H-5, 80 cm (155.40 mbsf), and 157-956A-18X-1, 100 cm (159.10 mbsf), contain considerable reworked upper Miocene forms. *Reticulofenestra pseudoumbilicus* and *Sphenolithus* spp., the markers for Zone CN11, could be reworked from the Miocene, so this section is assigned to undifferentiated Zones CN11 and 12. Sample 157-956B-1R-2, 122 cm (159.82 mbsf), without reworked Miocene, contains *R. pseudoumbilicus*, *Sphenolithus* spp., and *Discoaster tamalis* and is placed in Subzone CN11b. Samples 157-956B-2R-1, 82 cm (167.42 mbsf), to 157-956B-6R-5, 15 cm (211.25 mbsf), contain *R. pseudoumbilicus* and *Sphenolithus* spp. without *D. tamalis* and are placed in Subzone CN11a. Sample 157-956B-7R-4, 50 cm (219.70 mbsf), contains the highest occurrence of *Amaurolithus* spp. thus indicating Zone CN10.

Miocene

The highest consistent occurrence of *Discoaster quinquerramus* in Sample 157-956B-11R-3, 41 cm (256.61 mbsf), indicates upper Mi-

miopelagicus, a marker within the upper part of Subzone CN5b, indicating that Zone CN6 is absent and perhaps also the upper part of Subzone CN5b. Closer sampling is needed to verify this hiatus. If present, this hiatus has a minimum duration of 0.4 Ma, as the FO datum of *D. hamatus* is at about 10.4 Ma and the LO of *C. miopelagicus* is at about 10.8 Ma. A hiatus is also suggested by the foraminifer data.

Samples 157-31R-1, 100 cm (446.30 mbsf), and 157-956B-32R-2, 106 cm (457.49 mbsf), are assigned to Subzone CN5b because *Cyclicargolithus floridanus* is absent. Below the highest occurrence of *C. floridanus* in Sample 157-956B-32R-4, 14 cm (459.57 mbsf), the samples are assigned to undifferentiated Zone CN5. The highest occurrence of *Sphenolithus heteromorphus* in Sample 157-956B-38R-1, 90 cm (513.80 mbsf), indicates the top of Zone CN4. All samples below Sample 157-956B-48R-5, 44 cm (613.84 mbsf), were taken from calcareous clasts in the basaltic breccias of lithologic Unit V. All of these samples contain *S. heteromorphus* and were assigned to Zone CN4, or they are possibly as old as Zone CN3 based on the range of *S. heteromorphus*.

Planktonic Foraminifers

Zones from N23 to M7 and no older than M3 appear in general stratigraphic order at Site 956. However, the sequence above 430 mbsf is extensively disrupted by slumps and debris flows, which cause thickened and repeated sequences in the upper Pliocene and upper Miocene sequences (Fig. 20). A hiatus between the late and middle Miocene is indicated by the absence of Zones M9 and M10.

Planktonic foraminifers are generally abundant to common in the upper 500 m of the sequence and few to rare at greater depths (Table 3). Preservation is generally good to moderate above 340 mbsf and moderate to poor at greater depths. Low abundance and poor preservation combine to make zonal assignments difficult below 510 mbsf.

Pleistocene

The Pleistocene sequence is divided into Zones N23 and N22. The sequence contains many slumps and debris flows and the biostratigraphy should be regarded with caution (Fig. 20 and Table 3). Sample 157-956A-2H-CC, 0–2 cm (14.59 mbsf), is assigned to Zone N23. The overlying sample, 157-956A-1H-CC, 0–2 cm, contains an assemblage characteristic of Zone N22, but it comes from the calcareous basal sand of a turbidite and is evidently reworked from the older zone. Samples 157-956A-3H-CC, 0–2 cm, to 157-956A-7H-5, 51–53 cm (25.39–60.10 mbsf), are assigned to Zone N22. The sequence seems to be relatively thin and part of Zone N22 is probably missing. The lower part of the sequence includes at least some of the lower Pleistocene, which is characterized by low frequencies of *Globorotalia truncatulinoides* and the common occurrence of *Sphaeroidinella dehiscens*. The Zone N22/PL6 boundary is placed between Samples 157-956A-7H-5, 51–53 cm (60.11 mbsf), and 157-956A-7H-CC, 0–2 cm (63.16 mbsf), based on the first appearance of *Globorotalia truncatulinoides*.

Pliocene

The Pliocene sequence contains representative intervals of Zones PL6 to PL1 in general stratigraphic order, but extensive slumping and debris flows have repeated some intervals. Two samples, 157-956A-7H-CC, 0–2 cm (63.15 mbsf), and 157-956A-8H-CC, 0–2 cm (72.10 mbsf), are assigned to Zone PL6, which lies between the lowest stratigraphic occurrence of *Globorotalia truncatulinoides* and the highest stratigraphic occurrence of *Globorotalia miocenica*. The two samples contain *Globorotalia inflata* and the upper sample contains *Pulleniatina*, both of which reenter the Atlantic Ocean during the latter part of the zone. No sample contains the lower part of the zone.

Samples 157-956A-9H-CC, 0–2 cm (82.15 mbsf), and 157-956A-10H-CC, 0–2 cm (91.10 mbsf), are assigned to Zone PL5, which lies

between the highest stratigraphic occurrences of *Globorotalia miocenica* and *Dentoglobigerina altispira* with *Globorotalia multicamerata*. The interval includes the highest stratigraphic occurrence of *Globorotalia puncticulata* in the lower sample, hence both the upper and lower parts of the zone are represented.

The sequence between Samples 157-956A-11H-CC, 0–2 cm (101.35 mbsf), and 157-956B-1R-3, 117–119 cm (161.27 mbsf), is irregular in several respects. Samples from 157-956A-11H-CC, 0–2 cm (101.35 mbsf), to 157-956A-16H-CC, 0–2 cm (148.76 mbsf), are tentatively assigned to Zone PL4. This zone is typically short because it spans only 0.06 m.y., but at Site 956 it is longer, extending nearly 50 m. The interval is heavily slumped, which may have thickened the sequence. The internal character of the zone is also atypical. *Dentoglobigerina altispira* and *Globorotalia multicamerata* are rare and sporadic in their occurrences. In fact, two samples in the middle of the interval, 157-956A-13H-CC, 0–2 cm (120.20 mbsf), and 157-956A-14H-CC, 0–2 cm (129.66 mbsf), have neither species and can be assigned to lower Zone PL5. The interval may be a repeated section.

The subjacent Samples 157-956A-17H-CC, 0–2 cm (157.60 mbsf), and 157-956A-18X-1, 0–2 cm (158.10 mbsf), are assigned to Zone PL2 based on the presence of *Globorotalia margaritae*, although the sample is odd because it contains no *Sphaeroidinellopsis seminulina*. This interval is out of stratigraphic order. The sequence resumes a more normal stratigraphic succession in the underlying Sample 157-956A-18X-CC, 0–2 cm (159.55 mbsf), which is tentatively assigned to Zone PL3 based on the highest stratigraphic occurrence of *Sphaeroidinellopsis seminulina*. The sample, however, contains a few specimens of *Globigerina nepenthes*, which may be reworked.

The lower Pliocene is more normal in its succession. The interval, however, is still extensively disrupted by slumps and debris flows, so caution is needed when applying the biostratigraphic data. Two samples (157-956A-1R-3, 117–119 cm, to 157-956A-5R-CC, 0–2 cm; 161.27–203.76 mbsf) belong to Zone PL2, which contains common *Globorotalia margaritae*, and four samples (157-956A-6R-CC, 0–2 cm, to 157-956A-11R-3, 40–42 cm; 213.23–256.60 mbsf) belong to Zone PL1, which contains *Globigerina nepenthes*. The Zone PL1/M13 boundary lies between Samples 157-956A-11R-3, 40–42 cm (256.60 mbsf), and 157-956A-11R-CC, 0–2 cm (258.43 mbsf), based on the highest stratigraphic occurrence of *Globorotalia juanai*, which approximates the boundary.

Miocene

The upper Miocene sequence also contains slumped intervals and is interrupted by one possible disconformity. Two samples, 157-956B-11R-CC, 0–2 cm (258.43 mbsf), and 157-956B-12R-CC, 0–2 cm (269.46 mbsf), bear *Globorotalia margaritae*, *Globorotalia juanai*, and dextral coiling *Neogloboquadrina acostaensis* and can be assigned to Zone M13. The sequence from Samples 157-956B-13R-CC, 0–2 cm (275.86 mbsf), to 157-956B-24R-6, 78–80 cm (386.19 mbsf), consists of slumped beds, debris flows, and turbidite muds. Several samples within the chaotic interval contain *Globorotalia conomiozea* without *Globorotalia margaritae* and can be assigned to Zone M12, and several intervening samples (Table 3) bear *Neogloboquadrina acostaensis* without *Globorotalia conomiozea* and belong to Zone M11. The sporadic occurrences of *Globorotalia conomiozea* can be explained in two ways. The species may have been environmentally excluded from the region at several times during deposition of the interval. Alternatively, the intervals may be repeated because of slumping. The interval is tentatively placed in undifferentiated Zones M11/M12.

Slumping probably does not affect the interval between Samples 157-956B-25R-4, 73–75 cm (392.62 mbsf), and 157-956B-31R-1, 9–17 cm (445.36 mbsf). The samples, taken from marl and turbidite mud, contain sinistral and dextral *Neogloboquadrina acostaensis*, sinistral menardine globorotalids, and *Globigerina nepenthes* with-

out *Globorotalia conomiozea* and belong to Zone M11. A probable disconformity is present between 445.35 and 458.75 mbsf because we did not find any material assignable to Zone M10/M9. The hiatus represents at least 0.81 m.y. and is bracketed by the FO of *Globigerina nepenthes* and *Neogloboquadrina acostaensis*.

The subjacent samples (157-956B-32R-3, 81–83 cm, to 157-956B-37R-2, 108–110 cm; 458.74–505.88 mbsf) are placed in Zone M8 based on the occurrence of rare *Globorotalia peripheroacuta* and *Globorotalia fohsi* without *Globorotalia peripheroronda*. Preservation and abundance deteriorate markedly below 505.88 mbsf making zonal assignments difficult. Samples 157-956B-38R-1, 91–93 cm (513.81 mbsf), to 157-956B-42R-1, 11–13 cm (551.61 mbsf), are placed in undifferentiated Zones M7/M8. The better preserved samples contain frequent *Globorotalia peripheroacuta*, and several samples also contain *Sphaeroidinellopsis disjuncta*, *Sphaeroidinellopsis seminulina*, *Globigerinoides trilobus*, *Globoquadrina dehiscens*, and specimens close to *Globorotalia peripheroronda*. Samples 157-956B-43R-1, 50–52 cm, and 157-965B-45R-4, 44–45 cm contain rare *Sphaeroidinellopsis disjuncta*, *Sphaeroidinellopsis seminulina*, *Globoquadrina dehiscens*, and *Paragloborotalia mayeri* and can be no older than Zone M3 based on the range of *Sphaeroidinellopsis* spp. Samples 157-956B-53R-1, 52–53 cm (657.83 mbsf), and 157-956B-53R-3, 38–39 cm (660.69 mbsf), from the matrix of a lapillistone include *Globorotalia archeomenardii*, *Globigerinoides diminuta*, *Globorotalia peripheroronda*, *Globorotalia peripheroacuta*, and *Sphaeroidinellopsis seminulina* and can be assigned to Zone M7.

PALEOMAGNETISM

Introduction

Paleomagnetic measurements were made on the APC and the RCB cores recovered from Holes 956A and 956B. All the APC and the RCB cores (except the RCB cores that recovered only small fragments in debris flows) were measured in the long-core mode of the 2G-Enterprises magnetometer. They were demagnetized to at least 25 mT and analyzed for magnetostratigraphy. The results from both the APC and RCB cores showed once again a strong downward overprint, so that even after demagnetization much of the inclination was anomalously high. The detailed magnetostratigraphy must await onshore measurements of discrete samples.

Experiments were continued to clarify the origin of the magnetization overprint acquired during drilling. To this end, the fields associated with drill bit and collar assemblies were measured with a Hall-probe magnetometer. These will be described in the Leg 157 *Scientific Results* volume.

Intensity of NRM (25 mT) and low field susceptibility are plotted in Figure 21. Both values are again a good proxy for volcanic input.

Magnetostratigraphy

Hole 956A

Plots of the inclination from all cores are shown in Figure 22, which also shows the inclination data after the disturbed, slumped, and debris flow material has been removed. The recovered cores from Hole 956A include long intervals of slumped formations (see "Lithostratigraphy," this chapter). The directional and intensity behavior in the slumped intervals is problematical, as noted in the "Paleomagnetism" section of the "Site 955" chapter (this volume).

Given the poor paleomagnetic record obtained, it does not seem appropriate to give detailed chron boundaries. However, the first reversed interval close to 34 mbsf most likely represents the onset of the Brunhes (C1n). Other reversed intervals centered at 60 and 75 mbsf possibly represent the reversed period between C2n/C2An.

Hole 956B

In this hole, the massive slumps continued. Although there are intervals between 300 and 400 mbsf in which consistent magnetizations are seen with appropriate inclinations, they are too short to build up a reliable magnetostratigraphy. It is not until the interval between 450 and 550 mbsf that the record is sufficiently continuous to permit any plausible magnetostratigraphic interpretation. Even here, the record is not very convincing, and we await shore-based magnetostratigraphic studies. We will also study the effect on magnetization of soft sediment deformation involved in the slumping.

Conclusions

The magnetostratigraphy of the sediments from Holes 956A and 956B has been impossible to establish below the Brunhes/Matuyama boundary.

Preliminary observations of the fields associated with drill bits and collars suggests that the remanent magnetization of the drilling collar gives rise to a field in which the drilling takes place. These observations should be extended with more shipboard investigation. Any mitigation of the effect seems to involve reducing the magnetization of the drill assembly.

PETROGRAPHY, MINERALOGY, AND GEOCHEMISTRY OF VOLCANICLASTIC SEDIMENTS

A wide variety of volcanoclastic sediments were recovered at Site 956, including fine-grained ash fall, crystal-lithic silt and sand, pumiceous sand, basaltic lapillistone, and hyaloclastite tuff and lapillistone (Table 4). As in Sites 953, 954, and 955, petrographic analysis shows that the majority of the volcanoclastic material is derived from Gran Canaria. However, Site 956 differs from the previous sites in having a much greater abundance of pumice sand and ash derived from Pleistocene eruptions of Pico de Teide Volcano on the island of Tenerife.

Petrography and Mineralogy

Subunit Ia (0–37.5 mbsf) contains numerous beds of bioclastic sands and one pumiceous lapilli bed. Bioclastic sands contain mainly biogenic fragments with very minor volcanic material (up to 10%–20%). The dominant lithic component of the sands is trachyphonolite lava together with minor basalt (plagioclase-phyric tachylite and crystalline basalt). Felsic pumice is also common in the bioclastic sands. A pumiceous lapilli bed in Core 157-956A-3H contains pumice with variable amounts of alkali feldspar and amphibole phenocrysts (Fig. 23). Crystals in the sands are mainly alkali feldspar with minor clinopyroxene (Ti-augite), alkali amphibole, and biotite. The main source of volcanoclastic lithics, pumice, and crystals is likely to be Tenerife, which was volcanically very active in the Pleistocene.

Subunit Ib (37.5–76.5 mbsf) contains numerous thin interbeds of sand and silt with pumice, pumice sand, basaltic gravel, vitric silt, and crystal-lithic sand. Dominant lithic components are basalt (plagioclase-phyric tachylite) and trachyphonolite lava. Felsic pumice is also very abundant and is the main component of the pumice sands (interval 157-956A-8H-6, 12–14 cm). A basaltic gravel occurs in Core 157-956A-6H-1 and contains a large proportion (~50%) of plagioclase-clinopyroxene-phyric basalt. The crystal components in the volcanoclastic sediments are mainly alkali feldspar, clinopyroxene (Ti-augite), and minor alkali amphibole and biotite. Vitric ash layers in Subunit Ib contain felsic glass shards with minor pumice and rare alkali amphibole. The mineralogy and age of these deposits suggests that they are derived from explosive eruptions of Teide Volcano

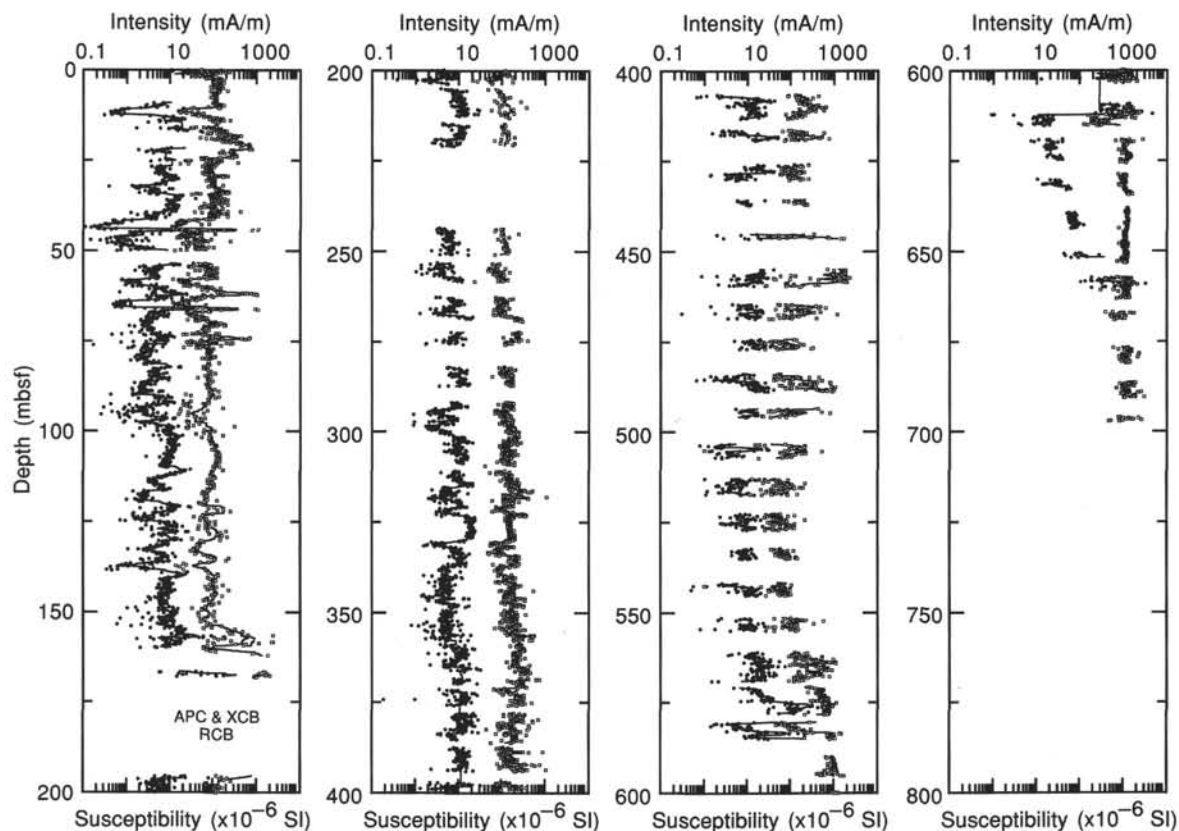


Figure 21. 25 mT NRM intensity (filled circles) and low field susceptibility (open squares) for Holes 954A and 954B. Lines connecting data points indicate smoothed susceptibility ($n = 20$) and smoothed intensity ($n = 7$).

(Tenerife). The main sources of volcanic rock fragments and crystals for Subunit Ib are similar to those of Subunit Ia.

Subunit Ic (76.5–158 mbsf) contains minor volcanoclastic interbeds in Cores 157-956A-12H and 157-956A-13H. Crystal lithic sands contain small amounts of basaltic clasts and crystals are mainly clinopyroxene (Ti-augite) with rare plagioclase.

Unit II (158–196.9 mbsf) contains quartz silts and sands, and a basaltic lapillistone. The silts and sands are distinguished from those in Subunit Ic by an increased abundance of basaltic lithics. Crystal-lithic sands contain mainly basaltic rock fragments (crystalline and tachylitic basalt and minor sideromelane). Crystals are mainly clinopyroxene (Ti-augite) with very minor plagioclase and alkalic amphibole. The lapillistone contains mostly aphyric, angular, crystalline basaltic fragments, (Fig. 24) and very minor sideromelane, which were probably derived from the Miocene shield basalts of Gran Canaria. Volcanoclastic sediments of Unit II typically have a zeolitic cement. An isolated clast of trachyphonolitic welded tuff occurs in Core 157-956B-3R-1.

Unit III (196.9–367.5 mbsf) contains thin interbeds of crystal-lithic silt and sand with minor lapillistone. Dark volcanic fragments are sometimes dispersed within the clayey nanofossil mixed sediments. An isolated clast of welded tuff occurs within a slumped interval in Core 157-965B-5R-1. The tuff is characterized by eutaxitic texture and a welded glassy matrix (Fig. 25). Fiamme show vapor phase crystallization. Crystals are mainly alkali feldspar with minor alkali amphibole and biotite. Phonolite lava clasts are present. The welded tuff clast was probably derived from a subaerial ignimbrite of the Fataga Group on Gran Canaria.

Subunit IVa (367.5–517.5 mbsf) contains vitric tuffs with variable crystal and lithic contents, crystal-lithic sandstone, and basaltic breccia. The tuffs are typically poorly sorted and composed of colorless felsic glass shards and small pumice fragments (Fig. 26). Many contain abundant crystalline and tachylitic basalt clasts. Large crys-

tals of alkali feldspar and pale green clinopyroxene are the most abundant crystals together with minor amphibole. Very minor amounts of sideromelane are present in some tuffs. The crystal-lithic sandstones are also poorly sorted and are composed dominantly of subangular to subrounded basalt clasts, mostly crystalline, and crystals of clinopyroxene (Ti-augite), alkali feldspar, plagioclase, and traces of alkali amphibole and vesicular sideromelane shards.

Subunit IVb (522.6–564.1 mbsf) contains numerous vitric tuffs. Felsic glass shards are the main component together with minor alkali feldspar and amphibole. The abundance of colorless glass shards, probably of rhyolitic composition, suggests that these tuffs are related to the middle Miocene Mogan Group volcanics on Gran Canaria.

Unit V (564.1–704 mbsf) is characterized mainly by basaltic hyaloclastite tuffs, lapillistones, and breccias. They are composed of pervasively altered sideromelane shards that range from nonvesicular to highly vesicular, and basaltic lithic clasts that include both aphyric and porphyritic varieties. Some clasts contain abundant large clinopyroxene phenocrysts and olivine pseudomorphs. Plagioclase-aphyric varieties are also present. The presence of basaltic material from both shallow submarine and subaerial eruptions indicate that these sediments are derived from the emergent shield stage of Gran Canaria. Also occurring near the top of Unit V is parallel and cross laminated foraminiferal-crystal sandstone that contains abundant prismatic black amphibole crystals, and lesser amounts of green pyroxene, zircon, chlorite, and sphene. The morphology of these crystals suggests a volcanic origin but a metamorphic or plutonic source outside the Canary Islands is more likely, such as the African continental margin.

Geochemistry

A clast of welded tuff from the top of Unit III was analyzed for major and trace elements (Table 5). The tuff is a moderately silica-

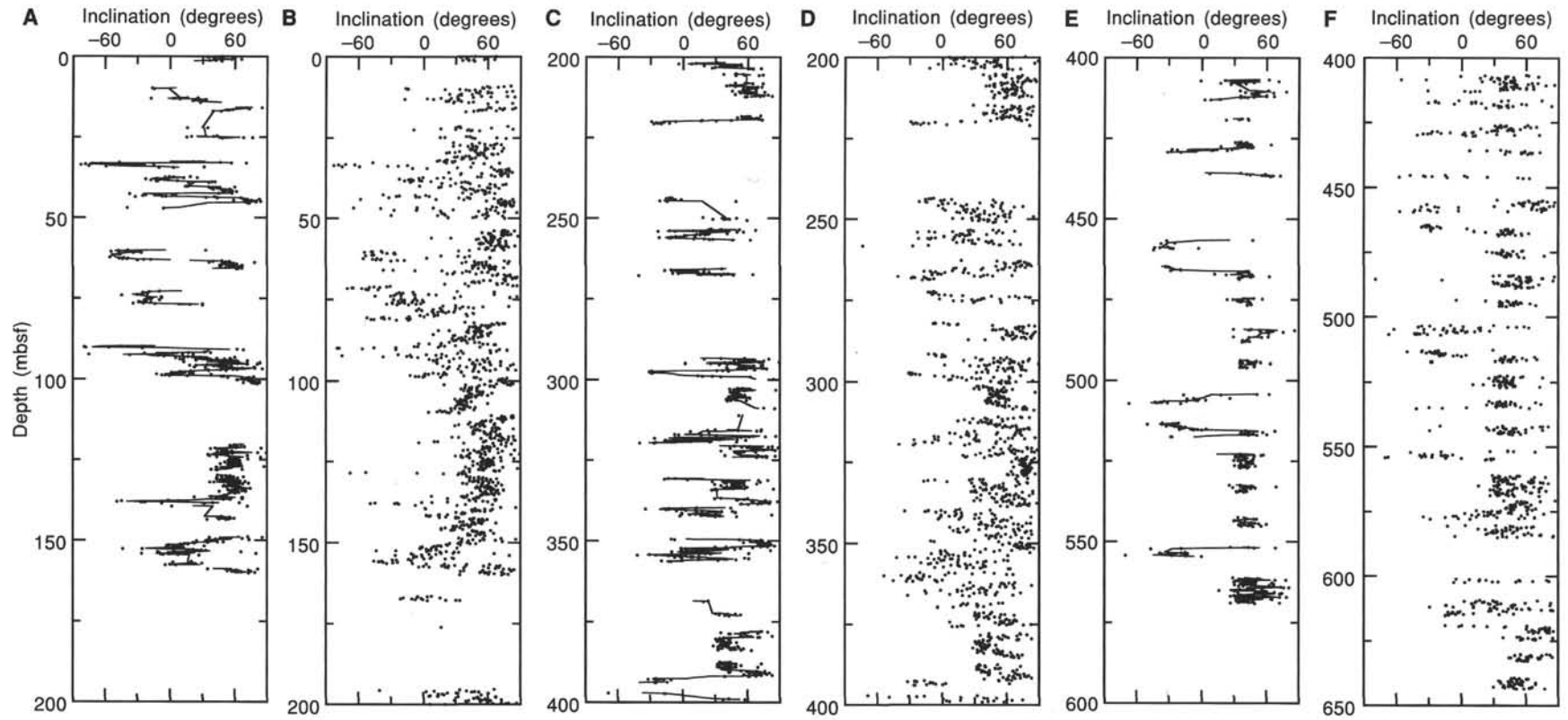


Figure 22. Magnetic data from APC and RCB cores from Site 956. **A**, **C**, and **E**. Inclination data with disturbed, slumped, and volcanic intervals removed; connecting lines indicate smoothed inclination ($n = 3$). **B**, **D**, and **F**. Inclination data from all cores.

undersaturated trachyphonolite typical of the Fataga Group on Gran Canaria (Schmincke, 1994). It is a relatively evolved rock with intermediate SiO₂, low MgO, and high incompatible element abundances. The Zr/Nb ratio of 4.1 is also typical of Fataga Group volcanics. Its bulk composition is similar to those of crystal-lithic sands and tuffs of comparable age recovered at Site 953 (see "Site 953," this volume).

INORGANIC GEOCHEMISTRY

Introduction and Operation

A total of 24 interstitial-water samples were taken between 1.45 and 542.51 mbsf at Site 956 (Table 6). The sampling strategy and analytical methods were identical to those employed at Sites 950–955 (see "Explanatory Notes," this volume). Due to lack of time, samples were analyzed only for pH, salinity, chlorinity, and alkalinity aboard ship. Sulfate, silica, magnesium, and calcium were determined onshore by inductively coupled plasma–atomic emission spectrometry, and sodium and potassium by atomic absorption spectrometry, at the Laboratoire de Géochimie ORSTOM Bondy (France). Changes in pore-water composition are driven by the bacterially mediated oxidation of organic matter from organic-rich sediments and diagenetic reactions in the siliclastic fraction, particularly the appearance of smectites and zeolites forming at the expense of volcanic glass. In contrast to Site 955, no brines were observed in the sequence.

Sulfate and Alkalinity

Sulfate (Fig. 27) contents decreased from around 38 mmol/L in the upper 25 m, to 10 mmol/L at 200–250 mbsf. Values at the top of the section appear to be enriched compared to typical seawater values (28.9 mmol/L). Sulfate contents rise again below 250 mbsf, approaching seawater concentrations in volcaniclastic-rich Unit IV. The high values recorded in the upper 50 m, and increased sulfate at depth, might be attributable to the dissolution of sulfur-rich glasses. The strong gradient indicates moderate sulfate reduction rates in the upper 200 m.

Alkalinity increases from 3.6 mmol/L at 2 mbsf (significantly higher than the 2.3 mmol/L seawater value), to a maximum of 4.5–4.9 mmol/L between 25 and 70 mbsf (Fig. 27), below which concentrations decline exponentially, falling to <0.5 mmol/L below 500 mbsf. High alkalinity in the upper beds may be attributed to H₂S and HCO₃⁻ production accompanying sulfate reduction. The alkalinity profile is similar to that seen at Site 955 but is offset toward lower concentrations, indicating reduced rates of sulfate reduction at Site 956.

Chloride, Salinity, and Sodium

Salinity (Fig. 28) decreases from close to seawater values (35 g/kg) in the upper 80 m to a minimum of 32 g/kg around 200–250 mbsf, and then climbs steadily to a maximum of 36 g/kg around 540 mbsf. Chloride (Fig. 28) shows a regular increase with depth, from seawater concentrations in the uppermost 25 m, to a maximum of 590 mmol/L at 540 mbsf. The high salinities and chlorinities observed at Site 955 do not occur at Site 956.

Sodium and Potassium

Sodium remains close to seawater values throughout the section (Fig. 29) but shows a similar trend to chlorinity with slightly higher concentrations in the deeper samples. Potassium is slightly enriched over seawater values in the uppermost 50 m, with values around 11 mmol/L (Fig. 30). Concentrations decline to a minimum of <4 mmol/L in the lower beds of Unit III, before rising again to 9 mmol/L in the

deepest sample. The presence of a potassium minimum between 250 and 350 mbsf indicates uptake of potassium by a diagenetic phase, probably phillipsite, forming at the expense of volcanic glasses. Potassium is then being liberated at depth by further alteration of the volcaniclastic fraction.

Silica

The pore-water silica profile is rather similar to that of Site 955 but attains slightly lower concentrations in the upper beds. Silica fluctuates around 550 μmol/L in the upper 130 m with a maximum of 650 μmol/L at 42 mbsf (Fig. 29). Concentrations decline markedly below 130 mbsf, falling to 128 μmol/L around 250 mbsf, and then fluctuating between 100 and 180 μmol/L down to 410 mbsf. Increasing values below 410 mbsf, which coincide with rising potassium, are associated with the occurrence of evolved volcanic glasses in Unit IV.

Magnesium and Calcium

Calcium is variable, falling from seawater values (Fig. 31) at 2 mbsf to low concentrations of around 8.7 mmol/L between 25 and 80 mbsf, and attaining a minimum of 7.8 mmol/L at 90 mbsf. Below this, concentrations increase progressively, reaching a maximum of 33 mmol/L in the bottom sample. The Ca²⁺ minimum lies immediately below the alkalinity maximum indicating that carbonate precipitation is consuming bicarbonate. High calcium concentrations in pore waters at the base of the sequence are probably a consequence of the dissolution of volcanic glasses.

Magnesium contents increase from less than seawater values of 52.6 mmol/L at 2 mbsf (Fig. 31), to a maximum of 55 mmol/L around 35 mbsf. Below this, Mg²⁺ decreases sharply to a minimum of 24.7 mmol/L at 201 mbsf. Between 320 and 370 mbsf, Mg²⁺ values increase to around 30 mmol/L, but decline again to 21 mmol/L below 500 mbsf. The Mg/Ca ratio (Fig. 31) peaks at around 60 mbsf, falls sharply to a plateau between 200 and 350 mbsf, before dropping off again below. The upper Mg²⁺ minimum and the plateau in the Mg/Ca ratio coincide with the sulfate minimum, offering the probability that precipitation of dolomite under sulfate reducing conditions is acting as a sink for magnesium. Lower pore-water Mg²⁺ and increasing calcium concentrations at the base of the site probably result largely from diagenetic reactions within the siliclastic fraction.

ORGANIC GEOCHEMISTRY

The shipboard organic geochemistry program at Site 956 followed the same procedures used at previous sites.

Volatile Hydrocarbons

Concentrations of methane (C₁) and ethane (C₂) gases were monitored in every core by the standard ODP headspace-sampling technique as part of the SSP program. Methane contents remained constantly low throughout the entire sequence at Site 956, varying between 2 and 4 ppmv. No ethane was detected.

Carbon, Nitrogen, and Sulfur Concentrations

A total of 84 analyses of carbonate were made, and related to lithology as for Sites 950–955. Samples were then selected for the determination of organic carbon, nitrogen, and sulfur. A total of 26 samples were run on the CNS instrument.

Organic carbon contents varied from below detection to 1.18% (Fig. 32 and Table 7) with several values above 0.4% occurring in the upper 60 mbsf. Nitrogen varied between 0.01% and 0.14%, and sul-

Table 4. Summary of volcanoclastic components, Site 956.

Unit	Subunit	Core (top)	Depth (mbsf)	Age (Ma)	Period	Lithologies with volcanic components
I	a	1H	0.0	0.0	Post-Roque Nublo and Tenerife	Bioclastic sand with minor volcanics, pumice sand
	b	5H-4	38	1.3	Post-Roque Nublo and Tenerife	Pumice sand, basaltic gravel, vitric silt, and crystal-lithic sand
	c	9H-4	77	2.3	Post-Roque Nublo	Minor crystal-lithic sand
II		18X-1	158	3.2	Roque Nublo	Basaltic lapillistone and crystal-lithic sand
III		5R	195	4.0	Volcanic hiatus	Thin interbeds of crystal-lithic silt and sand, minor lapillistone
IV	a	25R-4	392	8.2	Fataga	Vitric tuff, lithic-vitric tuff, crystal-lithic sandstone, and basaltic breccia
	a	34R-1	474	12.2	Mogan	Vitric tuff
V		43R-3	564	14.0	Shield stage	Basaltic lapillistone and hyaloclastite tuffs

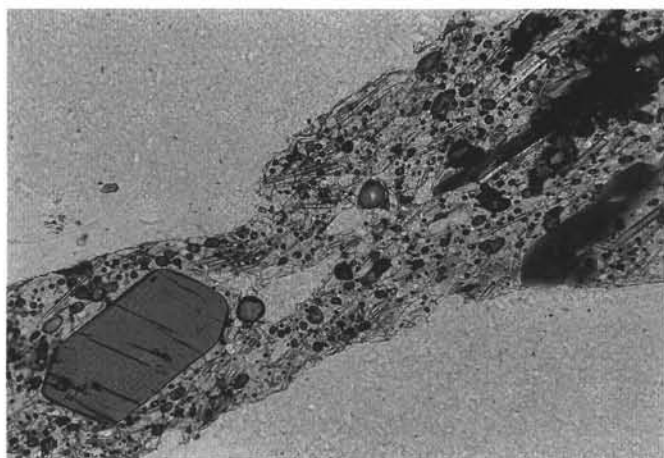


Figure 23. Photomicrograph of a pumice sand with crystals and lithics from Subunit Ia showing crystal-rich pumice. Field of view is 2.0 mm wide. Sample 157-956-3H-3, 93–94 cm.



Figure 25. Photomicrograph of a welded tuff clast from Unit III showing welded glass shards, lithics, and crystals of alkali feldspar. Field of view is 8.0 mm wide. Sample 157-956-5R-1, 47–51 cm.

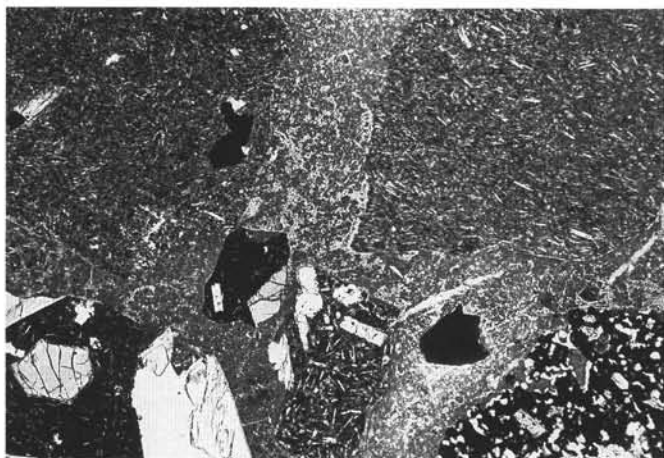


Figure 24. Photomicrograph of a basaltic lapillistone from Unit II that contains abundant angular to subrounded clasts of crystalline and tachylitic basalt. Field of view is 8.0 mm wide. Sample 157-956-2R-1, 128–131 cm.

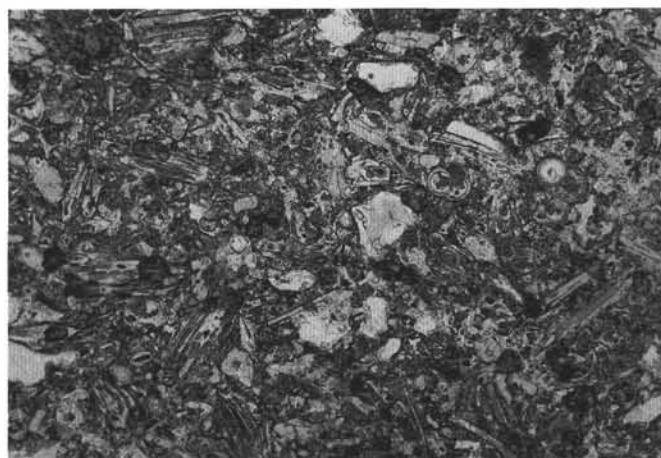


Figure 26. Photomicrograph of a vitric tuff from Subunit IVa showing abundant glass shards with pipe-vesicle structure. Field of view is 2.0 mm wide. Sample 157-956-33R-3, 103–105 cm.

Table 4 (continued).

Unit	Volcanic components		
	Rock fragments	Crystals	Vitric clasts
I	Minor trachyphonolite and basalt	Alkaline feldspar > clinopyroxene (Ti-augite), alkaline amphibole, and biotite	Phonolite pumice
	Basalt (tachylite and plagioclase/clinopyroxene), trachyphonolite lava	Alkaline feldspar, clinopyroxene (Ti-augite) > alkaline amphibole, and biotite	Phonolite pumice, minor vesicular sideromelane
	Minor basaltic clasts	Ti-augite >> plagioclase	
II	Basalt (tachylite and Ti-augite-phyric)	Ti-augite >> plagioclase, alkaline amphibole	Minor sideromelane
III	Trachyphonolite lava and welded tuff	Alkaline feldspar > alkaline amphibole, biotite	Minor felsic glass shards
IV	Basalt	Alkaline feldspar, clinopyroxene >> amphibole, plagioclase	Felsic glass shards and pumice
		Alkaline feldspar	Felsic glass shards and pumice, minor sideromelane
V	Basalt (olivine, clinopyroxene, minor plagioclase, and opaques)	Clinopyroxene and olivine pseudomorphs	Altered sideromelane shards

Table 5. XRF major and trace element analysis of welded ignimbrite clast from, Site 956.

Hole, core, section:	956B-5R-1
Interval (cm):	47-51
Depth (mbsf):	195.87
Major elements (wt%)	
SiO ₂	61.97
TiO ₂	0.92
Al ₂ O ₃	17.32
Fe ₂ O ₃	5.37
MnO	0.26
MgO	1.52
CuO	0.67
Na ₂ O	6.59
K ₂ O	5.73
P ₂ O ₅	0.06
Total	100.41
LOI	3.38
Trace elements (ppm)	
Cr	1.1
Ni	7.8
Cu	1.5
V	26.3
Zn	223
Sr	172.2
Ba	402.8
Rb	125.1
Y	73.5
Zr	1266
Nb	305.5
Ce	484.3
Zr/Nb	4.1

fur concentrations ranged from below detection to 0.4%, both generally following the organic carbon trend.

C/N ratios ranged from 1 to 10, except for one value of 16 at 211 mbsf. These ratios indicate a primarily marine source for the organic carbon at Site 956, although low organic carbon values and the presence of abundant clay minerals may have resulted in reduced C/N values.

PHYSICAL PROPERTIES

Introduction

Measured physical properties included nondestructive GRAPE bulk density, magnetic susceptibility, natural gamma ray, and *P*-wave velocity from whole-round core sections using the MST, as

well as thermal conductivity following the full-needle probe method. Shear strength, *P*-wave velocity, and index properties were measured from split sections on discrete samples (see "Explanatory Notes" chapter, this volume). Although core recovery in Hole 956B was moderate, missing intervals affected the continuity of the physical properties measurements. In general, physical properties variations at Site 956 define intervals that agree closely with the lithostratigraphic units (see "Lithostratigraphy," this chapter) or that indicate compositional changes within the sediment.

Whole-core Measurements

MST

Whole-round measurements of GRAPE density and magnetic susceptibility were made on all cores throughout Holes 956A and 956B and the natural gamma ray was measured up to Core 157-956B-45R (584 mbsf). *P*-wave velocity was measured only in Hole 956A because of void spaces between sediment core and the plastic liner. Cores from Hole 956A were allowed to thermally equilibrate for ~4 hr to room temperature before MST logging; cores from Holes 956B were measured immediately. Sampling rate was typically one measurement every 1.5 to 2 cm for the *P*-wave logger, 2.5 cm for the GRAPE, 3 cm for magnetic susceptibility, and 30 cm for natural gamma activity. For details on the MST sensors see the "Explanatory Notes" chapter of the Leg 156 *Initial Reports*. Data obtained from all four sensors are shown on Figures 33 through 41. The data were filtered with a running median filter to eliminate spikes. The filter length in Hole 956A was 0.125 m for the velocity, density, and magnetic susceptibility, and 1 m for the natural gamma ray. In Hole 956B, the filter length was doubled. Intervals longer than the filter length without data are indicated by gaps in the curves.

Magnetic Susceptibility

Volumetric magnetic susceptibility was measured in all recovered cores from Holes 956A and 956B. The volume magnetic susceptibility data for Holes 956A (0-157 mbsf) and 956B (157-697 mbsf) are plotted on Figures 33 and 37, respectively. In general, magnetic susceptibility trends downcore are useful for lithology interpretation and stratigraphic correlations between holes. At Site 956, this correlation was especially interesting relative to the volcanic intervals.

The magnetic susceptibility data for Hole 956A (Fig. 33) shows several high-amplitude spikes of over 500×10^{-6} SI units that are re-

Table 6. Inorganic geochemistry.

Core, section, interval (cm)	Depth (mbsf)	pH	Salinity (g/kg)	Cl (mmol/L)	Alkalinity (mmol/L)	SO ₄ (mmol/L)	Na (mmol/L)	K (mmol/L)	SiO ₂ (μmol/L)	Ca (mmol/L)	Mg (mmol/L)	Mg/Ca (molar ratio)
157-956A-												
1H-1, 145-150	1.45	7.74	34.5	559	3,549	38	440	10.6	459	10.4	52.6	5.08
2H-4, 145-150	12.05	7.54	35.0	552	3,832	39	473	11.7	527	9.9	53.5	5.39
3H-6, 145-150	24.55	7.47	35.5	560	4,513	38	479	11	427	8.8	54.5	6.21
4H-5, 140-150	32.50	7.47	34.5	567	4,552	36	479	11.6	520	8.3	54.9	6.63
5H-5, 140-150	42.00	7.40	34.0	562	4,865	36	473	11.3	648	8.7	53.5	6.17
6H-5, 140-150	51.50	7.48	35.0	567	4,482	36	475	11	605	8.8	53	5.99
7H-5, 140-150	61.00	7.88	35.0	567	4,817	35	468	10.7	563	8.6	51.8	6.00
8H-4, 140-150	69.00	7.56	35.0	567	4,717	34	469	10.5	548	8.8	50.1	5.68
9H-5, 140-150	80.00	7.57	35.0	567	4,052	31	475	10.1	499	8.5	47.9	5.63
10H-4, 140-150	88.00	7.55	34.0	567	3,472	31	472	9.2	534	7.8	42.9	5.51
12H-4, 140-150	107.00	7.58	34.0	568	3,691	27	472	8.9	534	9.6	44.1	4.61
14H-4, 140-150	126.00	7.57	34.0	564	3,059	24	470	8	548	9.7	40.7	4.19
16H-6, 140-150	148.00	7.72	33.5	569	1,914	22	478	7.1	235	10.5	36.9	3.50
157-956B-												
1R-2, 140-150	160.00	7.92	33.0	567	1,532	ND	ND	ND	ND	ND	ND	ND
5R-4, 140-150	201.30	7.76	32.0	572	0,812	10	473	4.6	150	14.9	24.7	1.66
10R-2, 135-150	246.45	7.80	32.0	577	0,721	10	478	3.7	128	15.8	25.7	1.63
14R-2, 130-150	284.80	7.80	32.5	578	0,724	ND	ND	ND	ND	ND	ND	ND
17R-2, 130-150	315.10	7.86	34.0	561	0,853	15	483	3.6	182	17.1	29	1.69
20R-5, 130-150	346.80	7.96	34.0	575	1,200	18	490	3.8	171	19	30.4	1.60
23R-4, 130-150	374.20	8.26	34.0	578	0,727	22	497	5.1	107	20.1	30.2	1.50
27R-4, 130-150	412.50	8.26	35.0	571	0,529	26	497	6	121	22.8	26.3	1.15
33R-2, 130-150	467.16	8.13	35.0	587	0,513	ND	ND	ND	ND	ND	ND	ND
37R-2, 20-45	505.00	7.68	35.0	587	0,361	28	468	8.5	285	26.4	20.9	0.79
41R-1, 61-81	542.51	8.00	36.0	589	0,352	28	483	9	285	33.4	21.2	0.64

Note: ND = not determined due to insufficient pore water.

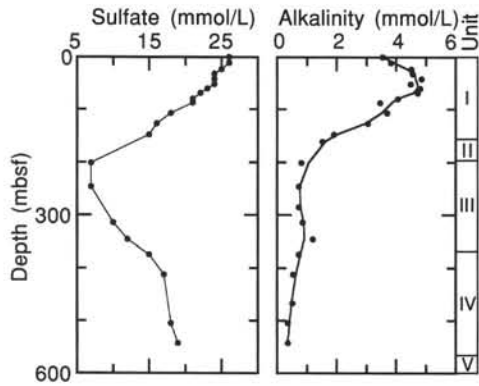


Figure 27. Interstitial-water sulfate and alkalinity, Site 956.

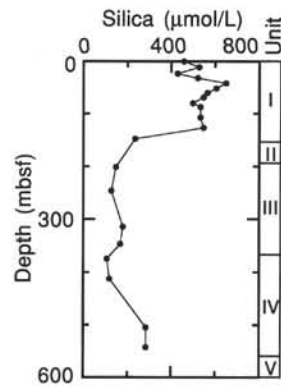


Figure 29. Interstitial-water silica, Site 956.

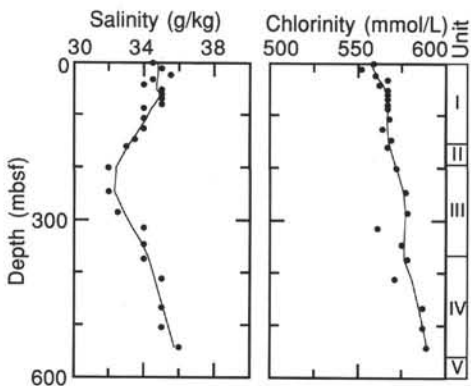


Figure 28. Interstitial-water salinity and chlorinity, Site 956.

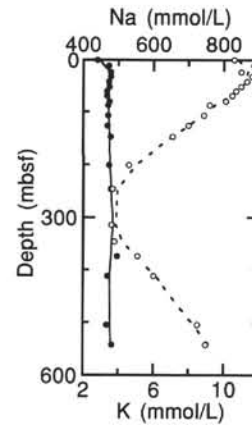


Figure 30. Interstitial-water sodium (filled circles) and potassium (open circles), Site 956.

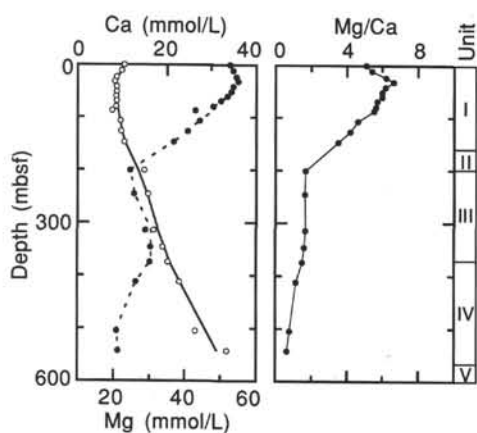


Figure 31. Interstitial-water calcium (open circles), magnesium (filled circles), and Mg/Ca ratio, Site 956.

lated mainly to sands. This behavior continues in Hole 956B (Fig. 37) up to 168 mbsf. The interval between 195 and 445 mbsf is characterized by a more quiet signal in the susceptibility, and no large peaks occur. Between 445 and 564 mbsf several high-amplitude magnetic susceptibilities were measured. For example, the vitric tuffs between 455 and 459 mbsf have values of up to 1500×10^{-6} SI units. The volcanic rich lithologic Unit V (below 564 mbsf) has again a high magnetic susceptibility. The values here are in general higher than 1000×10^{-6} SI units.

GRAPE Bulk Density

The GRAPE density data collected at Holes 956A and 956B are displayed in Fig. 34 and 38, respectively. GRAPE density data from the RCB cores were not corrected for drilling disturbances (reduced diameter), as the diameter of the recovered material was highly variable. Therefore, although the GRAPE data give an excellent indication of downcore trends, the use of GRAPE density values should be treated with caution. Along the profile for Hole 956A (Fig. 34), the larger peaks correspond to sand layers having densities up to 1.9 g/cm^3 . The general trend of the GRAPE density data shows on average an increase downcore from values close to 1.55 g/cm^3 near the mud line to 1.80 g/cm^3 at ~ 150 mbsf. Drilling disturbance may explain why some Hole 956B GRAPE density values are lower than those determined from discrete samples (up to, and occasionally greater than, a 0.3 g/cm^3 difference). In spite of the discrepancies in some intervals, GRAPE density shows a general downcore trend similar to that of the densities determined from discrete samples.

P-wave Velocity

P-wave velocity was measured at Hole 956A. Filtered data are plotted against depth on Figure 35. The velocity increases from about 1500 m/s at the seafloor to 1600 m/s at 157 mbsf, with variations between 1410 and 1660 m/s.

Natural Gamma Ray

The natural gamma ray emission was measured in both Holes 956A and 956B up to 584 mbsf. The total gamma counts and their percentages in the different energy windows are displayed in Figures 36 and 39. Channels 2 and 3 represent low energies, whereas Channels 4 and 5 represent high energies. Channel 1 is the sum of the other four channels.

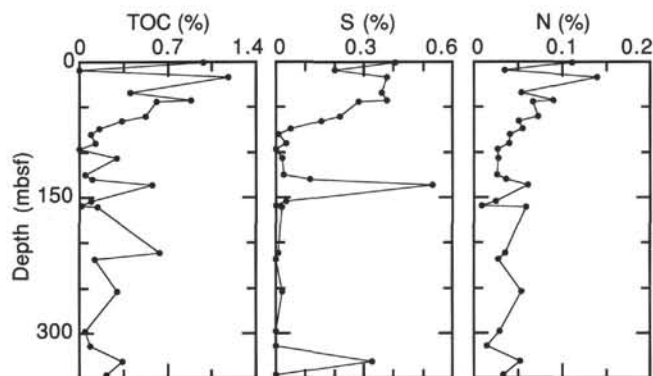


Figure 32. Concentration profiles of total organic carbon, total sulfur, and total nitrogen at Site 956.

In Hole 956A the average total gamma count is ~ 600 with a minimum between 5 and 9 mbsf (sand), and several peaks up to 820 counts occur further downcore; an interval between 146 and 155 mbsf has approximately 780 total counts.

In Hole 956B there is a broad interval with an increased natural gamma ray activity between 290 and 440 mbsf. At 290 mbsf the activity starts to increase and reaches its maximum at 348 mbsf, with around 1050 counts, at which the activity decreases slightly (values between 800 and 1000 counts). Below 440 mbsf no large peaks occur and the values are in less than 760 counts.

Correlation of MST results

Data collected from GRAPE density, magnetic susceptibility, natural gamma ray, and P-wave velocity sensors on Site 956 are shown in Figures 40 and 41; the crossplots for Hole 956A and 956B are presented in Figures 42 and 43, respectively. These data confirm the presence of significant variations in physical properties at a relatively fine scale. As expected there is a positive correlation between density and velocity. The correlation between the magnetic susceptibility, density, and natural gamma ray is more complicated. In general, high susceptibilities correlate positively with density and natural gamma ray. However, sometimes a negative correlation is observed. The density and natural gamma ray exhibit a positive correlation; high gamma counts are generally related to higher densities. One exception is the sand layer between 6 and 10 mbsf where a high density occurs yet has a minimum in the gamma counts.

Thermal Conductivity

Thermal conductivity measurements were routinely performed on sections 1, 3, and 5 of each core. Needles were inserted 50 cm from the top of each measured section on most cores from Hole 956A, from the mud line to a depth of 145 mbsf. The values for the thermal conductivity varies from 0.85 to $1.35 \text{ W/(m}\cdot\text{K)}$. The data are compiled in Table 8 and shown in Figure 44. A negative correlation is apparent between the thermal conductivity and the water content (Fig. 44); a low water content seems to be associated with a high thermal conductivity.

Discrete Measurements on Split Cores

Index Properties

Index properties, including wet- and dry-bulk density, water content, porosity, void ratio, and grain density were measured or calculated from weights and volumes of discrete samples, both in saturated and dry states. Sampling rate for index properties was approximately

Table 7. Elemental and organic carbon compositions of core samples, Site 956.

Core, section, interval (cm)	Depth (mbsf)	Inorganic carbon (%)	CaCO ₃ (wt%)	Total carbon (wt%)	TOC (wt%)	Total nitrogen (wt%)	Total sulfur (wt%)	C/N (ratio)
157-956A-								
1H-1, 56-57	0.56	5.72	47.6	6.70	0.98	0.11	0.40	8.9
2H-3, 50-51	9.60	10.12	84.3	9.50	BD	0.04	0.20	ND
3H-2, 19-20	17.29	5.49	45.7	6.67	1.18	0.14	0.38	8.4
4H-7, 35-36	34.45	6.19	51.6	6.59	0.40	0.05	0.36	8.0
5H-6, 34-35	42.44	5.20	43.3	6.09	0.89	0.09	0.38	9.9
6H-1, 22-23	44.32	6.54	54.5	7.15	0.61	0.07	0.28	8.7
7H-5, 83-84	60.43	4.31	35.9	4.83	0.52	0.07	0.22	7.4
8H-2, 58-59	65.18	6.70	55.8	7.03	0.33	0.05	0.16	6.6
9H-1, 138-139	73.98	7.42	61.8	7.58	0.16	0.06	0.05	2.7
9H-6, 69-70	80.79	7.17	59.7	7.26	0.09	0.04	0.01	2.3
10H-6, 67-68	90.27	8.18	68.1	8.31	0.13	0.04	0.03	3.3
11H-4, 75-76	96.85	8.18	68.1	8.12	BD	0.03	BD	ND
12H-4, 88-89	106.48	6.82	56.8	7.11	0.29	0.03	0.02	9.7
14H-4, 73-74	125.33	7.98	66.5	8.03	0.05	0.03	0.03	1.7
15H-1, 33-34	129.93	5.54	46.1	5.64	0.10	0.04	0.11	2.5
15H-5, 116-117	136.76	4.73	39.4	5.30	0.57	0.06	0.53	9.5
17H-4, 112-113	154.22	7.10	59.1	7.19	0.09	0.02	0.03	4.5
18X-1, 105-106	159.15	5.73	47.7	5.74	0.01	0.01	BD	1.0
157-956B-								
1R-3, 68-69	160.78	5.66	47.1	5.80	0.14	0.06	0.02	2.3
6R-5, 46-47	211.56	7.32	61.0	7.96	0.64	0.04	0.01	16.0
7R-3, 68-69	218.38	8.16	68.0	8.28	0.12	0.03	BD	4.0
11R-1, 97-98	254.17	3.83	31.9	4.13	0.30	0.05	0.02	6.0
15R-5, 5-6	297.75	5.57	46.4	5.62	0.05	0.03	BD	1.7
17R-3, 87-88	314.67	7.16	59.6	7.25	0.09	0.01	BD	9.0
19R-2, 40-41	331.80	2.37	19.7	2.71	0.34	0.05	0.33	6.8
20R-5, 64-65	346.14	4.09	34.1	4.30	0.21	0.03	BD	7.0

Note: BD = below detection; ND = not determined.

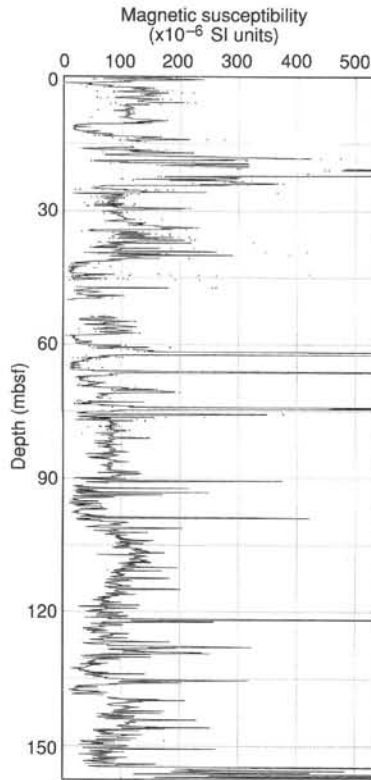


Figure 33. MST magnetic susceptibility, Hole 956A. Filtered data indicated by lines, raw data by discrete points.

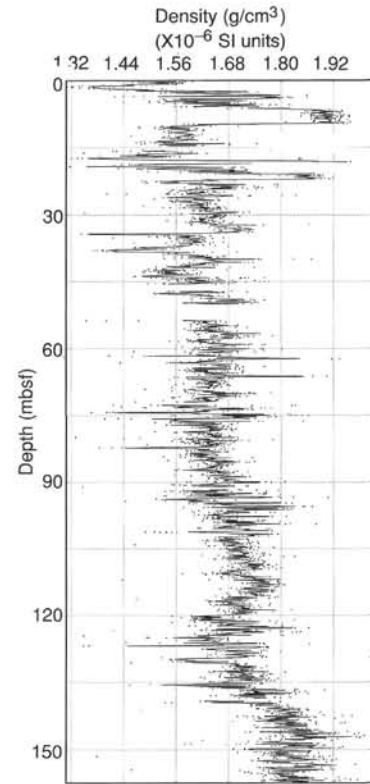


Figure 34. MST GRAPE density, Hole 956A. Filtered data indicated by lines, raw data by discrete points.

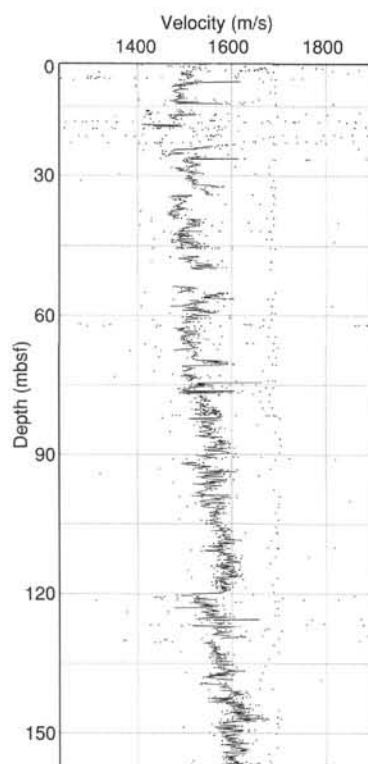


Figure 35. MST *P*-wave velocity, Hole 956A. Filtered data indicated by lines, raw data by discrete points.

one per section. Bulk density was calculated following Method B, dry-bulk density, grain density, porosity, and void ratio using Method C (see “Explanatory Notes,” and “Site 950,” this volume). Values of the index properties for Site 956 are presented in Table 9 and in Figure 45.

Lithologic Unit I (0–158 mbsf) is characterized by a downcore increase of bulk density as well as by a decrease in water content and porosity. The grain density is only slightly increasing with depth with values around 2.7 g/cm^3 .

Lithologic Unit II (158–195 mbsf), with its high content in volcanoclastic material, is characterized by high densities and by low water content and porosity. Bulk density increases up to 2.38 g/cm^3 , whereas the water content is around 20% at 195 mbsf.

Further downcore, bulk and grain density increase, without a large scatter, up to 270 mbsf, while water content and porosity decrease. Below this depth, all index properties remain almost constant to 435 mbsf (bulk density around 2.00 g/cm^3 , grain density 2.77 g/cm^3 , water content 25% and porosity 47%). This uniformity is due to the low volcanic content in this interval. Below this depth, density decreases to 550 mbsf, as porosity and water content increase.

The hyaloclastite tuffs and breccias in lithologic Unit V (564–697 mbsf) have a high bulk density (up to 2.9 g/cm^3 in some basaltic clasts). The same behavior is visible in the grain density, while the porosity and the water content show low values.

P-wave Velocity

The *P*-wave velocity was measured to 89 mbsf with the DSV. At Core 157-956A-10H the sediments became too lithified to use the DSV. After this, the Hamilton Frame was used to obtain compressional-wave velocities. Measurements were made with the core in the liner and typically one to five values per section were determined (Table 10 and Fig. 46).

The velocity increases almost linearly with depth from about 1.5 km/s at the mud line to 2.2 km/s at 564 mbsf with some interbedded

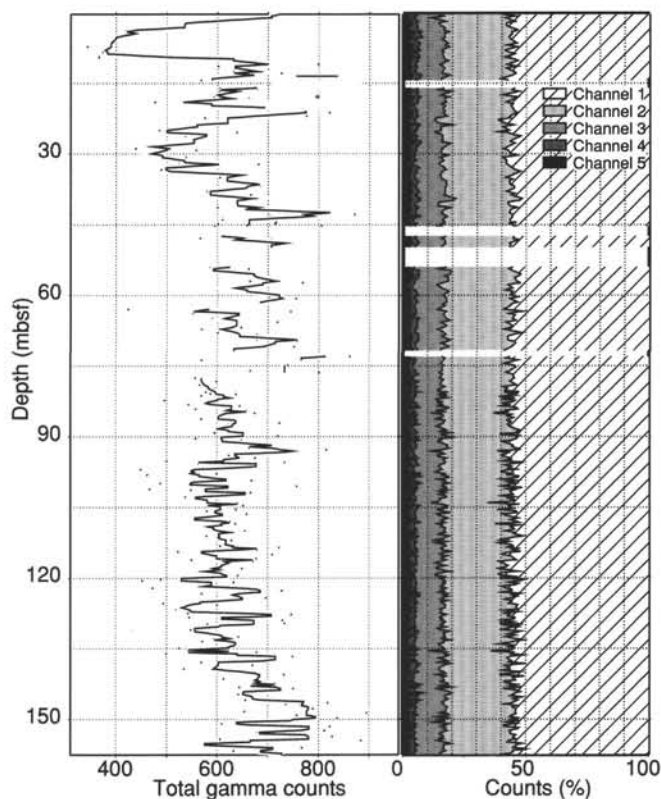


Figure 36. MST total natural gamma ray and percentage counts by channel, Hole 956A. Filtered data indicated by lines, raw data by discrete points.

intervals of high velocity representing mainly volcanic material. High velocities up to 5.2 km/s between 158 and 196 mbsf are related to basaltic lapillistones, clasts, and welded tuff. Further downcore there are two remarkable peaks caused by welded tuff. At 368 mbsf velocity was measured at 6.4 km/s, and at 445 mbsf velocity it was 5.2 km/s.

Lithologic Unit V (564–697 mbsf) is characterized by high velocities with a large scatter (2.0–6.7 km/s). In general, the fine grained breccias have a lower velocity than those that are coarse grained. Large lithic clasts generated especially high velocities.

Undrained Shear Strength

Undrained shear strength was measured with the vane shear device to a depth of 159 mbsf on Core 157-956A-18X. Beyond this depth, several meters of hard rock were encountered. Further downcore the sediments began cracking upon insertion of the vane. Between 10–160 mbsf, sediment strength was also estimated with the handheld penetrometer. A comparison of the results obtained by the two systems gives a fairly good correlation, although penetrometer readings tend to give higher values than those obtained with the vane shear. Data are presented in Table 11 and Figure 44.

Strength values increase downhole from very low values (near zero) on the seafloor to 170 kPa at about 160 mbsf. Strength can be correlated with water content (Fig. 44); higher water content corresponds to lower shear strength.

Discussion

The physical properties at Site 956 show a close relationship to the lithologic units. The intervals with high volcanoclastic content can be easily identified in the index properties, velocity, and magnetic susceptibility data.

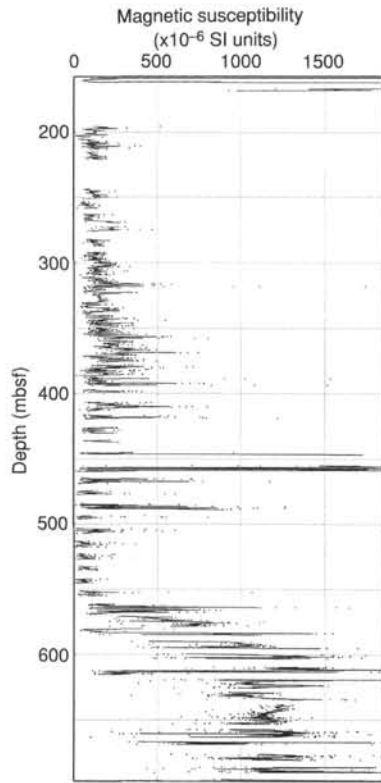


Figure 37. MST magnetic susceptibility, Hole 956B. Filtered data indicated by lines, raw data by discrete points.

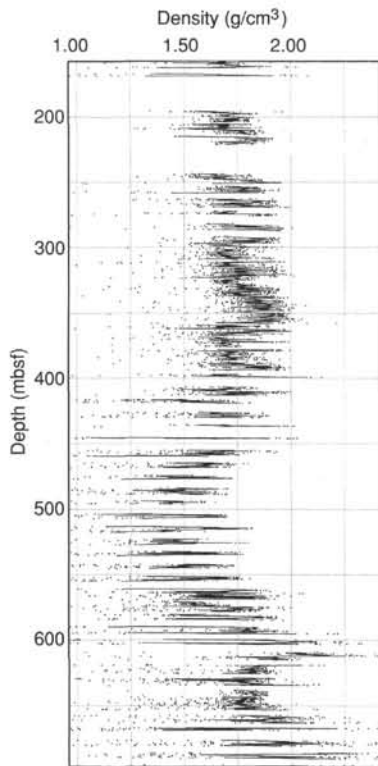


Figure 38. MST GRAPE density, Hole 956B. Filtered data indicated by lines, raw data by discrete points.

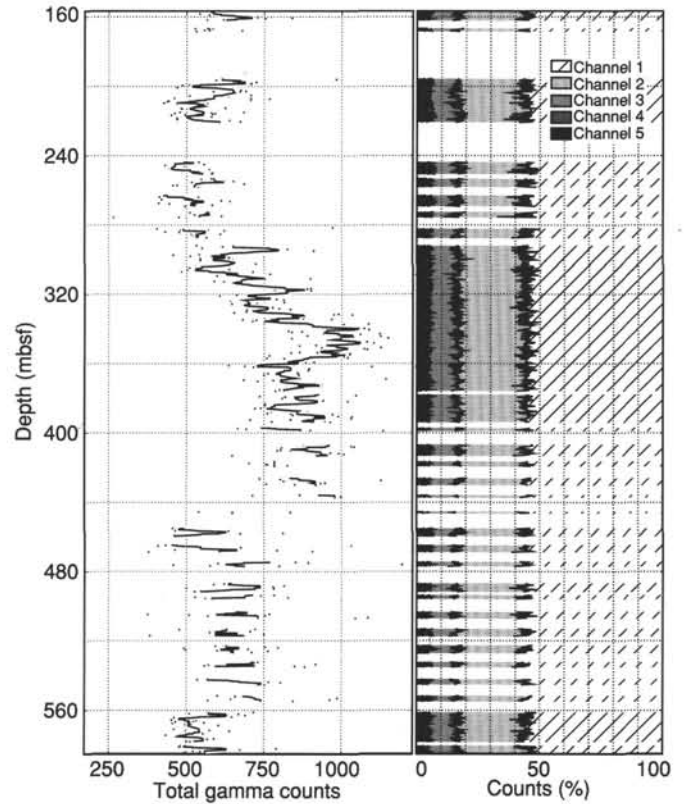


Figure 39. MST total natural gamma ray and percentage counts by channel, Hole 956B. Filtered data indicated by lines, raw data by discrete points.

The interval between 158 and 196 mbsf (lithologic Unit II), with its several high velocities and densities, represents one of the most prominent seismic reflectors (see “Underway Geophysics,” this chapter). It appears as a band of four high-amplitude reflections between 4800 and 4850 ms twt.

The absence of any magnetic susceptibility peaks in lithologic Unit III is remarkable. This interval represents the volcanic hiatus on Gran Canaria and contains large slumps. Index properties for this unit are very constant below 270 mbsf. An explanation for this may be that the slumped material is very well mixed, at least at the sample size scale.

Scatter in velocity in lithologic Unit V (564–697 mbsf) represents the heterogeneity of the deposited volcanoclastic material. Fine-grained material alternates with coarse grained material in which the large lithic clasts have a high velocity; the degree of welding also affects the velocity.

DOWNHOLE MEASUREMENTS

Logging operations

A full suite of three Schlumberger tool strings were run in Hole 956B. The quad combination, geochemical, and Formation Micro-Scanner tool strings provided comprehensive coverage of the open-hole section. The WHC was used during logging to counter ship heave resulting from the mild sea state conditions (0.2–0.75 m heave). The base of the drill pipe was set at 303 mbsf, below unstable hole conditions above. A summary of the logging tool strings used on Leg 157, the basis of their measurement principles, and logging operations are discussed in the “Explanatory Notes” chapter (this volume). A summary of the logging operations at Hole 956B is given in Table 12.

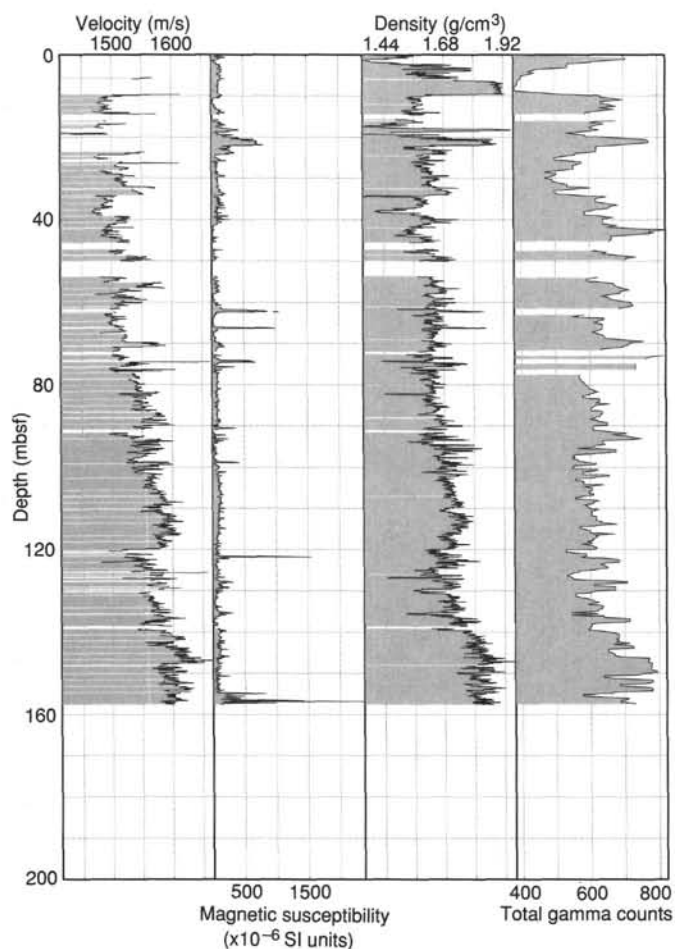


Figure 40. Filtered MST velocity, magnetic susceptibility, density, and natural gamma ray, Hole 956A.

The first tool string run, the quad combination, comprises the sonic (LSS), induction (DIT), density (HLDT), neutron porosity (CNT), and natural gamma-ray (NGT) tools, along with the Lamont-Doherty temperature logging tool. A downgoing log was recorded at 1500 ft/hr from the end of pipe to total depth of 703 mbsf. Total penetration in Hole 956B was 703 mbsf; therefore, no hole fill was encountered. A short upgoing log was recorded at 900 ft/hr from this depth to 577 mbsf. The main log followed from 703 mbsf to the end of pipe at 303 mbsf. The geochemical combination, comprising natural gamma-ray (NGT), aluminum (AACT), and gamma-ray spectrometry (GST) tools, recorded data from 703 mbsf to the mud line (303–0 mbsf, through pipe) at 550 ft/hr. Several different runs were made due to some temporary uphole hardware problems. A second run at the same logging speed recorded data from 703–517 mbsf. A third run, the FMS, comprising a natural gamma-ray tool in combination with an FMS, recorded two openhole runs. The first ran from 703 to 325 mbsf, and the second from 703 to 266 mbsf. Both were recorded at a logging speed of 1500 ft/hr.

Log Quality

The main logs recorded at Hole 956B are shown in Figures 47, 48, and 49 and are generally of high quality. Above 303 mbsf, the sonic, induction and density data are invalid, and the natural gamma-ray and other geochemical logs are highly attenuated by the presence of the drill pipe.

Hole 956B is rugose above about 450 mbsf, shown by the hole caliber in Figure 48, as a result the density log has suffered in quality. The white area in the center of the figure shows the diameter of a gauge hole drilled with the RCB coring bit, while the shaded areas show how much wider the hole was when logged than when originally drilled. When comparing log bulk density to discrete measurements on core, the log bulk density appears to have intervals of poor quality data which correlate with zones of wider, rugose borehole. The poor quality data occurs when pad contact with the borehole wall is incomplete, resulting in a small amount of borehole fluid being included with the measurement of sediment density.

The velocity data from the logs are of excellent quality. A minor amount of cycle skipping is present in the raw log data, but shipboard processing of the traveltimes eliminated these excursions. The sonic velocity presented in Figure 48 is the processed data.

Hole width also affects the natural gamma-ray activity log by raising the count rate where the hole is narrow and lowering it where it is wide. Post-cruise processing will correct for these environmental factors. A comparison of porosity calculated from the induction logs and measured on discrete core samples is shown in Figure 50.

Data from the geochemical logging tool require extensive post-cruise processing to convert the relative elemental yields into weight percent elements and oxides. The preliminary elemental yield data can be used to determine relative elemental variations.

Results

Variation of Logs with Depth

The openhole interval logged in Hole 956B (~303–703 mbsf) covers lithologic Units III to V (late to middle Miocene), which are based on the recovered cores (see "Lithostratigraphy," this chapter). The sequence is dominated by hemipelagic fine grained sediments interbedded with volcanoclastic material principally in the lower section.

The drilled sequence is subdivided into log units since the lithostratigraphy at this site is principally defined by variations in sand content and type of volcanoclastic material, rather than by bulk formation properties measured by the logging tools.

Log unit I (303–450 mbsf) is characterized by fairly constant resistivity and sonic velocity, which slowly increases linearly with depth (Fig. 48). This unit has relatively high log-carbonate values that decrease with depth and correspond to an increasing total gamma-ray trend with depth (Fig. 47). Log unit I encompasses lithologic Units III and the top of IVa and is composed predominantly of a nanofossil mixed sediment. In the lower half of the log unit there is more abundant volcanoclastic material, corresponding to lithologic Subunit IVa, some of which is thick enough to appear in the total gamma-ray logs as a series of high spikes.

The transition downward to log Unit II (450–562 mbsf) is marked by a sharp increase in bulk density, resistivity, and sonic velocity and by a distinct decrease in the rugosity of the borehole (Fig. 48). The gamma-ray log has lower average values than it does in log Unit I above, but it has a higher degree of variability. The generally higher variability of the logs reflects the increase in thickness and abundance of the volcanoclastic material. The carbonate values are lower than in log Unit I above (Fig. 49).

The transition between log Units I and II seems to correspond to the boundary between the interpreted seismic Units D and E (see "Underway Geophysics"). Seismic Unit D (Fig. 2) appears to lie unconformably on the Unit E below. This hypothesis is supported by the abrupt change in character of the physical logs (Fig. 48) and a change in character of the dip information from the FMS.

The transition downwards into log Unit III (562–703 mbsf) is characterized by an abrupt decrease in the gamma-ray logs (Fig. 47), which correlates with the abrupt disappearance in the felsic and the beginning of the mafic material noted in the cores. This boundary

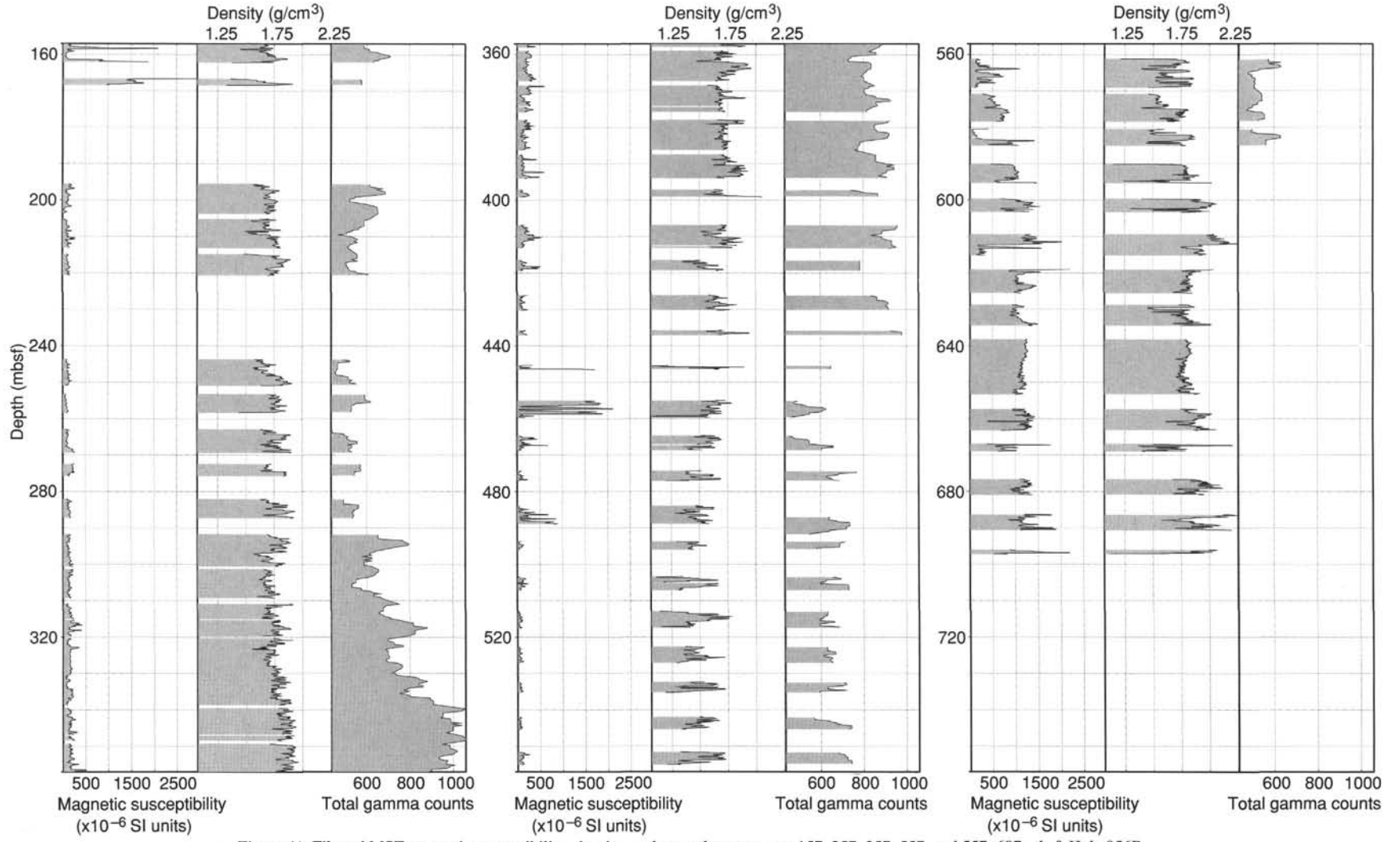


Figure 41. Filtered MST magnetic susceptibility, density, and natural gamma ray, 157-357, 357-557, and 557-697 mbsf, Hole 956B.

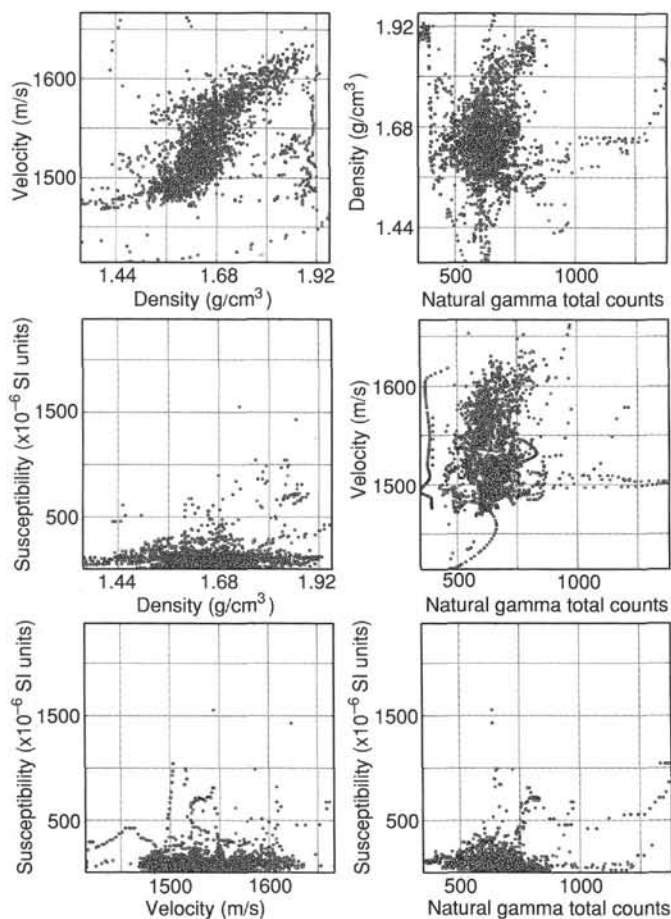


Figure 42. Crossplots of MST velocity, magnetic susceptibility, density, and natural gamma ray, Hole 956A.

corresponds to the top of lithostratigraphic Unit V and approximately to the top of seismic stratigraphic Unit F and it represents the end of the Gran Canaria basaltic shield phase of volcanism. Bulk density, resistivity, and sonic velocity increase represent the compositional change to the more dense mafic material.

The core material recovered consists of graded basaltic breccia and hyaloclastic tuff units interpreted as debris flows. The graded nature of these flows is well exhibited by the physical logs of bulk density, resistivity, and sonic velocity. The percentage abundance and clast size of the basaltic breccia increases towards the base of the debris flows and is reflected by increasing bulk density, resistivity, and sonic velocity with depth within each flow. Two main debris flows are visible within log Unit III, the lowermost of which is at least 83 m thick, as the base of the flow is not reached in the log or core data.

Above the lowermost debris flow is a 5 m thick bed of naturally highly radioactive material (615–620 mbsf, Fig. 47). This bed has total gamma-ray counts up to 350 API units due principally to Th concentrations up to 60 ppm (Fig. 47). Uranium is also significantly higher than in the rest of the hole at ~4 ppm, but K is no higher than the sediments in log Units I and II above. In the core, this interval corresponds to a foraminifer sand rich in sphene and zircon, which can contain quantities of Th, although it is likely that a mineral such as monazite would be needed to give such very high Th concentrations. Some of this heavy mineral sand was recovered in the cores, which is a distinct unit ~5 m thick in the logs. The origin of this type of placer sand material would imply an evolved plutonic source; therefore, it is possible that it derived from beach sand deposits on the African margin.

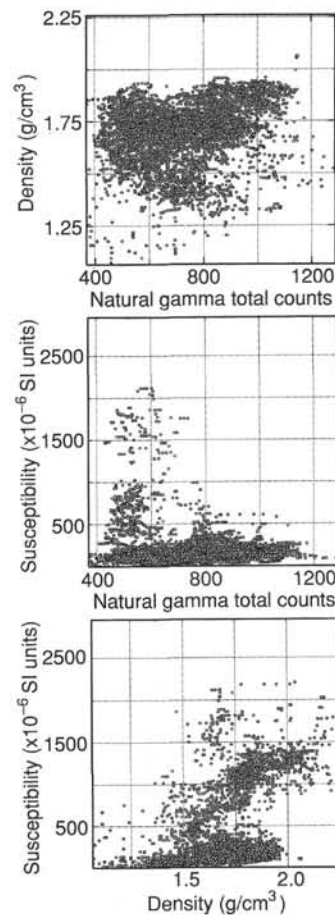


Figure 43. Crossplots of MST magnetic susceptibility, density, and natural gamma ray, Hole 956B.

Temperature

The Lamont-Doherty temperature tool was deployed on the quad combination tool string in Hole 956B. An accurate thermal gradient cannot be obtained from this measurement; cold seawater, which is circulated in the hole during drilling, cools the adjacent formation. A minimum of three bottom hole temperature measurements, taken over a period of time, are required for extrapolating the virgin bottom hole temperature and calculating the true thermal gradient. Nevertheless, a temperature of 10.8°C, obtained at 700 mbsf, indicated that the thermal gradient must be greater than 10.4°C/km, since the mud line temperature was 3.5°C (Fig. 51).

SEDIMENT ACCUMULATION RATES

A sediment accumulation rate curve (Fig. 52) was calculated for Site 956 based on 21 nannofossil datums, 12 foraminifer datums, 4 paleomagnetic datums, and a volcanoclastic radiometric age correlated to the sequence on Gran Canaria for a total of 38 control points over 657.82 m of sediment (Table 13).

The upper 380 m of the site, within lithologic Units I, II, and III (see "Lithostratigraphy," this chapter), contain chaotically disturbed sediments. Every effort was made to sample undisturbed pelagic sediments for datum control; however, even if a section looked undisturbed, it may still have been within a slumped unit. Slumping is evident in the biostratigraphic data by repeated sections in the

Table 8. Thermal conductivity measurements, Hole 956A.

Core, section, interval (cm)	Depth (mbsf)	TCcorr (W/mK)	Standard error (W/mK)	Drift (°/min)
157-956A-				
1H-1, 50	0.50	1.037	0.01316	-0.014
1H-3, 50	2.89	1.000	0.01141	0.010
1H-5, 50	5.31	1.216	0.01192	0.009
2H-1, 50	6.60	0.914	0.01087	-0.028
2H-5, 50	12.60	1.276	0.01085	0.026
3H-3, 50	19.10	0.965	0.01228	-0.009
3H-5, 50	22.10	0.993	0.01269	-0.036
4H-1, 50	25.60	1.087	0.01499	0.036
4H-3, 50	28.60	1.349	0.00907	0.033
4H-5, 50	31.60	0.960	0.01379	-0.020
5H-1, 50	35.10	1.155	0.00885	0.005
5H-3, 50	38.10	0.987	0.01169	0.009
5H-5, 50	41.10	1.279	0.01241	0.012
6H-1, 50	44.60	0.991	0.00906	-0.028
6H-3, 50	47.60	0.938	0.01114	-0.006
7H-1, 50	54.10	0.976	0.01056	-0.023
7H-3, 50	57.10	1.250	0.00788	0.035
8H-1, 50	63.60	1.109	0.00643	0.024
8H-3, 50	66.60	1.238	0.00896	0.012
8H-5, 50	69.60	0.953	0.01148	-0.019
9H-1, 50	73.10	1.194	0.01049	-0.002
9H-3, 50	76.10	1.060	0.00664	-0.017
9H-5, 50	79.10	1.133	0.00913	-0.031
10H-1, 50	82.60	1.039	0.01421	0.008
10H-3, 50	85.60	1.101	0.01445	0.011
10H-5, 50	88.60	1.293	0.01249	0.024
11H-1, 50	92.10	1.027	0.01358	0.028
11H-3, 63	95.23	1.150	0.00913	0.013
11H-5, 50	98.10	0.850	0.00935	-0.037
12H-3, 50	104.60	1.088	0.01064	-0.028
13H-1, 50	111.10	1.119	0.00586	-0.012
13H-3, 50	114.10	1.176	0.01154	-0.003
13H-5, 50	117.10	1.169	0.00901	0.037
14H-1, 50	120.60	0.996	0.01100	-0.033
14H-3, 50	123.60	1.178	0.01022	0.006
14H-5, 50	126.60	1.353	0.01163	0.001
15H-1, 50	130.10	1.009	0.01195	-0.020
15H-3, 50	133.10	1.206	0.01130	0.020
15H-5, 50	136.10	1.105	0.01396	0.037
16H-1, 50	139.60	1.126	0.01028	0.004
16H-3, 50	142.60	1.269	0.00945	0.011
16H-5, 50	145.60	1.182	0.00694	0.006

Note: TCcorr = thermal conductivity corrected for drift.

Pliocene and possibly a repeated section in the Miocene (see "Biostratigraphy," this chapter).

The sedimentation accumulation rate is ~26 m/m.y. from zero to 50 mbsf. From 50 to ~354 mbsf the sedimentation rate does not reflect the true sedimentation rate at Site 956, but rather it reflects an increased rate caused by numerous allochthonous units.

The sediment accumulation rate, within lower Unit III, from 354.3 to 389.69 mbsf, is approximately 39 m/m.y., which may be a representative sedimentation rate for this interval since there were no obvious repeated sections and no obvious slumping below approximately 375 mbsf.

A hiatus, spanning a minimum of 0.6 m.y., between 8.8 and 9.4 Ma is present between 399.07 and 413.3 mbsf near the boundary between lithologic Unit III and Subunit IVa. This hiatus is also present at Sites 954 and 955. A second hiatus, within lithologic Subunit IVa, spans a minimum of 0.8 m.y. from 9.99 and 10.8 Ma and is present between 445.35 and 446.30 mbsf. The sedimentation rate in the upper part of Subunit IVa between 413.3 and 436.47 mbsf is ~60 m/m.y., which is the same sedimentation rate as is found at Site 955 for lithologic Subunit IVa.

Below 446.30 mbsf there is considerably less stratigraphic control, with only three biostratigraphic datums and one volcanic datum. These do not show a consistent relationship with the paleomagnetic data. The volcanic datum at 564 mbsf is a distinct unit correlated to the P1 ignimbrite (~14 Ma on Gran Canaria, see "Lithostratigraphy" section, this chapter). The biostratigraphic data indicate a sedimentation rate of 28 m/m.y. between 457.49 and 513.80 mbsf for the lower

part of lithologic Subunit IVa and upper part of Subunit IVb. From 513.8 to 657.82 mbsf the rate increases within lithologic Subunit IVb and Unit V to a very high 144 m/m.y., reflecting the rapid deposition of debris flows in Unit V and the abundant volcanoclastic input in lower Subunit IVb. The paleomagnetic data below 466 mbsf indicate older ages than either the biostratigraphic data or the volcanic age. Shore-based work will be needed to sort out these discrepancies at this complex site.

IN-SITU TEMPERATURE MEASUREMENTS

Three ADARA temperature measurements were made while coring Hole 956A. The measurements were taken during Cores 157-956A-5H (44.1 mbsf), 157-956A-8H (72.6 mbsf), and 157-956A-11H (101.1 mbsf). Sub-bottom equilibrium temperatures were extrapolated from synthetic curves which were constructed to fit transient temperature data. An equilibrium temperature for Core 157-956A-8H was calculated at 6.315°C but this number was considered unreliable because the probe began to heat up, perhaps due to frictional heating; while this temperature profile was being recorded, motion from the heave compensator was unusually high. However, the results of this temperature fit are presented in Figure 53. Cores 157-956A-5H (Fig. 54) and 157-956A-11H (Fig. 55) gave more reliable equilibrium temperatures of 4.578°C and 6.047°C, respectively. The mud line temperature was calculated at 2.62°C for the site.

From temperature measurements downhole, a geothermal gradient can be calculated, and along with an estimate of thermal conductivity, provides an estimate of heat flow. Plotting the sub-bottom equilibrium temperatures along with the mud line temperature vs. depth, the geothermal gradient was approximated at 33.51°C/km by using a linear mean (Fig. 56). Core 157-956A-8H was not used in calculating the geothermal gradient because of the unreliability of the measurement. Heat flow was then calculated by multiplying the geothermal gradient by the average thermal conductivity for the hole (see "Physical Properties," this chapter). Thermal conductivity in Hole 956A had an average value of approximately 1.11 W/(m-K), resulting in a heat flow value of 37.20 mW/m².

ROCK EVAL

Characterization of Organic Matter at Sites 953, 955, and 956 using Rock-Eval Pyrolysis

The preservation of labile organic matter in seafloor sediments depends on the presence of an oxygen-depleted water column and/or high sedimentation rates. Organic matter preservation on the MAP is controlled largely by turbidity currents which have very rapidly redepositing organic-rich sediments derived from the North West African continental margin. Extensive post-depositional oxidation of this organic matter is confined to turbidite tops, where seawater oxygen has burnt downward into the sediment column while each turbidite remained exposed on the seafloor. Comparable sediments form a minor component of the sequence in the deeper part of the VICAP Site 953. Elsewhere in the VICAP area, organic-rich sediments occur predominantly in the slumped intervals at Sites 955 and 956, to the south of Gran Canaria. Once again, gravity-driven redeposition of sediments derived from the continental margin provides a mechanism for preserving organic matter in these deep-water areas. Rock-Eval pyrolysis was used to assess the character of organic matter at these three VICAP sites, 953, 955, and 956.

Samples

A total of 26 samples were analyzed on the Rock-Eval instrument (Table 14). Samples were selected based on results of CNS-analyses

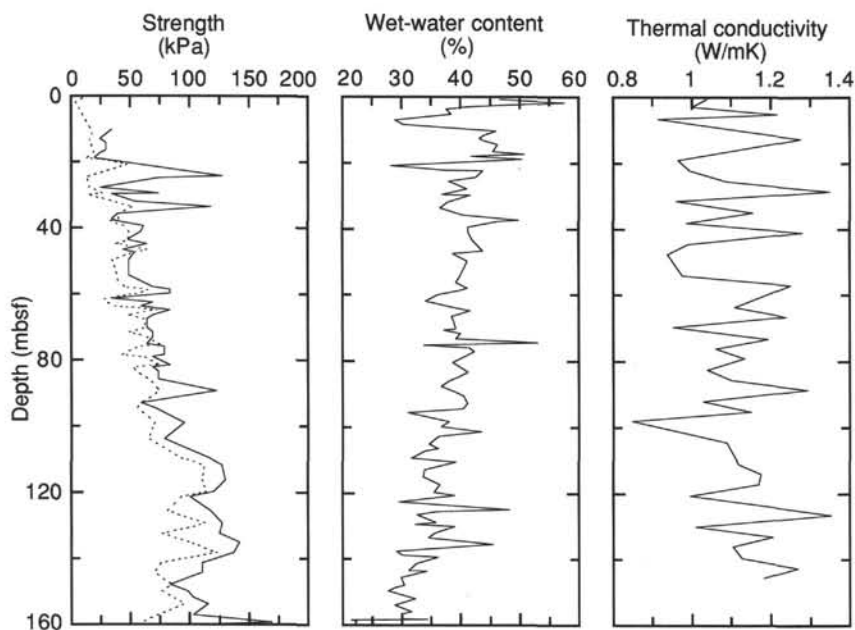


Figure 44. Strength data determined by vane shear (dotted line) and handheld penetrometer (solid line) methods, wet-water content, and thermal conductivity, Hole 956A.

and consisted of two categories: (1) Those containing more than 1.2% organic carbon; (2) Those containing between 0.3%–1.0% organic carbon (Fig. 57; Table 14). Sample weights analyzed were 100–101 mg. Measured parameters followed those obtained for the MAP sites (see Site 952 Rock-Eval section).

T_{\max} for the VICAP samples ranged from 328°–432°C, indicating that these sediments may be classified as immature (Fig. 12). A maximum value of 432°C was found at 818 mbsf (TOC = 0.39%) in Site 953. The average PI value was around 0.2 for organic-rich turbidites from Site 953. For Sites 955 and 956, PI varied between 0.2–0.4, which places all of these sediments in the oil formation zone (Peters, 1986).

Origin of the Organic Matter

HI is plotted against OI for Sites 953, 955, and 956 in Figure 58. The majority of the data points fall in a broad field between kerogen type II (marine) and type III (terrigenous). This is interpreted as representing a mixture between the two types of organic matter precursor. Bearing in mind likely mineral matrix effects, the data set suggests that the marine component prevails, which is consistent with C/N ratio data for these sites.

Source Rock Potential

$S_1 + S_2$ values obtained for the VICAP sites varied between 0.17 and 7.78 mgC/g sediment (Fig. 59; Table 14). Samples yielding values of >5 mgC/g are considered to be good source rocks. It is difficult to give a meaningful average value for the VICAP sites because of the inhomogeneous and slumped character of the sediments. Most samples have values of <3 mgC/g, indicating a fair source rock.

Conclusions

Organic carbon values of 0.5% were recorded only in the upper 150 m of Sites 953, 955, and 956. There was no apparent variation

with lithology. The sediments represent a source rock of only fair potential for gas and oil, and have a low level of thermal maturity.

REFERENCES

- Bogaard, P., Schmincke, H.-U., Freundt, A., Hall, C., and York, D., 1988. Eruption ages and magma supply rates during the Miocene evolution of Gran Canaria: single crystal $^{40}\text{Ar}/^{39}\text{Ar}$ laser ages. *Naturwissenschaften*, 75:616–617.
- Freundt, A., and Schmincke, H.-U., 1995. Eruption and emplacement of a basaltic welded ignimbrite during caldera formation on Gran Canaria. *Bull. Volcanol.*, 56:640–659.
- Peters, K.E., 1986. Guidelines for evaluating petroleum source rocks using programmed pyrolysis. *AAPG Bull.*, 70:318–329.
- Rio, D., Fornaciari, E., and Raffi, I., 1990. Late Oligocene through early Pleistocene calcareous nannofossils from western equatorial Indian Ocean (Leg 115). In Duncan, R.A., Backman, J., Peterson, L.C., et al., *Proc. ODP, Sci. Results*, 115: College Station, TX (Ocean Drilling Program), 175–235.
- Rothwell, R.G., 1989. *Minerals and Mineraloids in Marine Sediments: An Optical Identification Guide*: Basking, UK (Elsevier Appl. Sci. Publ.).
- Schmincke, H.-U., 1982. Volcanic and chemical evolution of the Canary Islands. In von Rad, U., Hinz, K., Sarnthein, M., and Seibold, E. (Eds.), *Geology of the Northwest African Continental Margin*: Berlin (Springer), 273–306.
- , 1994. *Geological Field Guide: Gran Canaria* (7th ed.): Kiel, Germany (Pluto Press).
- Schmincke, H.-U., and von Rad, U., 1979. Neogene evolution of Canary Island volcanism inferred from ash layers and volcanoclastic sandstones of DSDP Site 397 (Leg 47A). In von Rad, U., Ryan, W.B.F., et al., *Init. Repts. DSDP*, 47 (Pt. 1): Washington (U.S. Govt. Printing Office), 703–725.
- Young, J.R., 1990. Size variation of Neogene *Reticulofenestra* coccoliths from Indian Ocean DSDP cores. *J. Micropaleontol.*, 9:71–85.
- Young, J.R., Flores, J.-A., and Wei, W., 1994. A summary chart of Neogene nannofossil magnetobiostratigraphy. *J. Nannoplankton Res.*, 16:21–27.

Ms 1571R-110

NOTE: For all sites drilled, core-description forms (“barrel sheets”) and core photographs can be found in Section 6, beginning on page 561. Smear-slide and thin-section data are given in Section 7, beginning on page 835. The CD-ROM (back pocket, this volume) contains physical properties and geochemical data, MST data, logging data, and color core photographs (Sites 950 and 953 only).

Table 9. Index properties, Site 956.

Core, section, interval (cm)	Depth (mbsf)	WCw (%)	WCd (%)	BD _b (g/cm ³)	BD _c (g/cm ³)	GD _b (g/cm ³)	GD _c (g/cm ³)	DD _b (g/cm ³)	DD _c (g/cm ³)	Por _b (%)	Por _c (%)	VR _b	VR _c
157-956A-													
1H-1, 73-75	0.73	46.67	87.53	1.54	1.54	2.78	2.76	0.82	0.82	70.36	70.19	2.37	2.35
1H-2, 31-33	1.81	57.47	135.14	1.42	1.39	2.92	2.67	0.60	0.59	79.40	77.90	3.85	3.53
1H-3, 44-46	2.83	41.90	72.12	1.64	1.61	2.88	2.74	0.95	0.94	66.99	65.82	2.03	1.93
1H-4, 44-46	3.75	37.61	60.27	1.72	1.68	2.93	2.74	1.08	1.05	63.30	61.68	1.72	1.61
1H-5, 44-46	5.25	38.40	62.33	1.70	1.67	2.89	2.74	1.05	1.03	63.72	62.48	1.76	1.67
2H-1, 79-81	6.89	28.93	40.70	1.89	1.85	2.87	2.76	1.34	1.32	53.26	52.31	1.14	1.10
2H-2, 79-81	8.39	30.25	43.37	1.86	1.82	2.88	2.75	1.30	1.27	54.96	53.78	1.22	1.16
2H-3, 113-115	10.23	45.96	85.05	1.55	1.55	2.78	2.74	0.84	0.84	69.74	69.49	2.30	2.28
2H-4, 96-98	11.56	44.03	78.67	1.56	1.57	2.67	2.69	0.87	0.88	67.19	67.42	2.05	2.07
2H-5, 28-30	12.38	43.17	75.98	1.55	1.58	2.54	2.68	0.88	0.90	65.36	66.55	1.89	1.99
2H-5, 98-100	13.08	43.61	77.33	1.60	1.58	2.81	2.74	0.90	0.89	67.93	67.41	2.12	2.07
2H-6, 89-91	14.49	46.20	85.86	1.58	1.54	2.93	2.72	0.85	0.83	71.06	69.50	2.46	2.28
3H-1, 88-90	16.48	45.45	83.33	1.54	1.55	2.65	2.72	0.84	0.85	68.28	68.91	2.15	2.22
3H-2, 14-16	17.24	50.80	103.25	1.48	1.47	2.71	2.64	0.73	0.72	73.19	72.67	2.73	2.66
3H-2, 76-78	17.86	41.83	71.90	1.63	1.61	2.85	2.74	0.95	0.94	66.67	65.76	2.00	1.92
3H-3, 33-35	18.93	50.35	101.42	1.48	1.48	2.72	2.68	0.74	0.73	72.94	72.60	2.69	2.65
3H-4, 77-79	20.87	28.10	39.08	1.89	1.86	2.81	2.72	1.36	1.34	51.74	50.94	1.07	1.04
3H-5, 64-66	22.24	37.48	59.95	1.71	1.68	2.87	2.72	1.07	1.05	62.66	61.42	1.68	1.59
3H-5, 81-83	22.41	43.75	77.77	1.57	1.49	2.66	2.29	0.88	0.84	66.90	63.44	2.02	1.74
3H-6, 124-126	24.34	42.56	74.09	1.60	1.59	2.73	2.69	0.92	0.91	66.42	66.09	1.98	1.95
4H-1, 45-47	25.55	38.01	61.31	1.68	1.66	2.77	2.69	1.04	1.03	62.37	61.72	1.66	1.61
4H-2, 123-125	27.83	41.00	69.48	1.62	1.62	2.73	2.71	0.96	0.95	64.92	64.74	1.85	1.84
4H-3, 141-143	29.51	36.76	58.13	1.68	1.69	2.68	2.74	1.06	1.07	60.35	60.82	1.52	1.55
4H-4, 19-21	29.79	41.54	71.06	1.60	1.61	2.68	2.70	0.94	0.94	65.05	65.15	1.86	1.87
4H-5, 91-93	32.01	37.76	60.66	1.69	1.66	2.79	2.67	1.05	1.03	62.31	61.26	1.65	1.58
4H-6, 104-106	33.64	36.47	57.41	1.72	1.69	2.83	2.71	1.09	1.08	61.30	60.30	1.58	1.52

Notes: WCw = water content (% wet sample weight), WCD = water content (% dry sample weight), BD = bulk density, GD = grain density, DD = dry density, Por = porosity, and VR = void ratio. Suffixes "b" and "c" on column heads indicate value calculated using Method B and Method C, respectively (see "Explanatory Notes" chapter, this volume).

Only a part of this table is reproduced here. The entire table appears on the CD-ROM (back pocket).

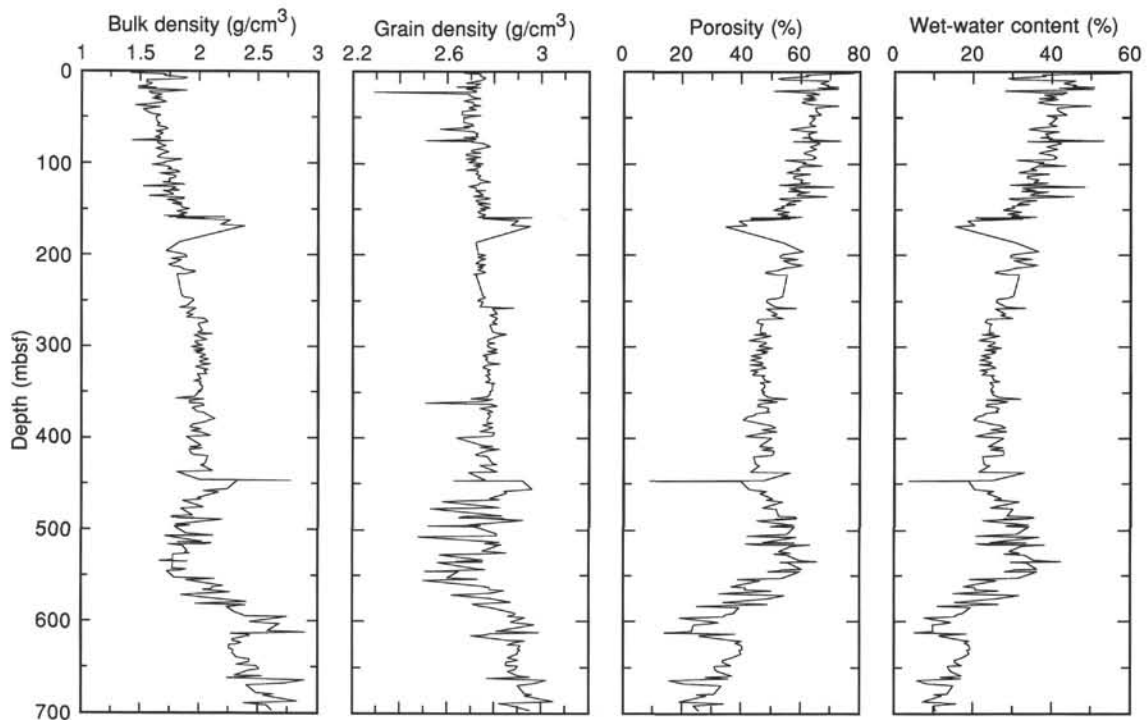


Figure 45. Bulk density (Method B), grain density (Method C), porosity (Method C), and wet-water content, Site 956.

Table 10. Compressional-wave velocities, Site 956.

Core, section, interval (cm)	Depth (mbsf)	Velocity (km/s)	Tool	Temperature (°C)
157-956A-				
1H-1, 76-83	0.76	1.54	DSV	20.9
1H-2, 30-37	1.80	1.52	DSV	19.7
2H-3, 114-121	10.24	1.53	DSV	20.5
2H-4, 96-103	11.56	1.54	DSV	19.8
2H-5, 99-106	13.09	1.54	DSV	20.2
2H-6, 66-73	14.26	1.54	DSV	20.1
3H-1, 89-96	16.49	1.55	DSV	19.5
3H-2, 14-21	17.24	1.54	DSV	
3H-3, 25-32	18.85	1.52	DSV	19.4
3H-6, 125-132	24.35	1.52	DSV	20.7
3H-7, 37-44	24.97	1.54	DSV	20.4
4H-2, 124-131	27.84	1.59	DSV	20.1
4H-3, 142-149	29.52	1.60	DSV	20.5
4H-4, 20-27	29.80	1.58	DSV	20.4
4H-5, 93-100	32.03	1.60	DSV	21.3
5H-1, 122-129	35.82	1.56	DSV	20.7
5H-2, 132-139	37.42	1.52	DSV	19.7
5H-3, 15-22	37.75	1.55	DSV	20.3
5H-4, 35-42	39.45	1.60	DSV	20.0
5H-5, 72-79	41.32	1.56	DSV	20.7

Notes: Temperature = temperature of the sample. Tools are DSV or Hamilton Frame.

Table 11. Strength measurements, Site 956.

Core, section, interval (cm)	Depth (mbsf)	Pk str (kPa)	Res (kPa)	Pen (kPa)
157-956A-				
1H-1, 76-77	0.76	10	3	
1H-2, 31-32	1.81	4	2	
2H-3, 108-109	10.18			34
2H-3, 114-115	10.24	17	12	
2H-4, 91-92	11.51			29
2H-4, 97-98	11.57	18	10	
2H-5, 93-94	13.03			25
2H-5, 99-100	13.09	16	8	
2H-6, 60-61	14.20			29
2H-6, 67-68	14.27	16	9	
3H-1, 83-84	16.43			29
3H-1, 89-90	16.49	18	11	
3H-2, 8-9	17.18			24
3H-2, 15-16	17.25	19	11	
3H-3, 16-17	18.76			20
3H-3, 25-26	18.85	13	7	
3H-4, 65-66	20.75	47	15	
3H-5, 59-60	22.19			83
3H-6, 117-118	24.27			128
3H-6, 125-126	24.35	13	7	

Notes: Pk str = peak strength, undrained shear strength as measured by the vane shear. Res = residual shear strength, Pen = unconfined shear strength as measured by the penetrometer, converted to kPa.

Only a part of this table is reproduced here. The entire table appears on the CD-ROM (back pocket).

Only a part of this table is reproduced here. The entire table appears on the CD-ROM (back pocket).

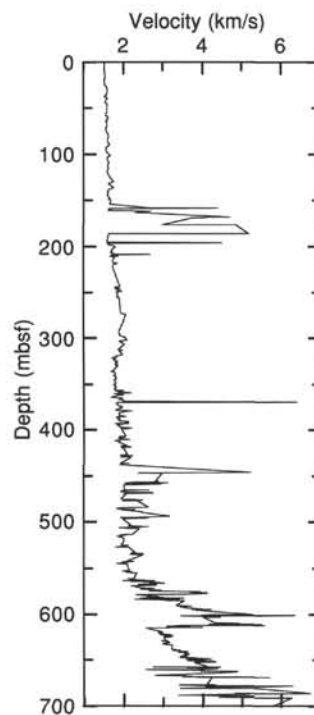


Figure 46. P-wave velocity measured by DSV and Hamilton Frame, Site 956.

Table 12. Summary of logging operations at Hole 956B.

Date (September 1994)	Time (UTC)	
21	00:20	Last core on deck. Prepare hole for logging. Hole displaced with sepolite mud for logging operations.
	12:15	Hole preparation complete, rig up wireline.
	13:40	RIH with NGT-LSS-CNT-HLDT-DIT (+TLT)
	15:05	Start downgoing log from EOP to TD (703 mbsf).
	15:56	Uplog at 900 ft/hour from 703 mbsf to 577 mbsf. RIH to TD.
	16:26	Main uplog at 900 ft/hour from 703 mbsf to EOP at 303 mbsf. HLDT caliper off at 321 mbsf. POOH.
	20:25	RIH with NGT-ACT-GST (+TLT)
	22:25	Uplog from 703 mbsf at 550 ft/hour to 682 mbsf; problem with depth counter. RIH to TD. Second uplog from 703 to 645 mbsf where uphole hardware malfunction.
	23:05	Uplog from 645 mbsf at 550 ft/hour, log terminated at 531 mbsf by uphole hardware failure.
	22	00:02
04:00		Uplog at 550 ft/hour from 703 to 517 mbsf. POOH.
06:30		Rig up NGT-FMS.
07:10		RIH with NGT-FMS
08:20		Uplog at 1500 ft/hour from 703-325 mbsf. RIH for repeat.
09:27		Uplog at 1500 ft/hour from 703-266 mbsf. POOH.
11:45		Tool out of hole. Rig down.
12:15		End of logging operations.

Note: Drillers TD = 703.5 mbsf, WD = 3453.4 mbrf, EOP = 303.7 mbsf.

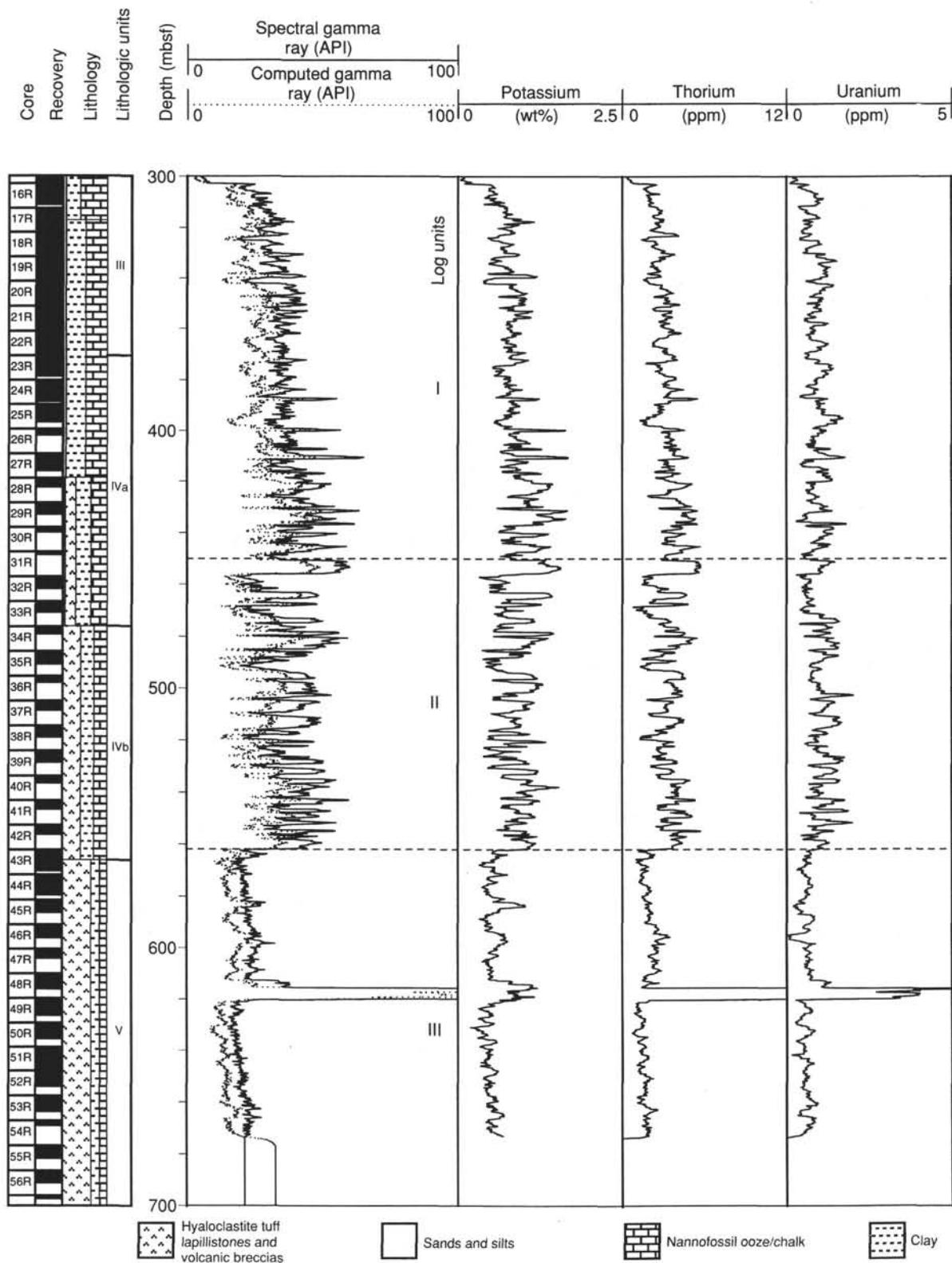


Figure 47. Data from the natural gamma-ray spectrometry tool (NGT) recorded on the quad combination tool string. The track on the left shows the total and the computed gamma-ray counts, and following tracks the K, U, and Th components of the total gamma-ray signal.

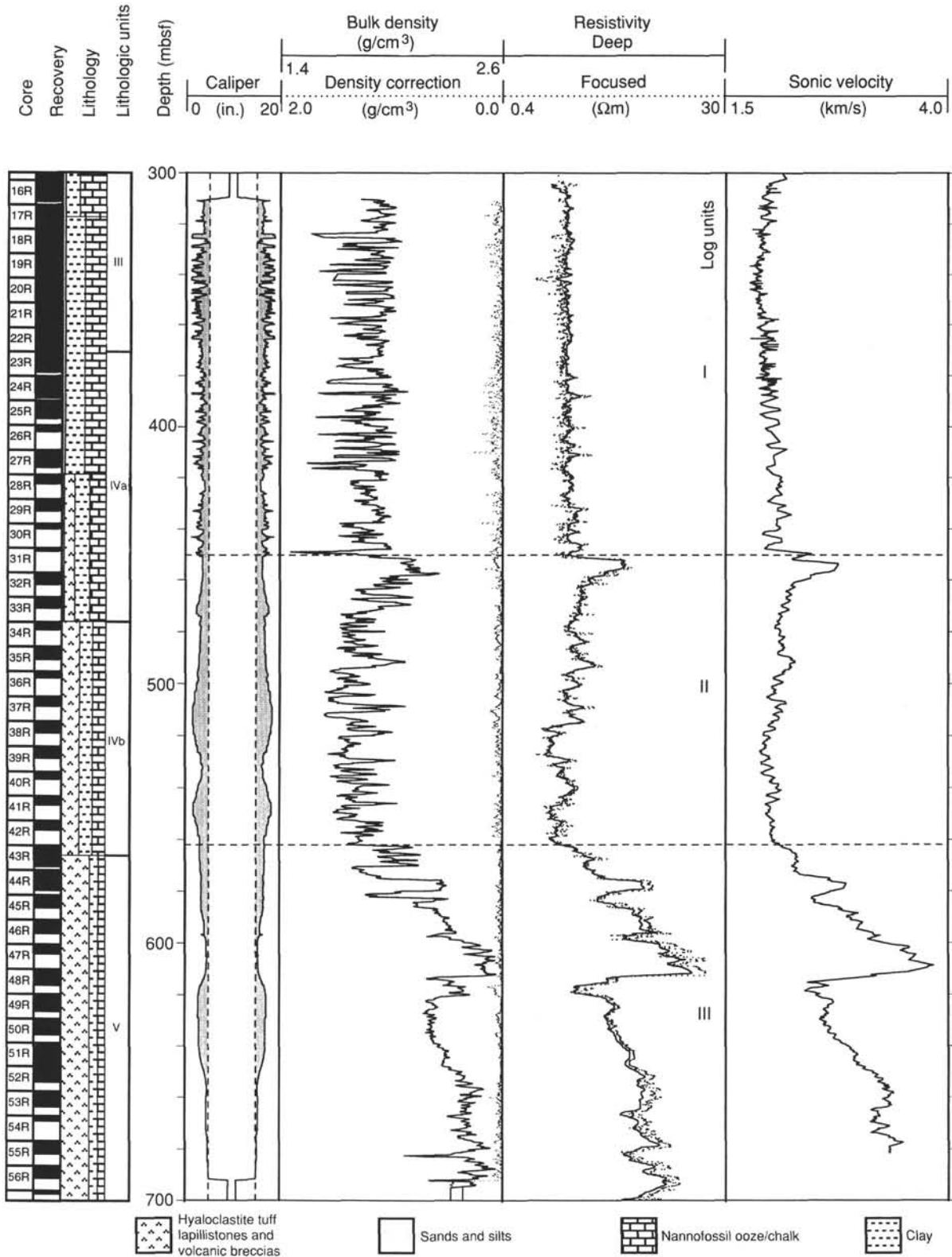


Figure 48. Hole 956B physical logs; caliper data from the high temperature lithodensity tool (HLDT) shown with: bulk density data from the HLDT; deep phasor induction and spherically focused resistivity from the phasor dual induction tool (DIT); sonic velocity data from the long-spaced sonic tool (LSS). The central white area in the caliper log represents the RCB bit size (9 7/8 in.) and the shading represents the "washed out" portion of the hole from the bit size to the actual measured diameter. The sonic velocity data have been processed to remove cycle skips.

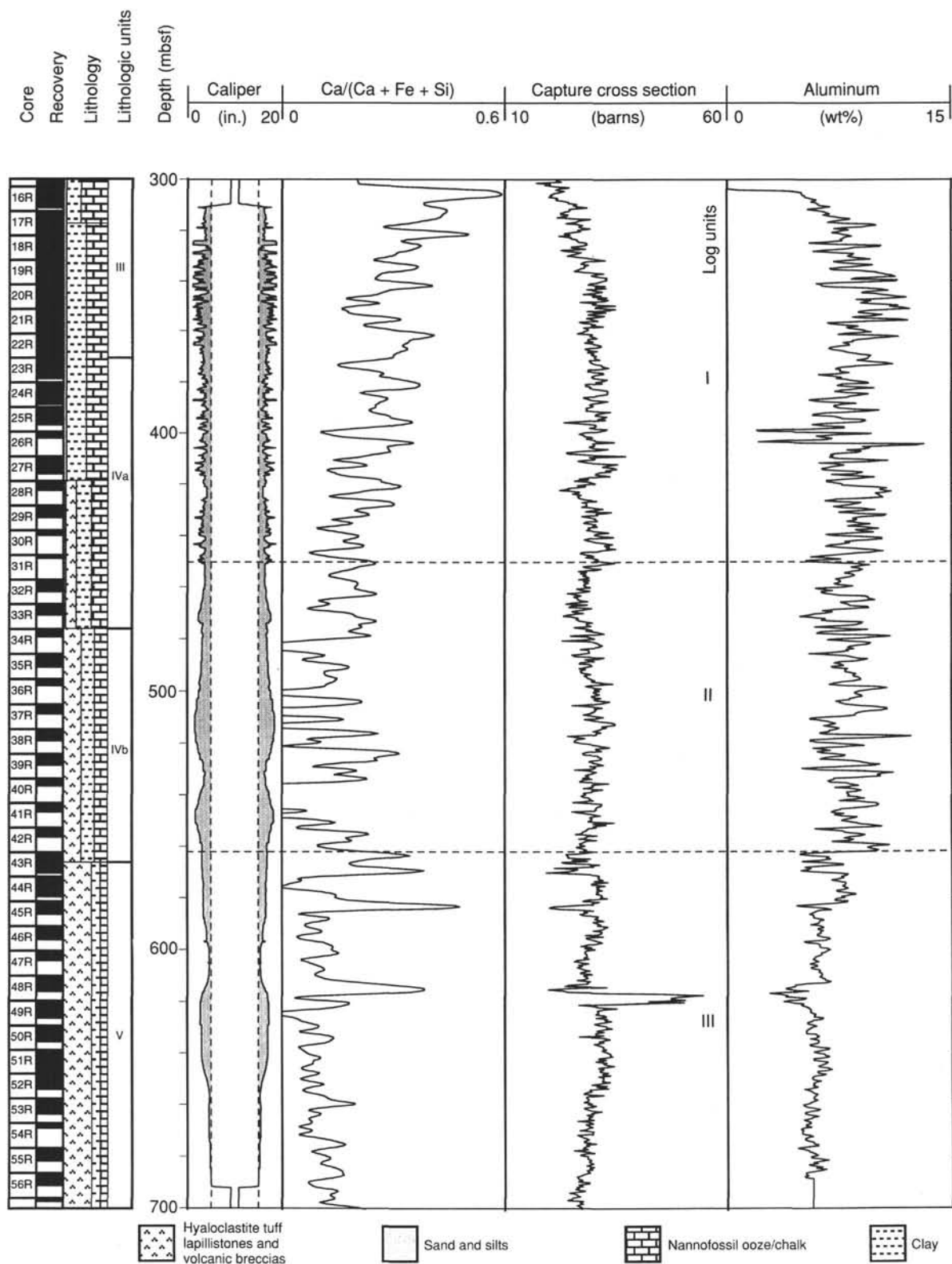


Figure 49. Caliper data from the high temperature lithodensity tool (HLDT) shown with: elemental yield ratio of $Ca/(Ca + Fe + Si)$, thermal neutron capture cross-section from the gamma-ray spectrometry tool (GST), and Al concentration from the aluminum activation clay tool (AACT).

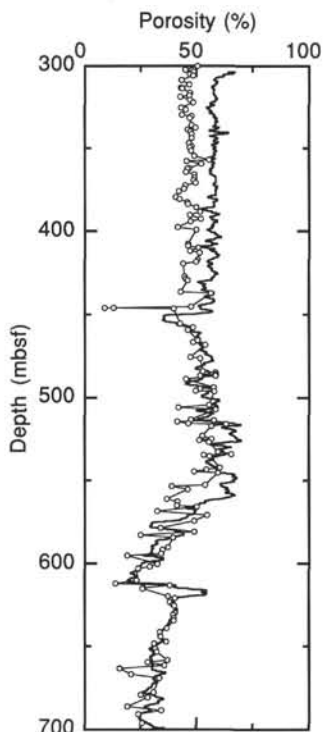


Figure 50. Porosity, calculated from the medium resistivity log using Archie's law (constants $a = 1.53$ and $m = 2.18$), compared to measurements of porosity on discrete core samples. Open circles = discrete core measurements.

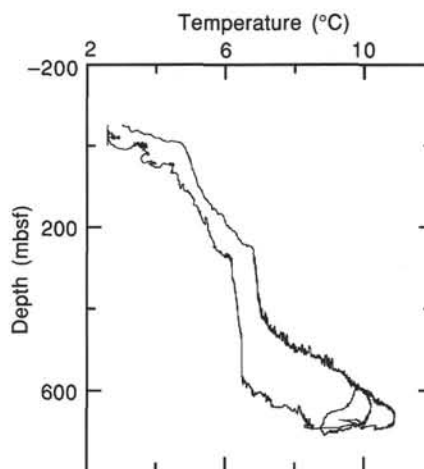


Figure 51. Temperature measurements from the Lamont-Doherty temperature logging tool taken from the quad combination run.

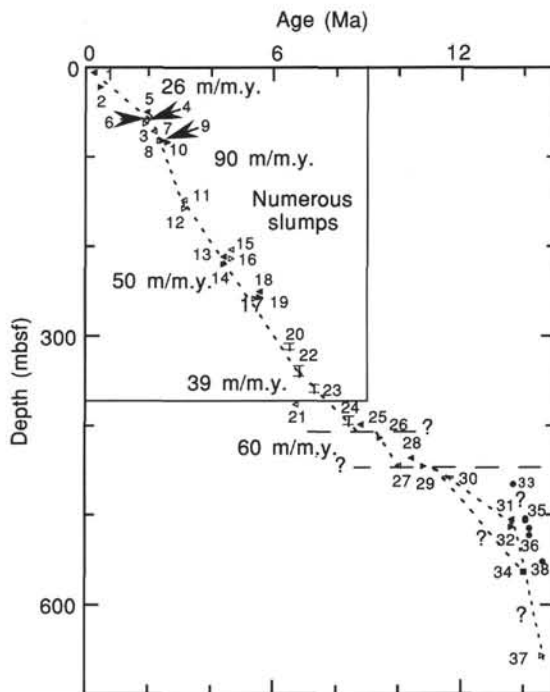


Figure 52. Sediment accumulation rates for Hole 956A. Vertical bars represent distances between sample points. Numbers refer to datum levels given in Table 13. Right-pointing filled triangle = nanofossil minimum age, left-pointing filled triangle = nanofossil maximum age, right-pointing open triangle = foraminifer minimum age, left-pointing open triangle = foraminifer maximum age, and filled square = base Mogan age.

Table 13. Datum levels used in calculation of sediment accumulation rate curves.

Event	Sample	Depth (mbsf)		Age (Ma)	Age (Ma)		
		Top	Bottom		Maximum	Minimum	
1	FO <i>E. huxleyi</i>	157-956A-1H-CC, 12	157-956A-	6.06	—	0.26	—
2	LO <i>P. lacunosa</i>	3H-5, 58	—	22.18	—	—	0.46
3	FO <i>Gr. truncatulinoides</i>	7H-5, 51–53	—	60.10	—	1.92	—
4	Absence <i>Gr. truncatulinoides</i>	7H-CC, 0–2	—	63.15	—	—	1.92
5	Absence <i>D. brouweri</i>	6H-CC	—	50.43	—	1.95	—
6	LO <i>D. brouweri</i>	7H-5, 52	—	60.12	—	—	1.95
7	FO <i>Gr. inflata</i>	8H-CC, 0–2	—	72.09	—	2.19	—
8	LO <i>Gr. miocenica</i>	9H-CC, 0–2	—	82.14	—	—	2.37
9	LO <i>D. pentaradiatus</i>	9H-CC	—	82.15	—	—	2.44
10	LO <i>D. surculus</i>	10H-2, 103	—	84.63	—	2.61	—
11	Absence <i>Ss. seminulina</i>	16H-CC, 0–2	—	148.75	—	3.15	—
12	LO <i>Ss. seminulina</i>	17H-CC, 0–2	—	157.59	—	—	3.15
13	Absence <i>Amaurolithus</i> spp.	157-956B-6R-5, 15	157-956B-	211.25	—	4.39	—
14	LO <i>Amaurolithus</i> spp.	7R-4, 50	—	219.70	—	—	4.39
15	Absence <i>Gg. nepenthes</i>	5R-CC, 0–2	—	203.76	—	4.63	—
16	LO <i>Gg. nepenthes</i>	6R-CC, 0–2	—	213.22	—	—	4.63
17	LO <i>Gr. juanai</i>	11R-CC, 0–2	—	258.42	—	—	5.40
18	Absence <i>D. quinqueramus</i>	10R-CC	—	250.98	—	5.56	—
19	LO <i>D. quinqueramus</i>	11R-3, 41	—	256.61	—	—	5.56
20	FO <i>A. amplificus</i>	16R-6, 11	17R-4, 47	308.91	315.77	6.50	—
21	FO <i>Gr. conomiozea?</i>	23R-6, 34–36	—	376.26	—	6.70	—
22	FO <i>R. pseudoubilicus</i> (>7 µm)	19R-3, 33	20R-4, 75	333.23	344.75	6.80	—
23	FO <i>A. primus</i>	21R-4, 61	22R-3, 70	354.31	362.60	7.30	—
24	FO <i>D. quinqueramus</i>	25R-2, 79	26R-2, 56.5	389.69	399.07	8.40	—
25	Absence <i>R. pseudoubilicus</i> (>7 µm)	26R-2, 56.5	—	399.07	—	8.80	—
26	LO <i>D. hamatus</i>	27R-CC, 8, 5	—	413.30	—	—	9.40
27	FO <i>Nq. acostaensis</i>	31R-1, 9–17	—	445.35	—	9.99	—
28	FO <i>D. hamatus</i>	30R-1, 77	—	436.47	—	10.40	—
29	LO <i>C. miopelagicus</i>	31R-1, 100	—	446.30	—	—	10.80
30	LO <i>C. floridanus</i>	32R-2, 106	32R-4, 14	457.49	459.57	11.60	—
31	Absence <i>S. heteromorphus</i>	37R-2, 55	—	505.35	—	13.60	—
32	LO <i>S. heteromorphus</i>	38R-1, 90	—	513.80	—	—	13.60
33	CSACn (t)	33R-2, 15	33R-2, 35	466.01	466.21	13.67	—
34	PI ignimbrite	43R-3	—	564.00	—	14.00	—
35	CSACn (o)	37R-1, 105	37R-3, 35	504.35	506.65	14.05	—
36	CSADn (t)	38R-2, 85	39R-1, 15	515.13	522.75	14.16	—
37	LO <i>Gr. peripheroronda</i>	53R-1, 52–53	—	657.82	—	—	14.60
38	CSADn (o)	42R-1, 45	42R-1, 55	551.95	552.05	14.61	—

Note: Numbers in left column refer to numbers on Figure 52.

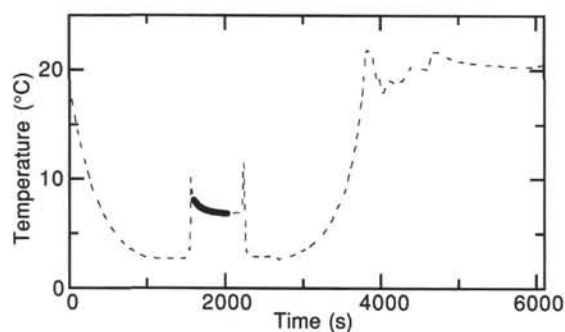


Figure 53. Measured temperatures (ADARA Tool 12) starting from the approximated zero time at the mud line and continuing through to the extraction of Core 157-956A-6H, 44.1 mbsf. The equilibrium temperature was extrapolated as 4.578°C. Dashed line shows measured temperature; solid line shows calculated temperature.

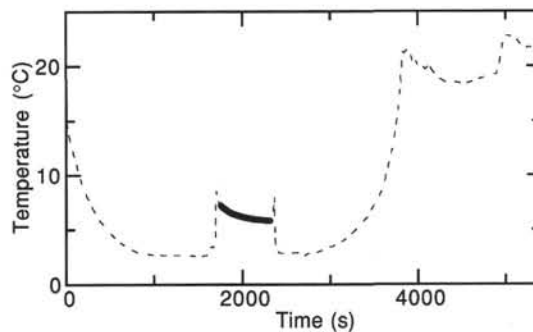


Figure 54. Measured temperatures (ADARA Tool 12) starting from the approximated zero time at the mud line and continuing through to the extraction of Core 157-956A-8H, 72.6 mbsf. The equilibrium temperature was extrapolated as 6.315°C but is considered unreliable because of frictional heating of the probe. Dashed line shows measured temperature; solid line shows calculated temperature.

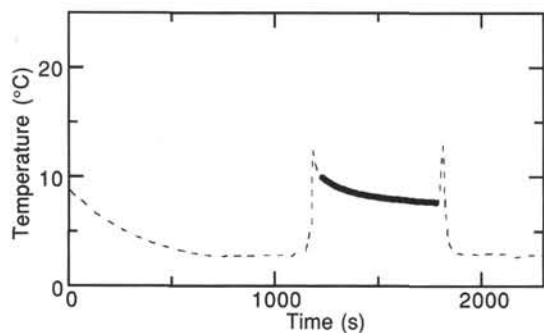


Figure 55. Measured temperatures (ADARA Tool 12) starting from the approximated zero time at the mud line and continuing through to the extraction of Core 157-956A-11H, 101.1 mbsf. The equilibrium temperature was extrapolated as 6.047°C. Dashed line shows measured temperature; solid line shows calculated temperature.

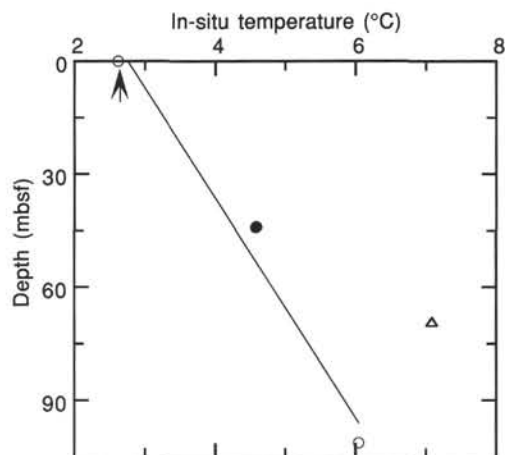


Figure 56. Hole 956A geothermal gradient from in-situ temperature measurements. The mud line (2.616°C, indicated by filled arrow) and equilibrium temperatures plotted vs. depth; the slope gives the geothermal gradient as 33.51°C/km ($y = 2.79314 + 0.03351x$). Filled circle = Core 157-956A-5H, 44.1 mbsf, 4.578°C; open circle = Core 157-956A-11H, 101.1 mbsf, 6.047°C. The temperature for Core 157-956A-8H, 72.6 mbsf, 6.315°C (indicated by triangle), was not used to calculate the gradient because of frictional heating of the probe.

Table 14. Pyrolysis data from Rock-Eval analysis of sediment samples from Sites 953, 955, and 956.

Core, section, interval (cm)	Depth (mbsf)	T_{max}	S_1	S_2	S_3	TOC (wt%)	PC	HI	OI	PI	S_2/S_3
			(mg C/g)								
157-953C-											
65R-4, 33-34	796.50	424	0.08	0.42	0.97	0.45	0.04	93	215	0.16	0.43
66R-2, 73-75	804.10	428	0.13	0.46	0.71	0.38	0.04	121	186	0.22	0.64
67R-5, 79-80	818.20	432	0.18	1.28	1.19	0.39	0.12	328	305	0.12	1.07
157-955A-											
1H-3, 50-51	3.50	410	0.50	1.01	2.49	0.65	0.12	155	383	0.33	0.40
1H-6, 23-24	7.73	397	0.25	0.16	2.57	0.51	0.03	31	503	0.62	0.06
2H-6, 42-43	16.02	409	0.23	0.39	1.79	0.70	0.05	55	255	0.37	0.21
4H-6, 65-66	35.25	416	0.17	0.31	1.80	0.65	0.04	47	276	0.35	0.17
5H-2, 60-61	38.70	425	1.56	6.22	3.35	2.59	0.64	240	129	0.20	1.85
6H-2, 88-89	48.48	416	0.97	3.74	3.17	1.91	0.39	195	165	0.21	1.17
6H-4, 38-39	50.98	422	1.37	4.61	2.59	1.31	0.49	351	197	0.23	1.77
8H-6, 136-137	73.96	420	0.53	1.63	2.14	1.40	0.18	116	152	0.25	0.76
9H-2, 139-140	77.49	419	0.19	0.43	2.03	0.67	0.05	64	302	0.31	0.21
11H-2, 92-93	96.02	428	0.22	0.71	1.63	0.62	0.07	114	262	0.24	0.43
14H-4, 100-101	127.60	429	0.27	0.63	1.41	0.93	0.07	67	151	0.30	0.44
17H-5, 40-41	157.00	405	0.09	0.23	1.70	0.47	0.02	48	361	0.28	0.13
18H-3, 120-121	164.30	399	0.09	0.15	1.62	0.37	0.02	40	437	0.37	0.09
44X-1, 28-29	407.10	406	0.05	0.12	1.19	0.33	0.01	36	360	0.31	0.10
56X-2, 55-56	524.50	368	0.06	0.16	1.44	0.33	0.01	48	436	0.27	0.11
157-956A-											
1H-1, 56-57	0.56	416	0.36	0.99	2.44	0.98	0.11	101	248	0.27	0.04
3H-2, 19-20	17.29	426	0.64	2.35	2.86	1.18	0.24	199	242	0.21	0.82
4H-7, 35-36	34.45	328	0.22	0.45	1.92	0.40	0.05	112	480	0.33	0.23
5H-6, 34-35	42.44	426	0.57	2.20	2.15	0.89	0.23	247	241	0.21	1.02
6H-1, 22-23	44.32	420	0.26	0.90	1.95	0.61	0.09	147	319	0.22	0.46
7H-5, 83-84	60.43	409	0.15	0.44	1.19	0.52	0.04	84	228	0.26	0.36
8H-2, 58-59	65.18	395	0.21	0.34	2.45	0.33	0.04	103	742	0.39	0.13
15H-5, 116-117	136.80	412	0.24	0.52	1.42	0.57	0.06	91	249	0.32	0.36

Notes: TOC = total organic carbon, PC = petroleum potential, HI = hydrogen index, OI = oxygen index, PI = production index.

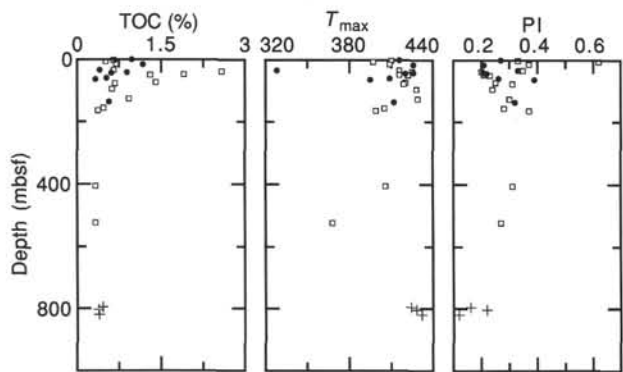


Figure 57. Variation of organic carbon, T_{max} , and production index (PI) as a function of depth. Filled circles = Site 956, open squares = Site 955, and plus signs (+) = Site 953.

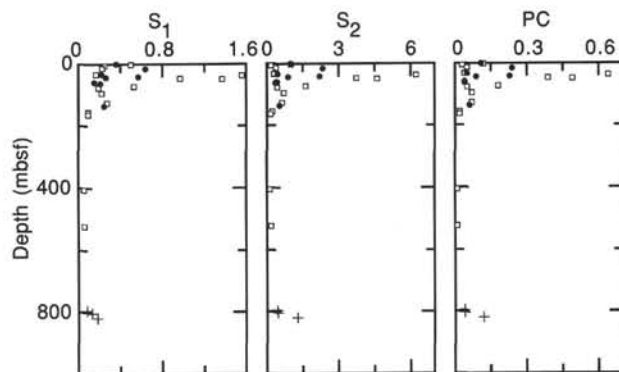


Figure 59. Variation of S_1 , S_2 , and production capacity (PC) with depth. Filled circles = Site 956, open squares = Site 955, and plus signs (+) = Site 953.

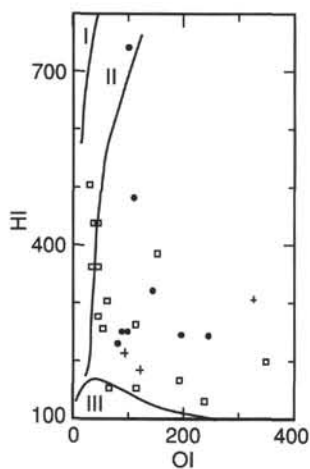


Figure 58. Hydrogen index (HI) as a function of oxygen index (OI) (modified van Krevelen diagram). Filled circles = Site 956, open squares = Site 955, and plus signs (+) = Site 953.

SHORE-BASED LOG PROCESSING

HOLE 956B

Bottom felt: 3453.4 mbrf (used for depth shift to seafloor)
Total penetration: 703.5 mbsf
Total core recovered: 297.4 m (54%)

Logging Runs

Logging string 1: DIT/LSS/HLDT/CNTG/NGT
 Logging string 2: ACT/GST/NGT
 Logging string 3: FMS/GPIT/NGT (two passes)

Wireline heave compensator was used to counter ship heave resulting from the mild sea conditions.

Bottom-hole Assembly

The following bottom-hole assembly depths are as they appear on the logs after differential depth shift (see "Depth shift" section) and depth shift to the seafloor. As such, there might be a discrepancy with the original depths given by the drillers on board. Possible reasons for depth discrepancies are ship heave, use of wireline heave compensator, and drill string and/or wireline stretch.

DIT/LSS/HLDT/CNTG/NGT: Bottom-hole assembly at 302.5 mbsf.

ACT/GST/NGT: Bottom-hole assembly at 302.5 mbsf.

FMS/GPIT/NGT: Bottom-hole assembly at 284 mbsf.

Processing

Depth shift: All original logs have been interactively depth shifted with reference to NGT from DIT/LSS/HLDT/CNTG/NGT run, and to the seafloor (-3453.4 m). A list of the amount of differential depth shifts applied at this hole is available upon request.

Gamma-ray processing: NGT data have been processed to correct for borehole size and type of drilling fluid.

Acoustic data processing: The sonic logs have been processed to eliminate some of the noise and cycle skipping experienced during the recording.

Geochemical processing: For detailed explanation of the processing please refer to the "Explanatory Notes" chapter, this volume, or to the geochem.doc file on the enclosed CD-ROM. The elemental yields recorded by the GST tool represent the relative contribution of only some of the rock-forming elements (iron, calcium, chlorine, silica, sulfur, hydrogen, gadolinium, and titanium—the last two computed during geochemical processing) to the total spectrum. Because

other rock-forming elements are present in the formation (such as aluminum, potassium, etc.), caution is recommended in using the yields to infer lithologic changes. Instead, ratios (see acronyms.doc on CD-ROM) are more appropriate to determine changes in the macroscopic properties of the formation. A list of oxide factors used in geochemical processing includes the following:

$\text{SiO}_2 = 2.139$

$\text{CaCO}_3 = 2.497$

$\text{FeO}^* = 1.358$

$\text{TiO}_2 = 1.668$

$\text{K}_2\text{O} = 1.205$

$\text{Al}_2\text{O}_3 = 1.889$

FeO^* = computed using an oxide factor that assumes a 50:50 combination of Fe_2O_3 and FeO factors.

Because of problems with the calibration of the tool, five repeat sections were recorded. Main pass and repeat section #5 were merged in the final plots.

Quality Control

During the processing, quality control of the data is mainly performed by cross-correlation of all logging data. Large (>12 in.) and/or irregular borehole affects most recordings, particularly those that require eccentricization (CNTG, HLDT) and a good contact with the borehole wall.

Hole diameter was recorded by the hydraulic caliper on the HLDT tool (CALI) and the caliper on the FMS string (C1 and C2).

Data recorded through bottom-hole assembly should be used qualitatively only because of the attenuation on the incoming signal. Invalid gamma ray spikes were recorded at 261–267 and 286.5–292.5 mbsf. The extremely high values of total gamma ray, uranium, and thorium recorded at 615–620 mbsf characterize a highly bioturbated sedimentary interval within the volcanoclastic breccia.

FACT = quality control curve in geochemical processing. Accuracy of the estimates is inversely proportional to the magnitude of the curve.

Note: Details of standard shore-based processing procedures are found in the "Explanatory Notes" chapter, this volume. For further information about the logs, please contact:

Cristina Broglia

Phone: 914-365-8343

Fax: 914-365-3182

E-mail: chris@ldeo.columbia.edu

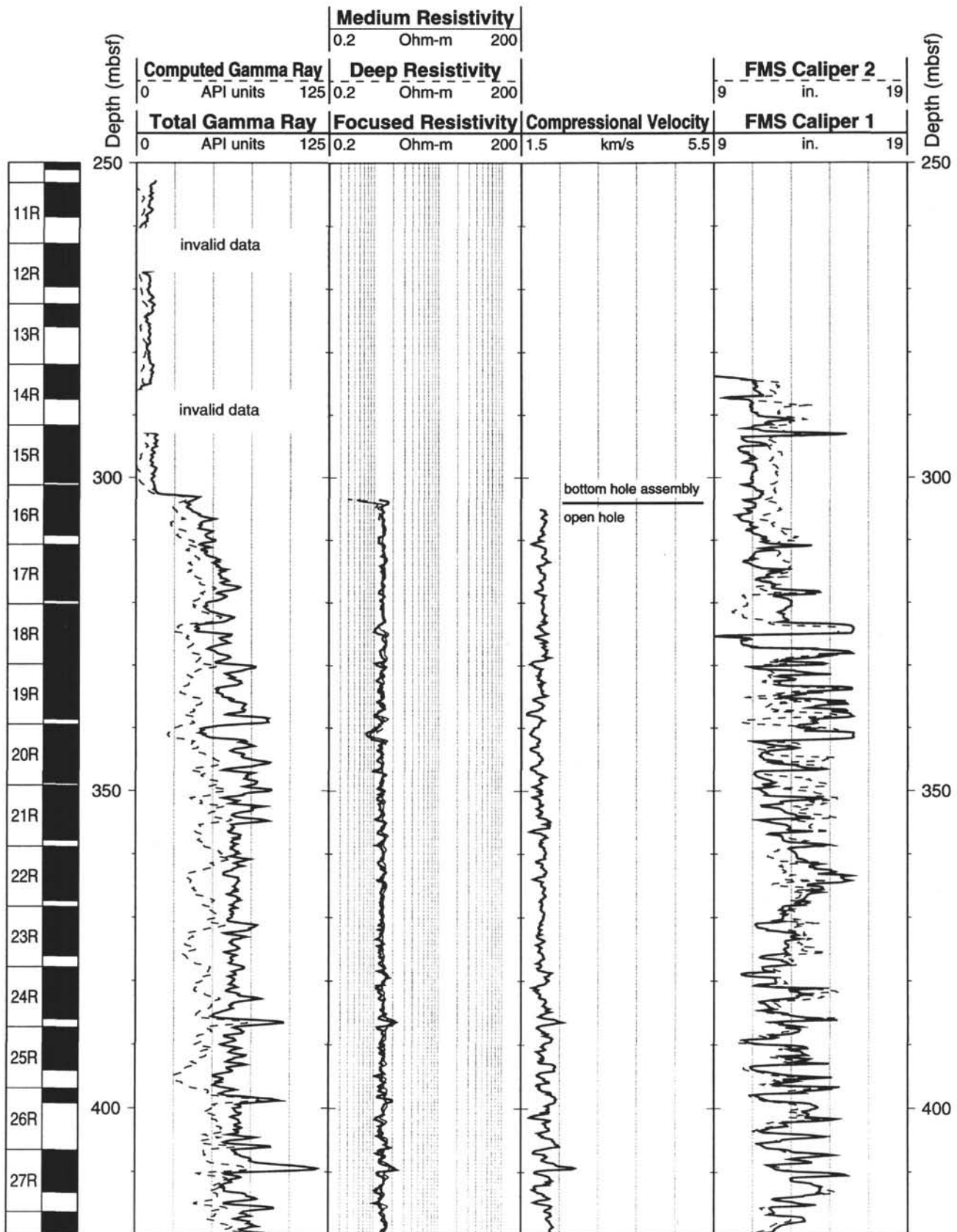
Elizabeth Pratson

Phone: 914-365-8313

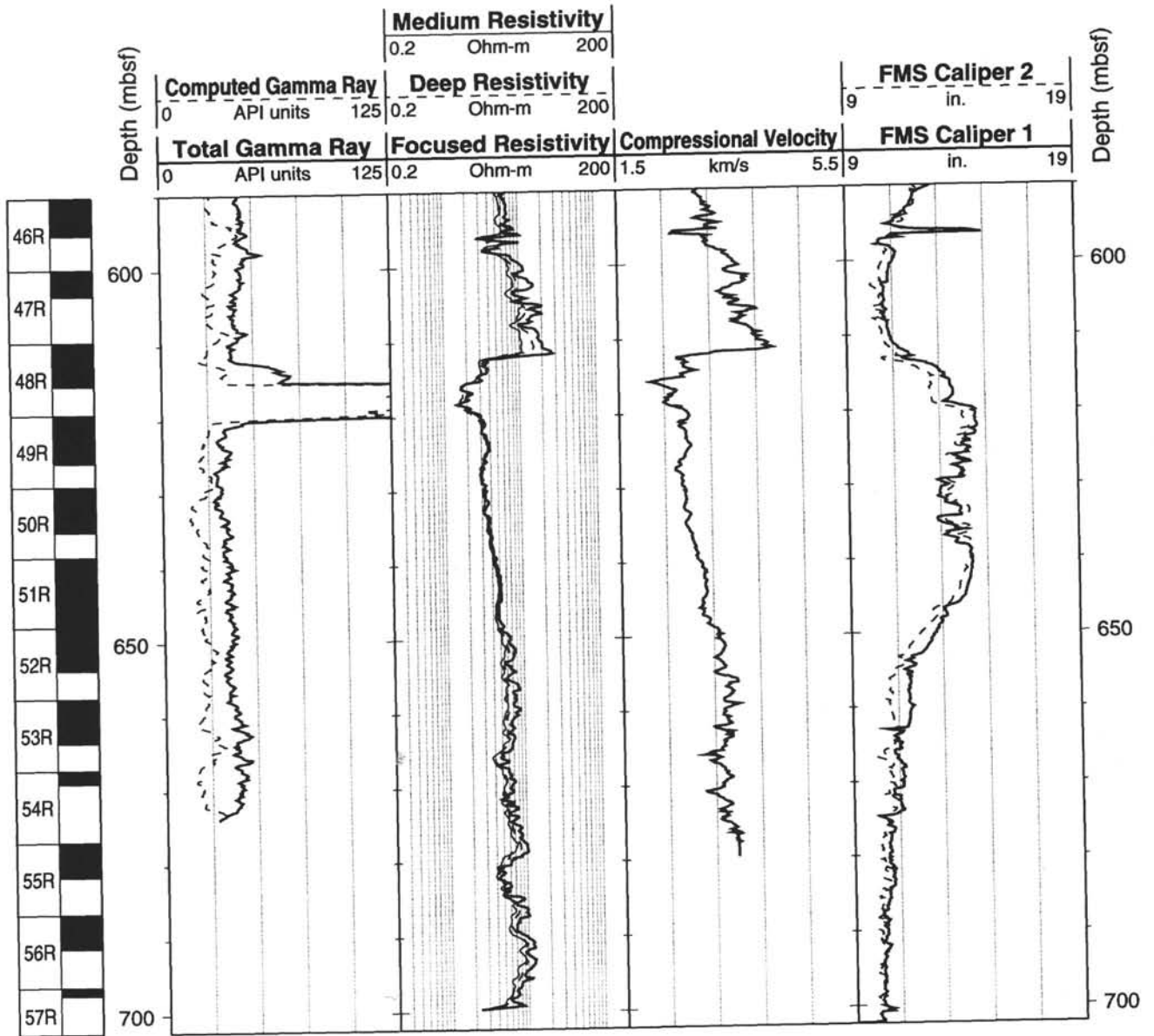
Fax: 914-365-3182

E-mail: beth@ldeo.columbia.edu

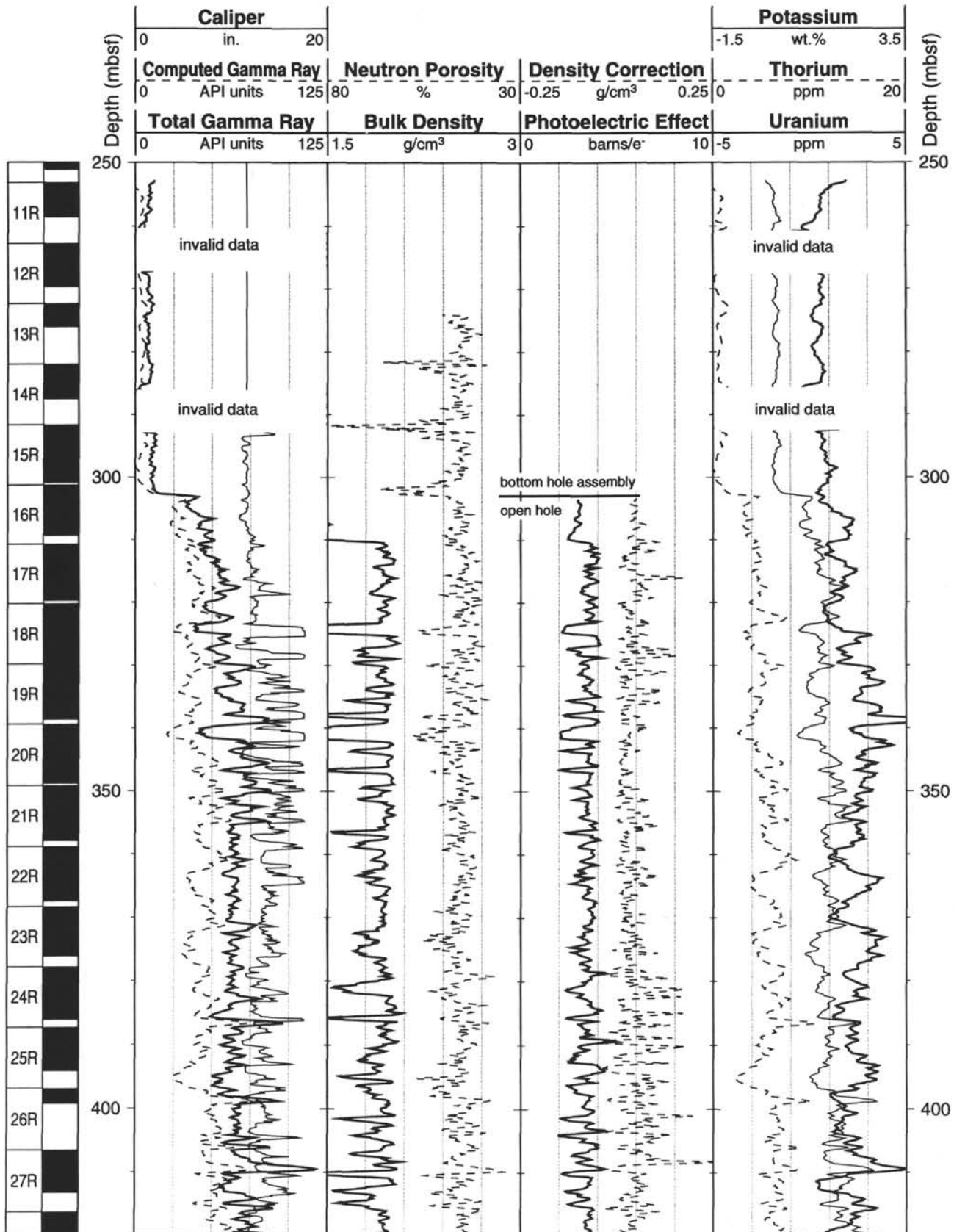
Hole 956B: Natural Gamma Ray-Resistivity-Sonic Logging Data



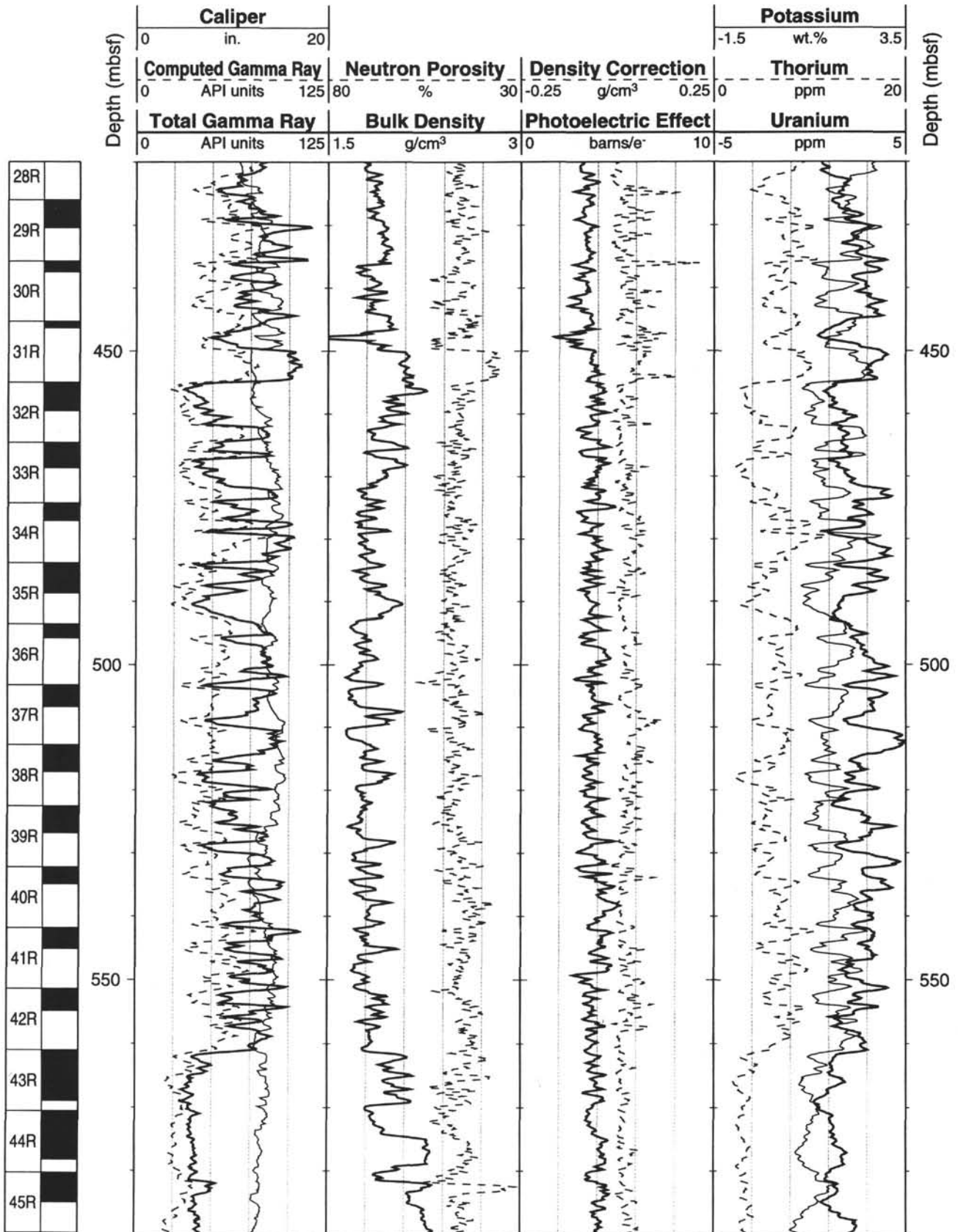
Hole 956B: Natural Gamma Ray-Resistivity-Sonic Logging Data (cont.)



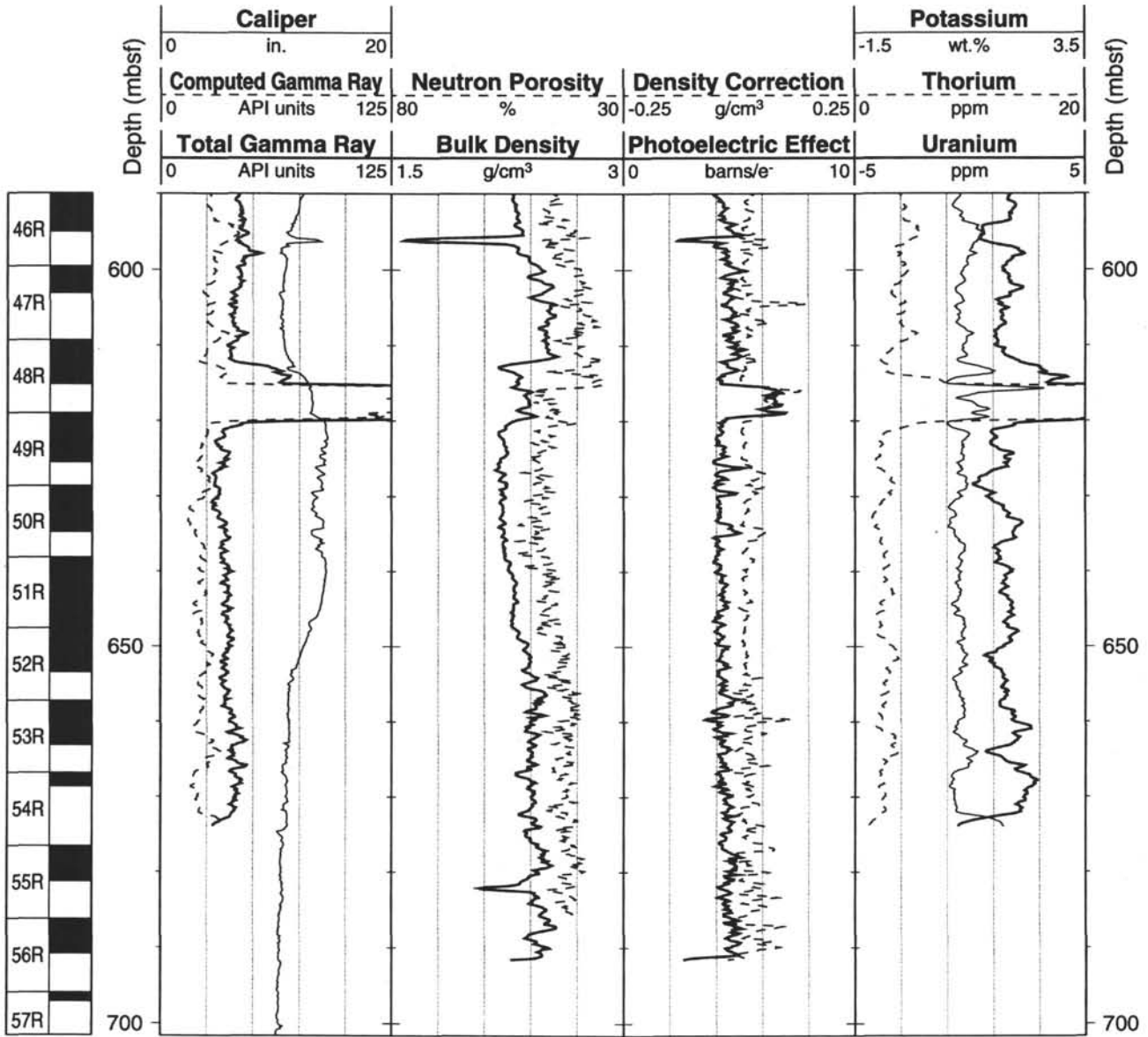
Hole 956B: Natural Gamma Ray-Density-Porosity Logging Data



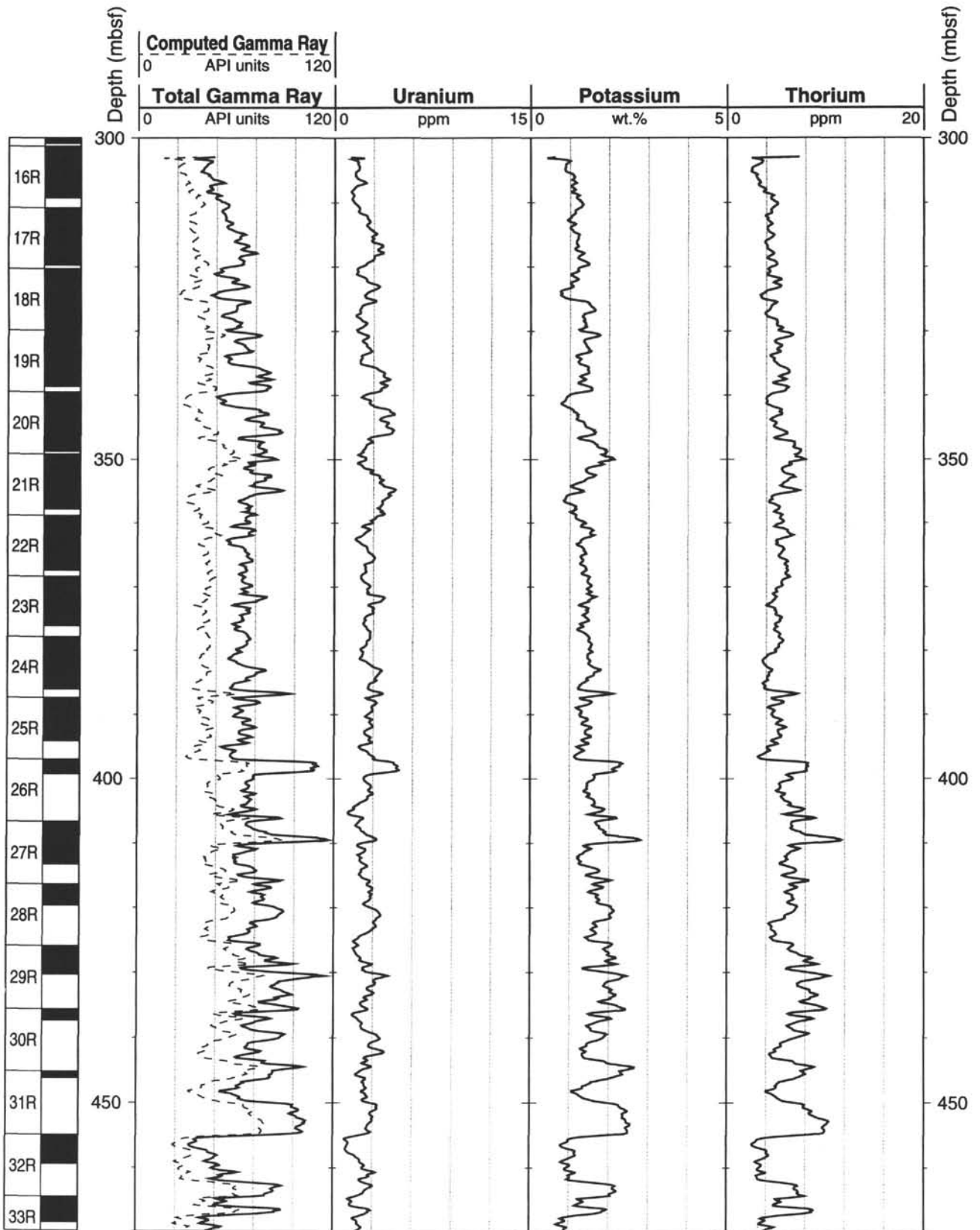
Hole 956B: Natural Gamma Ray-Density-Porosity Logging Data (cont.)



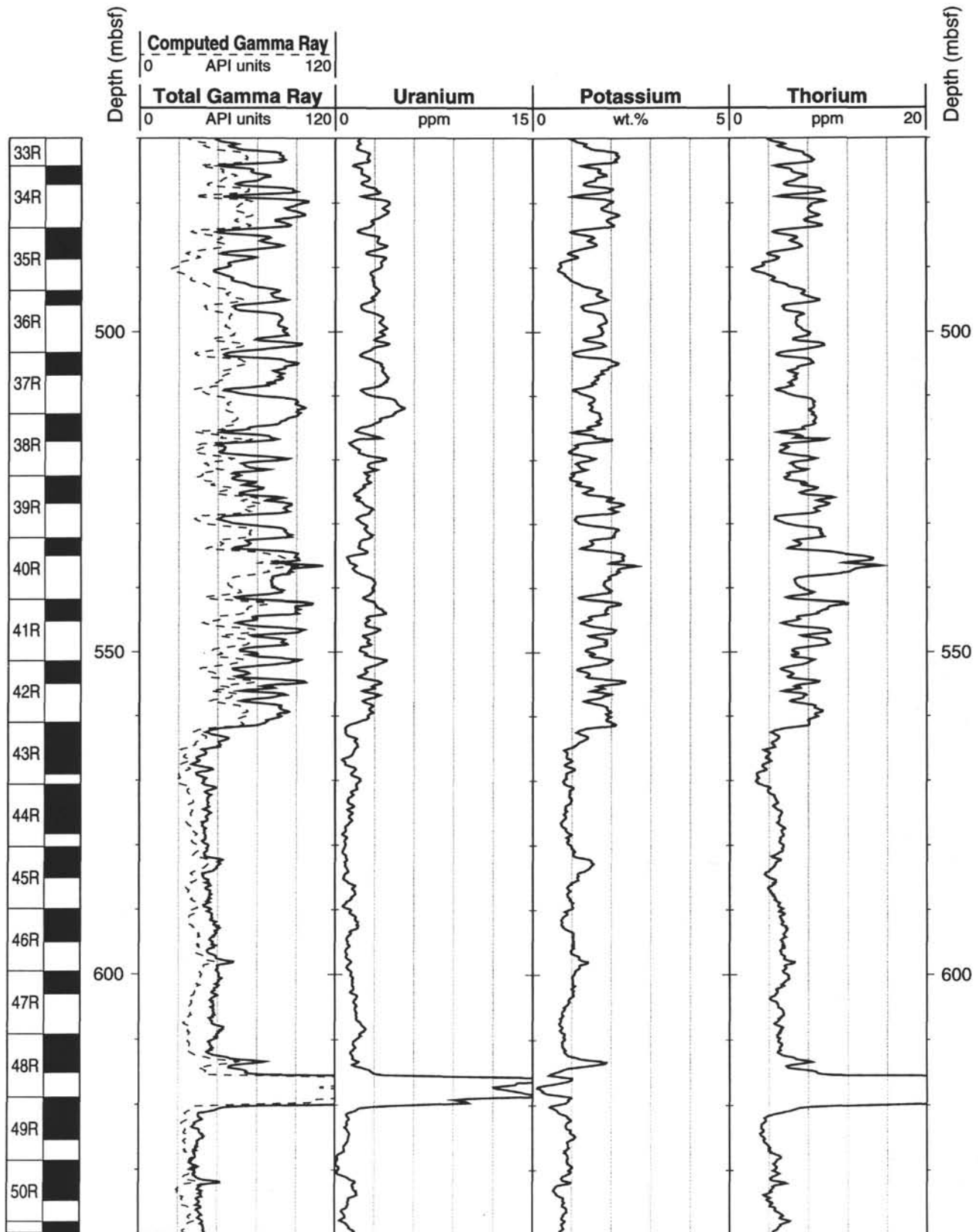
Hole 956B: Natural Gamma Ray-Density-Porosity Logging Data (cont.)



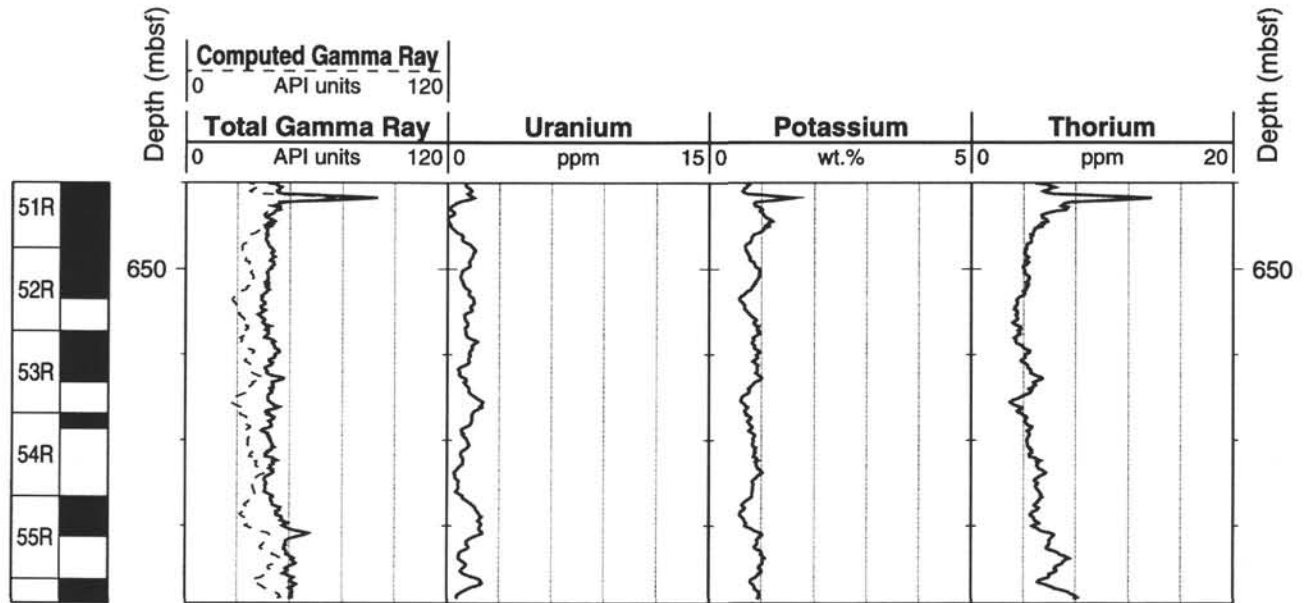
Hole 956B: Natural Gamma Ray Logging Data



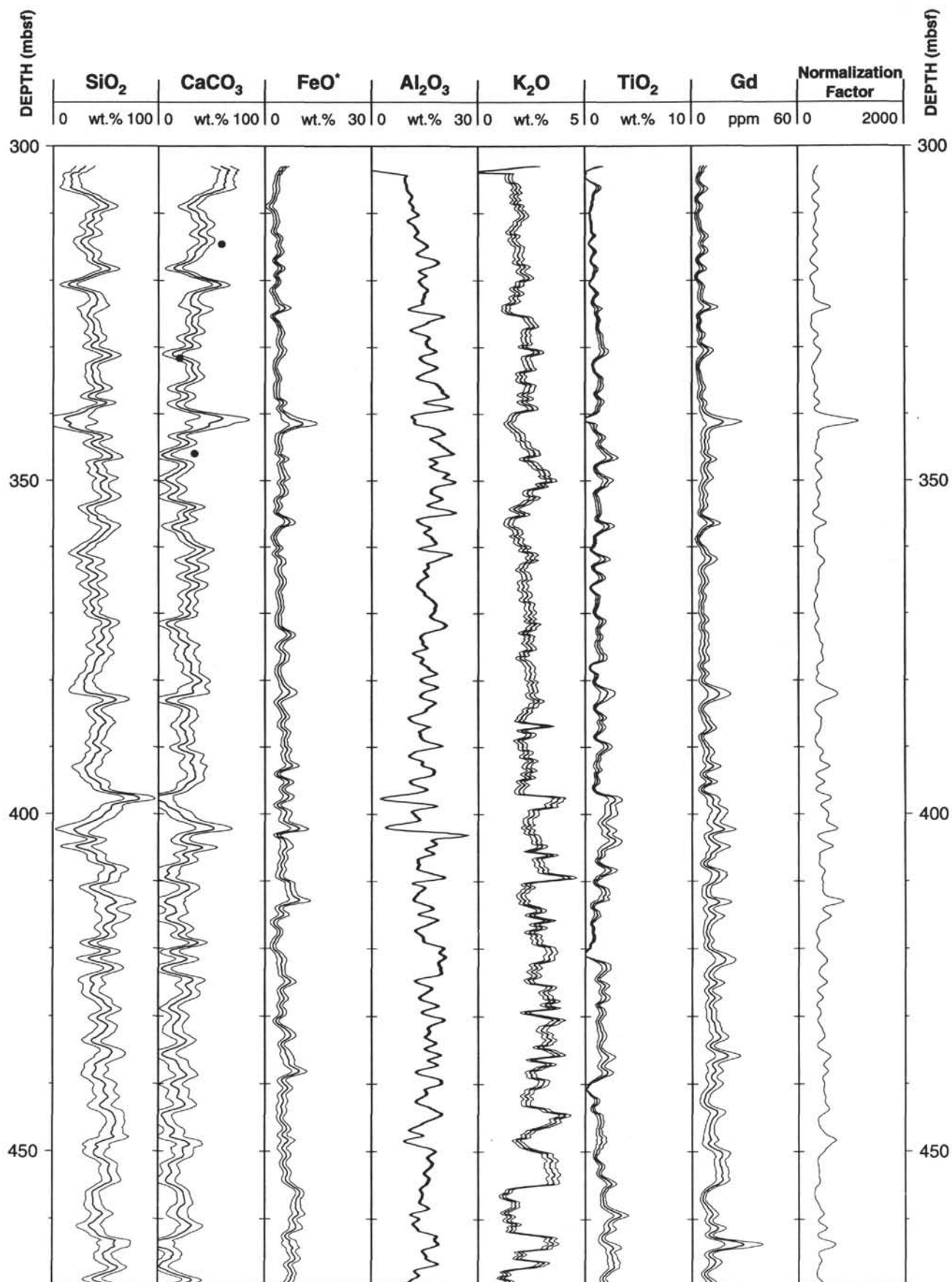
Hole 956B: Natural Gamma Ray Logging Data (cont.)



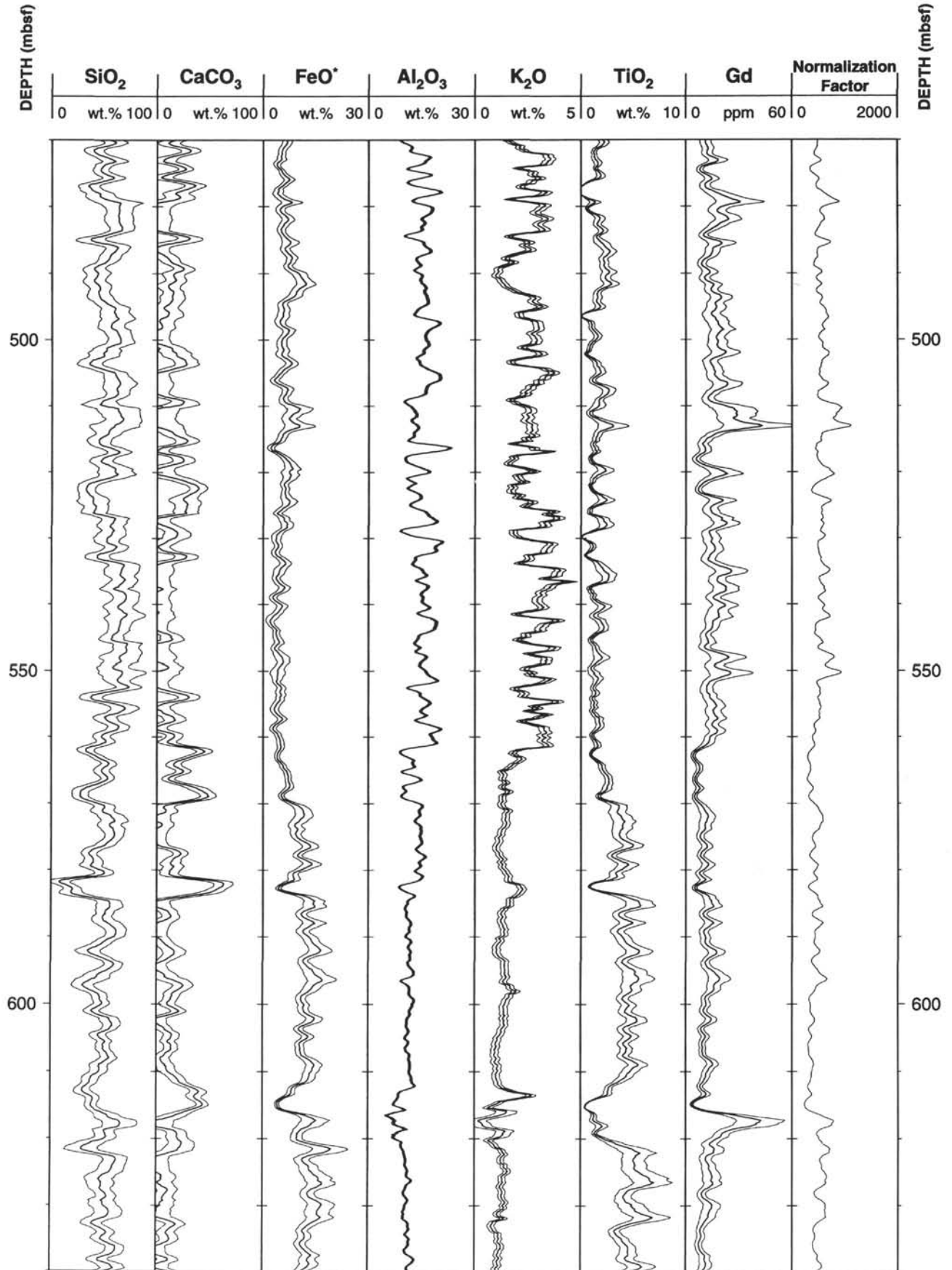
Hole 956B: Natural Gamma Ray Logging Data (cont.)



Hole 956B: Geochemical Logging Data



Hole 956B: Geochemical Logging Data (cont.)



Hole 956B: Geochemical Logging Data (cont.)

